AN EXPERIMENTAL STUDY OF THE STEADILY PLUNGING AIRFOIL IN UNIFORM-SHEAR FLOW

By

Mitchell Baxter Albrecht

A DISSERTATION

Submitted to
Michigan State University
in partial fulfillment of the requirements
for the degree of

Mechanical Engineering – Doctor of Philosophy

2022

ABSTRACT

AN EXPERIMENTAL STUDY OF THE STEADILY PLUNGING AIRFOIL IN UNIFORM-SHEAR FLOW

By

Mitchell Baxter Albrecht

Freestream shear may be found in many unsteady aerodynamic situations, such as the fighter jet landing through the air wake of an aircraft carrier and the micro air vehicle (MAV) navigating wind currents around buildings in urban environments. Despite the prevalence of shear in aeronautics, literature concerning its effects on unsteady airfoils is scarce. To address the need to understand the fundamental, complex aerodynamics of moving airfoils coupled with freestream shear, a novel experimental setup was implemented to investigate the case of the airfoil steadily plunging across a canonical uniform-shear approach flow in a water tunnel. The effect of unsteadiness on the NACA 0012 airfoil in shear is examined by using a servo motion system to plunge the airfoil from the high- to low-speed extremes of the shear zone and varying the steady plunge speed. The aerodynamic load (lift and drag coefficients), streamwise velocity component of the flow, separation and reattachment locations, and boundary layer thickness are characterized such that the flow measurements are correlated to the observed behavior of the load measurements.

First, uniform flow measurements are performed that confirm the unique experimental setup reproduces the expected Galilean transformation between the stationary and steadily plunging airfoils. It is confirmed that minimal blockage, confinement, or other artifacts result from the airfoil traversing over a large fraction of the test section's width. Molecular tagging velocimetry is uniquely implemented such that tag lines are created over the entire airfoil surface, image pairs are formed with the entire airfoil in view, and flow measurements are enabled for the moving airfoil. The airfoil aerodynamics are characterized in uniform flow at the same Reynolds numbers of the shear flow at three primary cross-stream locations of interest to provide baselines for the measurements in shear. For Reynolds numbers 13,500 and 16,500, a multi-region behavior is observed in the slope of the lift coefficient curve where the observed rapid rise in lift is related to the flow switching from

an open separation to a closed separation bubble. By contrast, a steady rise in lift is observed at Reynolds number 9,800 which correlates to only open separation being observed.

Next, the basic effect of shear on the stationary airfoil is studied by placing the airfoil at the three primary cross-stream locations in the shear flow, which also provides baseline measurements for the plunging airfoil in shear. It is observed that the current study reproduces the negative lift at zero angle of attack that is opposite of inviscid theory but consistent with recent computational and experimental literature from our group. A common observation in the lift and drag coefficient curves for the stationary airfoil in shear is asymmetry, as exemplified by the different stall behavior between positive and negative angles of attack. A multi-region behavior is observed among the lift curves which is connected to the airfoil switching from open separation to a closed separation bubble, like for uniform flow. Except for the Reynolds number 13,500 case, there is no observed difference in the angle of attack at which the flow switches from open separation to a closed separation bubble in shear compared to uniform flow. For the highest shear, lowest Reynolds number case, only open separation is observed at positive angles of attack, like the corresponding results in uniform flow.

Finally, the effect of the steadily plunging airfoil motion in shear is studied in comparison with its stationary airfoil counterpart. For the range of dimensionless shear rates (0.40-0.69) and chord Reynolds numbers (9,800-16,500) in this study, it is observed that the slope of the lift coefficient curve for the plunging airfoil begins to rapidly increase at lower effective angle of attack than for the stationary airfoil, which is found to be a result of the flow reattaching at a lower effective angle of attack for the former than for the latter. Near stall, the magnitude of the lift coefficient on the plunging airfoil is typically greater than that on the stationary airfoil, which is found to be related to the reattachment point occurring farther upstream for the former than for the latter. It is found that the airfoil must plunge as slowly as 1% of the freestream speed for the load on the plunging airfoil to be well-approximated by that on the stationary airfoil for the same effective angle of attack and freestream conditions.

This thesis is dedicated to Janine.

ACKNOWLEDGMENTS

Completing this dissertation and reaching this stage of my life would have been nearly impossible without all the people who have given me opportunities, support, and encouragement over the years. The following is my attempt to convey my gratitude for all those people.

First, I graciously thank my fiancée, Janine, for her unyielding love and support throughout the highs and lows of this endeavor. Thanks to my parents, Mike and Wendy, and my sister, Jamie, who have always motivated me to challenge myself and be a son/brother of whom they can be proud. Thanks to my friends who are too many to name from soccer, MSU, and elsewhere for providing me immeasurable social support.

Deepest thanks to my two exceptional co-advisors, Dr. Koochesfahani and Dr. Naguib, from whom I have been fortunate enough to learn. Their rigorous yet always supportive leadership has cultivated my competence and confidence in ways that will surely resonate throughout my life. The scientific mindset they instill in each TMUAL member cannot be replicated anywhere else and I am grateful for having been under their wings. Put simply but with tremendous weight: thank you both.

Special thanks to Dr. David Olson for his time, wisdom, patience, and much more which contributed to this success. I will be forever grateful for his mentorship and friendship that lead me to describe him in no other way than my academic "older brother" who I looked up to both as a scientist and human being. Thanks to the rest of my lab compatriots for their various technical and personal support: Borhan Hamedani, Kian Kalan, Basil Abdelmegied, Dr. Alireza Safaripour, Dr. Patrick Hammer, Dr. Mark Feero, and Dr. Shahram Pouya. Thanks to Dr. Doug Bohl for introducing me to fluid dynamics research and connecting me with my co-advisors, no doubt launching this saga.

Lastly, this work was sponsored by ONR grant number N00014-16-1-2760, the NDSEG Fellowship (ONR sponsored), and the MSU University Distinguished Fellowship.

TABLE OF CONTENTS

LIST OF TABLES

LIST OF FIGURES

CHAPTER 1

INTRODUCTION

1.1 Motivation

Moving aerodynamic bodies in real-world situations can experience non-uniform (shear) flows. For example, consider the fighter jet landing on an aircraft carrier. The wind over the carrier superstructure generates an unsteady air wake in the flight path of the landing aircraft. As the aircraft descends toward the flight deck through the air wake, it experiences a continuously changing approach flow. Another example is the micro air vehicle (MAV) flying around a city where wind around buildings creates non-uniform flows for the MAV to navigate. Similar examples can be found throughout aerodynamic applications and yet fundamental knowledge regarding aerodynamics of bodies in non-uniform flows is limited. This work aims to expand upon this currently limited knowledge by examining an airfoil steadily plunging (plunging with constant velocity) across a canonical uniform-shear (linearly varying velocity) approach flow, as illustrated in Fig. 1.1.

In Fig. 1.1, the approach flow is defined by $u_\infty(Y)$ with reference coordinates (X, Y), whereby

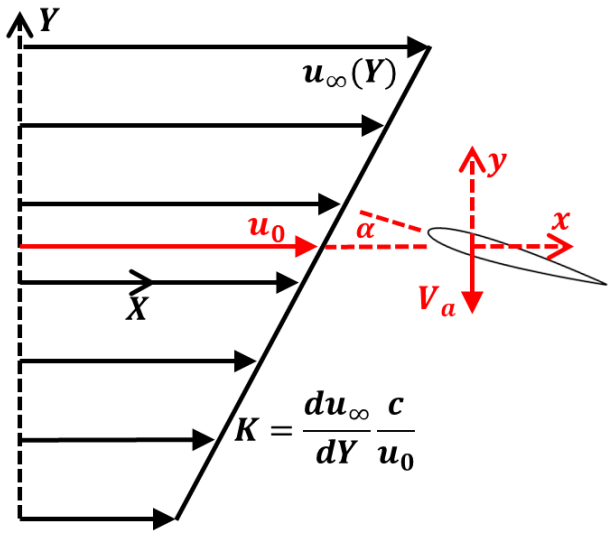

Figure 1.1: Schematic representation of an airfoil plunging in a uniform-shear freestream.

the shear rate du_∞/dY is a constant. The airfoil moves with steady velocity (V_a) and geometric angle of attack (α) in the negative-Y direction. The airfoil experiences a continuously changing local approach stream velocity (u_0) as it moves across the shear layer, where $u_0 \equiv u_\infty(Y)$ when the airfoil is at a particular cross-stream position Y used for reference. The local dimensionless shear rate is defined by K, based on u_0 and the airfoil chord (c) (see Fig. 1.1).

The local flow the moving airfoil experiences may be analyzed in a reference frame moving with the airfoil by a Galilean transformation (GT) from the laboratory reference frame. In the reference frame of the airfoil, the apparent direction and magnitude of the approach flow may be defined by the effective angle of attack (α_{eff}) and effective approach velocity (u_{eff}), respectively (see Fig. 1.2). The induced angle of attack (α_i) is the angle formed between V_a and u_0; the angular difference between the laboratory and airfoil reference frames. Note from Fig 1.2 that V_a is the apparent transverse flow direction in the reference frame of the airfoil and is positive, which means the ratio of the plunge velocity and local freestream velocity, given by $V_r = V_a/u_0$, is also positive. Consequently, α_i, α_{eff}, and u_{eff} are calculated by Eq. (1.1), (1.2), and (1.3), respectively.

$$\alpha_i = \tan^{-1}(V_r) \tag{1.1}$$

$$\alpha_{eff} = \alpha + \alpha_i \tag{1.2}$$

$$u_{eff} = u_0\sqrt{1 + \left(\frac{V_a}{u_0}\right)^2} = u_0\sqrt{1 + {V_r}^2} \tag{1.3}$$

The coordinates (x, y) referenced at the airfoil quarter-chord (the axis of rotation) and aligned with the flow direction such that the drag and lift (D and L, respectively) are aligned with the (x, y) axes and the laboratory reference frame. These axes are transformed to the airfoil's reference frame (x', y') drag and lift (D' and L', respectively) moving with the airfoil by Eq. (1.4).

$$\begin{bmatrix} D' \\ L' \end{bmatrix} = \begin{bmatrix} \cos(\alpha_i) & \sin(\alpha_i) \\ -\sin(\alpha_i) & \cos(\alpha_i) \end{bmatrix} \begin{bmatrix} D \\ L \end{bmatrix} \tag{1.4}$$

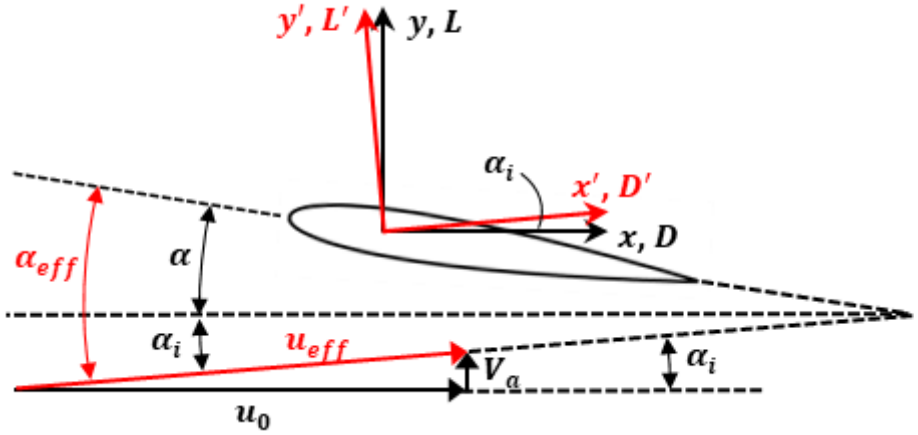

Figure 1.2: Geometric representation of the effective freestream flow on the plunging airfoil.

As discussed in Naguib & Koochesfahani (2020), a fundamental difficulty arises where α_{eff} cannot be uniquely defined since the freestream velocity varies across the approach stream due to the presence of shear. For this work, u_0 at the airfoil quarter-chord is arbitrarily chosen to calculate α_{eff}, leaving future work to address the issue of non-uniqueness. However, in the limit $K \rightarrow 0$, the flow is quasi-uniform (QU) and one would expect the chosen chordwise location to be irrelevant. From the perspective of the plunging airfoil, u_0 is a function of time; therefore, so are u_{eff} and α_{eff}, and the flow is unsteady even in the GT reference frame (Naguib & Koochesfahani, 2020).

It is well known for the airfoil steadily moving perpendicular to the freestream direction in uniform flow that a reference frame moving with the airfoil is used to predict the aerodynamic load. The prediction is done by equating the α_{eff} of the steadily moving airfoil with the geometric α of the stationary airfoil. However, with the unsteadiness of the airfoil across the shear zone as described above, a meaningful connection between the moving and stationary airfoils in shear flow is expected to be possible only under quasi-steady (QS) conditions. In the QS limit, the airfoil motion across the shear is sufficiently slow for the flow dynamics to adapt to the changing position of the airfoil within the shear zone. The unsteadiness of the problem may be characterized by the non-dimensional rate of change of u_0, denoted by $\dot{u}^+$ (Naguib & Koochesfahani, 2020).

$$\dot{u}^+ = \left(\frac{du_0}{dt}\right)\left(\frac{c}{u_0^2}\right) = \left(\frac{du_\infty}{dY}V_a\right)\left(\frac{c}{u_0^2}\right) = \left(\frac{du_\infty}{dY}\frac{c}{u_0}\right)\left(\frac{V_a}{u_0}\right) = KV_r \tag{1.5}$$

Since u_0 and c are the velocity and length scales, respectively, of the airfoil, they are also chosen here to nondimensionalize $\dot{u}^+$. From Eq. (1.5), one can see in the limit $KV_r \rightarrow 0$ that $\dot{u}^+ \rightarrow 0$ and the flow can be QS and/or QU (QUS) (Naguib & Koochesfahani, 2020).

1.2 Background

The flow field and aerodynamic load of a steady airfoil in an inviscid uniform-shear freestream were first provided by Tsien (1943). Tsien found that positive uniform-shear shifts the lift coefficient (C_L) versus α curve towards negative α, making the lift positive at zero α. Subsequent works extended this inviscid theory to generalized non-uniform velocity approach streams (James, 1951; Honda, 1960; Nishiyama & Hirano, 1970). In general, these works use potential flow analysis to consider the superposed inviscid solutions for the circular cylinder, shear approach flow and appropriate boundary conditions, which are then transformed using conformal mapping to obtain the airfoil result. Regardless, these works only consider the inviscid flow of the steady airfoil in shear, unlike the viscous flow of the unsteady airfoil in shear in the current work.

To the author's knowledge, there is no current theory for the load or flow field of a steadily plunging airfoil in shear flow. As discussed in the previous section, the plunging airfoil in shear is an unsteady problem. Existing unsteady aerodynamic theories, such as the classical work of Theodorsen (1935), typically describe the inviscid, oscillating airfoil with small disturbances. In general, none of the existing theories correspond to the steadily plunging airfoil in shear flow. The closest classical unsteady aerodynamic model related to the current work may be that of Wagner (1925), in which the "indicial" lift on the thin airfoil is described in terms of a step change in the angle of attack in an incompressible flow. Since the steadily plunging airfoil in shear undergoes a change in u_{eff} and α_{eff} across the shear layer, there may be particular flow conditions where the Wagner solution, though inviscid, provides insight.

Naguib & Koochesfahani (2020) performed an inviscid flow analysis on a plunging circular cylinder in an unbounded uniform-shear stream, which provided the most recent step toward a similar theory for the airfoil. In the work of Naguib & Koochesfahani (2020), the unsteadiness

parameter $\dot{u}^+$ from Eq. (1.5) was derived theoretically, but explicitly based on u_{eff}. For small V_r, the unsteadiness may be approximated by $K_{eff}V_r$ and is identical to KV_r of the plunging airfoil in the current work. For $K_{eff}V_r < 0.025$, the flow around the cylinder may be reasonably approximated as QUS. This QUS condition allows for a definition of the freestream incidence angle on the cylinder, as for the airfoil. Another interesting finding from the study is that the inviscid force was the same for the stationary and moving airfoil irrespective of the values of K and V_r; however, the same force was produced by different pressure distribution. In a viscous flow, this would be expected to change the boundary layer characteristics, including separation location.

Existing literature of steady airfoils in viscous, non-uniform approach flows is scarce. One study by Payne & Nelson (1985) performed wind tunnel experiments on the steady airfoil in shear at chord Reynolds number $Re_c \approx 10^5$. They observed asymmetry in the lift and drag curves for the airfoil in shear compared to in uniform flow but were unable to dissociate the effects of shear from the other effects present, such as turbulence from their shear-generating screen or the order of the measurement error. No other relevant works were available until recently when Hammer et al. (2018) found that the mean C_L is negative at zero α for the stationary NACA 0012 airfoil in viscous, positive uniform-shear flow at $Re_c \approx 1.2 \times 10^4$. The magnitude of the negative mean C_L also increased with increasing shear rate. These viscous results are directly opposite those predicted by the inviscid theory of Tsien (1943), which predicts a positive C_L at zero α.

Studies of unsteady airfoils in shear are similarly scarce and those that exist typically consider the pitching airfoil. Yu et al. (2018) and Hammer et al. (2019) showed asymmetry in the shed wake of the harmonically pitching NACA 0012 airfoil in positive uniform-shear, as opposed to a symmetric wake for uniform flow. At higher reduced frequencies ($k \equiv \pi f c/u_0$, where f is the oscillation frequency) the mean C_L on the pitching airfoil monotonically increased as the reduced frequency and shear rate increased. Hammer et al. (2019) more specifically demonstrated both computationally and experimentally that the mean C_L on the pitching airfoil in positive shear must pass a certain k threshold for the mean C_L to switch from negative to positive.

The unsteadiness of the shear layer may also be considered in addition to unsteady airfoil

motion. Safaripour-Tabalvandani (2020) investigated the effects of an unsteady shear layer on the aerodynamics of a stationary and a pitching airfoil. On the stationary airfoil in the unsteady shear layer, a positive lift at zero α was observed, and the slope of the C_L-α curve was nearly linear. The contrasting result of the positive lift at zero α for unsteady shear layer compared to negative lift for the steady shear layer was specifically attributed to the turbulent fluctuation in the flow. Interestingly, no reverse flow was observed in the mean streamwise velocity profiles of the boundary layer over the airfoil, contrary to the steady shear layer case. At low k, the sign of the pitching airfoil C_L in unsteady shear is positive, compared to negative in steady shear, while no difference in C_L is seen at higher reduced frequencies. The important distinction is drawn here that the aerodynamics of the airfoil in steady shear is different from that in unsteady shear, noting that the current work utilizes a steady shear layer.

The steadily plunging airfoil in a shear approach flow is a unique, unexplored problem, and thus little previous work exists on the topic. The works of Hamedani et al. (2017) and Hamedani et al. (2019) provide the most relevant and useful comparison to the current work, in which they investigated the effect of Re_c on a plunging airfoil in shear flow at $Re_c = 7.5\times10^4$ in a wind tunnel. When analyzed in the reference frame of the airfoil, they found the C_L on the moving airfoil is higher than that of the stationary airfoil at positive α_{eff}, with the largest difference occurring near stall. It was also observed that C_L was positive at zero α. However, the experiments had several limitations, including a shear layer width that was small relative to the airfoil chord, a shear region that was not uniform, and a shear layer that exhibited fluctuations similar to that of traditional shear layers.

From the above, one can appreciate the complex aerodynamics involved with an unsteady airfoil in a non-uniform flow. The current work is a continuing component of the above research at the Turbulent Mixing and Unsteady Aerodynamics Laboratory (TMUAL) at Michigan State University (MSU), aimed at uncovering the unique flow physics of an airfoil plunging across a uniform-shear approach flow. Consequently, the central purpose of the current research is to determine the conditions, if any exist, under which the aerodynamic load on the steadily plunging airfoil

in shear in the reference frame of the airfoil are the same as those on the stationary airfoil after considering α_{eff} and u_{eff}. Knowing whether a connection between the stationary and moving airfoil aerodynamics in shear flow can be made, and the conditions under which such a connection works, has a useful, practical ramification. Particularly, if such a connection is found, it alleviates the need to conduct experiments and/or computations on a moving model to study the aerodynamics of airfoils steadily traversing across shear flow.

1.3 Scope of the Current Study

The objective of this experimental study is to investigate the effects of freestream shear on the aerodynamic load and streamwise flow characteristics of the steadily plunging airfoil. To investigate this, the airfoil performs the steady plunge maneuver in the presence of a canonical uniform-shear flow in a water tunnel. The primary way of controlling the extent of the unsteadiness is by varying V_r through changing V_a. Plunge speeds up to V_a = 1 cm/s (10% of the nominal u_∞ = 10 cm/s shear flow centerline velocity) are used, where V_r varies throughout the plunge in the range of the shear profile (since u_0 is a function of time during the plunge). The experimental uniform-shear profile remains fixed which means the local Re_c and K of the airfoil only change with position along the shear profile. Since V_r varies, so does the KV_r parameter, allowing for the problem to be investigated in the context of the varied levels of unsteadiness.

This investigation is carried out by directly measuring the load on the airfoil via a load cell, and by measuring the streamwise component of the flow velocity over the airfoil suction surface via molecular tagging velocimetry (MTV). In both cases, the plunging airfoil results are compared to those of the stationary airfoil by relating their α_{eff} through Galilean transformation. It is examined whether the load on the stationary airfoil can be used to approximate those on the moving airfoil in the airfoil reference frame. The load is measured throughout the plunge over a range of α and V_a, while the flow measurements are measured at the centerline during the plunge for multiple α. The purpose of performing the experiments in a water tunnel is to take advantage of MTV flow diagnostic capabilities, which enables connections between the flow measurements around the

airfoil and the load measurements under the same conditions. For this study, single-component molecular tagging velocimetry (1c-MTV) is used to measure only the streamwise velocity of the flow. Unique flow physics associated with the plunging airfoil in shear, such as boundary layer profiles, and separation and reattachment behavior are evaluated. The low Reynolds number range evaluated in this study also aims to fill the knowledge gap for Reynolds numbers relevant to MAV flight.

1.4 Outline

The remainder of this document is presented in four chapters. Chapter 2 introduces the flow facility and the electromechanical system used to move the airfoil. The force transducer and techniques used to measure the load on the airfoil are discussed. The camera system and the procedures used for 1c-MTV over the airfoil surface are also outlined.

The primary results and discussion are divided into two chapters. Chapter 3 focuses on the load and flow measurement results in uniform flow which validate key aspects of the experimental setup and provide important baselines. The lift and drag coefficients, as well as the streamwise velocity component of the flow, are measured for the stationary airfoil at multiple cross-stream positions in uniform flow. The load and flow measurements are also performed in the reference frame of the moving airfoil and compared against those on the stationary airfoil at multiple cross-stream locations in the flow. Chapter 4 focuses on the load and flow measurement results in shear flow. The lift and drag coefficients, as well as the streamwise velocity component of the flow, are first measured for the stationary airfoil and compared against uniform flow results to establish the baseline effect of shear. Load and flow measurement results are then presented for the plunging airfoil and related to the stationary airfoil results in the airfoil reference frame under the same flow conditions. In both Chapters 3 and 4, the flow measurements are discussed in conjunction with the load measurements, noting boundary layer features that give context to the effects observed in the load measurements. Finally, Chapter 5 summarizes the important results of the present study.

CHAPTER 2

EXPERIMENTAL METHODS

2.1 Flow Facility

Experiments are conducted in a 10,000 L, 61 × 61 × 244 cm test section, close-loop water tunnel (Engineering Laboratory Design, ELD) located in TMUAL at MSU. Figure 2.1 provides a 3D model of the tunnel. The initial diffuser contains two perforated plates followed by a honeycomb with 1/4-inch diameter cells and fine mesh screen at the entrance of the settling chamber. The area contraction from the settling chamber to the test section entrance is 6:1. For uniform flow, a honeycomb with 1/8-inch diameter cells and fine-mesh screen are located at the entrance of the test section. The impeller of the water tunnel is powered by a Toshiba 20 hp motor and controlled with a Toshiba VF-AS1 drive which ensures day-to-day repeatability of the same freestream velocity. The water temperature is recorded throughout all measurements using a T-type thermocouple with a National Instruments USB-TC01 temperature input device, which accounts for the day-to-day variation of the laboratory temperature. Accurately setting the freestream velocity based on the recorded temperature, and thus the water viscosity, allows for precise control of the desired Reynolds number, which is important due to the Reynolds number sensitivity of the flow over the Reynolds number range of this study.

In this facility, velocity fluctuations in the freestream are due to both low frequency sloshing ($\lesssim$0.2 Hz) and the random turbulent fluctuations (Gendrich, 1999; Olson, 2011). Based on previous work (Gendrich, 1999; Olson, 2011; Olson et al., 2018), the total u_{rms} in the test section is typically less than 1.8% ($u_{rms} \lesssim 0.18$ cm/s at $u_\infty = 10$ cm/s), but after accounting for the sloshing, the u_{rms} attributed only to freestream turbulence intensity (FSTI $\equiv u_{rms}/u_\infty$) is expected to be 0.5-0.8% for the Re_c range in this study.

This study uses a NACA 0012 airfoil of chord $c = 12$ cm and span $b = 61$ cm ($AR = b/c = 5.1$) made up of a 2 mm-thick fiberglass-resin composite shell that was designed and constructed

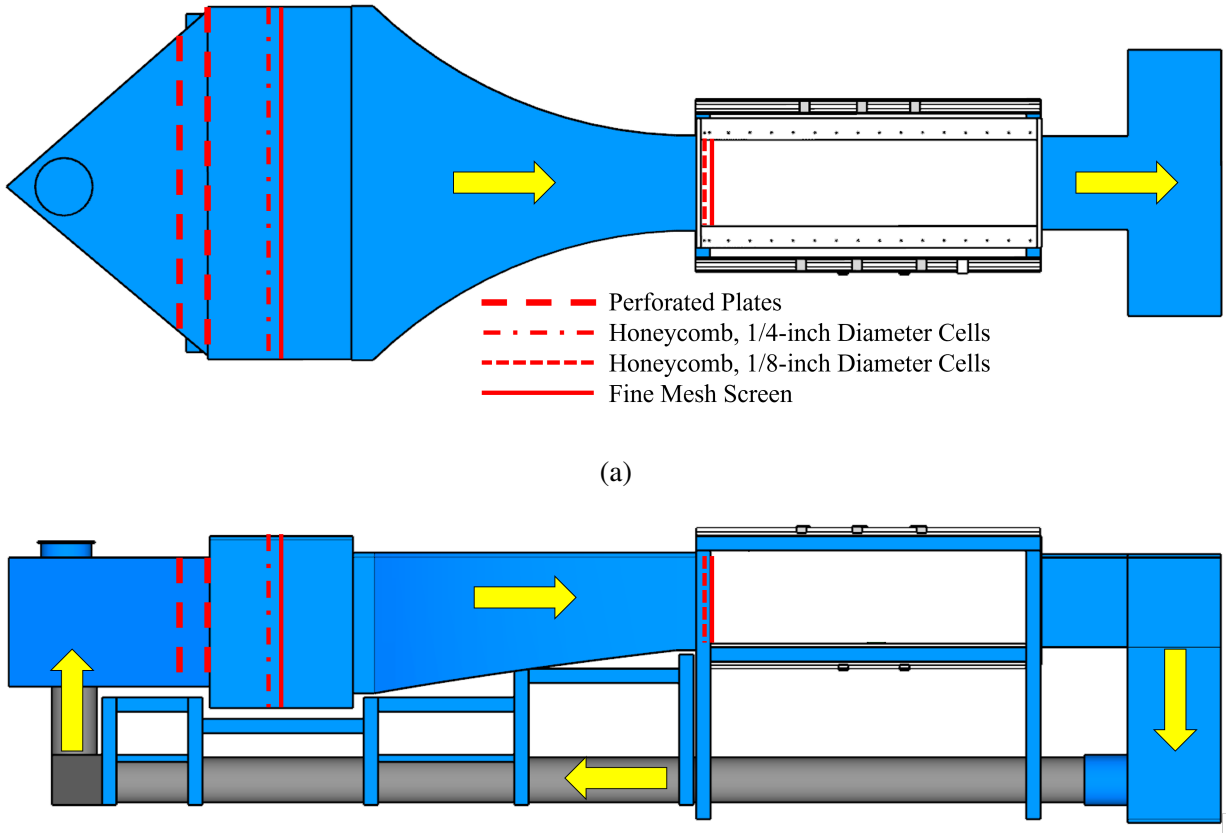

Figure 2.1: **(a)** Plan view and **(b)** side view of the water tunnel facility in TMUAL at MSU shown with the uniform flow configuration in the test section. The arrows depict the flow direction.

through the efforts of Smiljanovski (1990) and Brown (1992). Whereas Gendrich (1999) and Bohl (2002) used a shorter $AR = 4.0$ version of this airfoil mounted horizontally in the test section with false walls, the longer airfoil used for this study is held from one end vertically into the test section. To increase the stiffness of the airfoil in this orientation for the work of Hammer et al. (2019), it was internally reinforced with five 5/16-inch-diameter unidirectional carbon fiber rods and three VeroWhite 3D-printed ribs, as shown in Fig. 2.2. The airfoil tip has a brass insert cap at one end, and an aluminum mounting insert with an end cap at the other.

Suspended into the test section are two $0.95 \times 61 \times 68.6$ cm "skimmer" plates, as shown in Fig. 2.3. The plates rest level on the free surface to maintain a well-defined boundary condition on the mounting side of the airfoil, and to mitigate surface disturbances from airfoil motion. The plates are separated by 4.4 cm in the streamwise direction to permit space for the airfoil shaft to

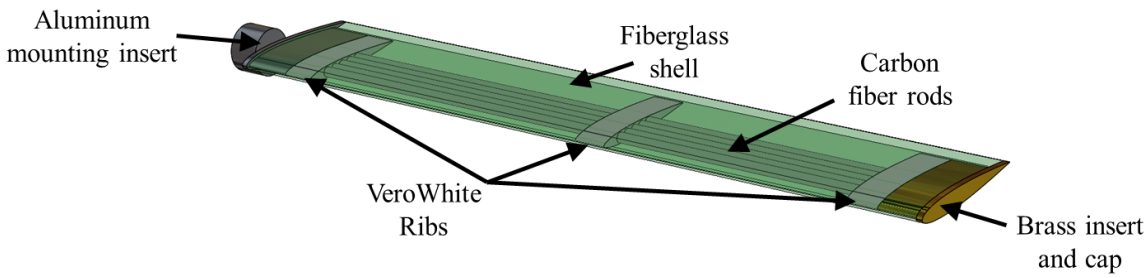

Figure 2.2: NACA 0012 3D model, shown with a transparent shell to see the internal structure.

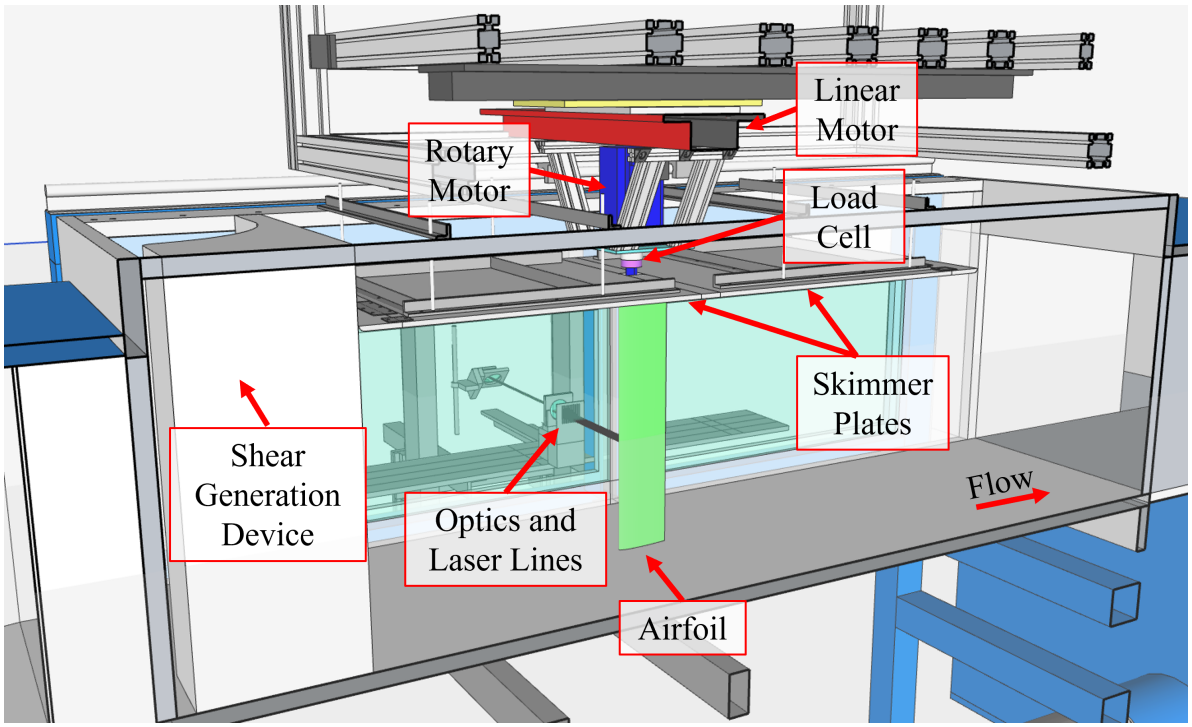

Figure 2.3: Water tunnel test section experimental setup.

translate across the width of the test section, since the plunging motion is lateral to create the scenario depicted in Fig. 1.1 for shear flow. The gaps between the airfoil upper tip and the skimmer plates, and the airfoil lower tip and water tunnel floor, are kept to less than 0.75 mm. The small tip gaps ensure 3D effects are minimized and in conjunction with the $AR = 5.1$ airfoil allow for the current study to be a good approximation for the 2D case. Full optical access in the visible spectrum is permitted on the sides and bottom of the test section through the acrylic walls. Two 41 $\times$ 84 cm quartz windows are installed on one side of the test section that permit ultraviolet (UV) light transmission through the wall.

2.2 Shear Generation Method

The current study uses a variable-length honeycomb method, as introduced by Kotansky (1966) and improved by Safaripour et al. (2016) and Safaripour-Tabalvandani (2020), placed at the test section entrance (see Fig. 2.3) to generate shear in the water tunnel. Shaped honeycombs can be fabricated with custom velocity profiles and low temporal velocity fluctuations. The current honeycomb, which has been used in several previous studies (Olson et al., 2016; Hammer et al., 2018, 2019), has a 61×61 cm cross-section made up of 3.175-mm-diameter cells and produces the three-segment velocity profile with a central uniform-shear zone, as shown in Fig. 2.4 determined from 1c-MTV (see Appendix A for details). A description of the 1c-MTV method is discussed in a following section. The shear profile in Fig. 2.4 consists of a linear mean velocity profile between high- and low-speed uniform streams. The mean velocity profile produced by the shear generation device, depicted in Fig. 2.4a, is measured approximately 73 cm (230 cell-diameters) downstream from the device exit and approximately $2c$ upstream of the airfoil leading edge. At the water tunnel centerline ($Y/c = 0$), the local approach freestream velocity is $u_0 = 10.1$ cm/s. The mean velocity profile is characterized by a shear layer of width δ/c which is bounded on the high-speed side by the Y/c location within the shear region at which the mean velocity equals the mean velocity in the high-speed uniform stream, and on the low-speed side by the Y/c location within the shear region at which the mean velocity equals the mean velocity in the low-speed uniform stream. A linear fit of the velocity profile within the δ/c range is used to determine the dimensionless shear rate, $K \equiv (du_\infty/dy)(c/u_0)$. For the current honeycomb, these methods yield a shear layer width $\delta/c = 1.7$ and dimensionless shear rate $K = 0.50$. Specifically in the range $-0.5 \leq Y/c \leq 0.5$, where the current experiments are primarily performed, the measured velocity deviates from the linear fit of the velocity by less than 3%. There is a velocity "undershoot" at $Y/c \cong 1$ where the uniform-shear zone transitions to the low-speed uniform flow region. The corresponding FSTI profile shown in Fig. 2.4b remains within 1.5-3% between $-0.5 \leq Y/c \leq 0.5$, while it rises to almost 8% at the velocity undershoot. Three cross-stream positions are used for the comparing the airfoil aerodynamics between uniform flow and shear, which are $Y/c = 0$ and ± 0.5. The flow

parameters at the three positions are summarized in Table 2.1, noting that the flow parameters are similar in uniform flow except that $K = 0$ and $FSTI = 1.8\%$ at each position.

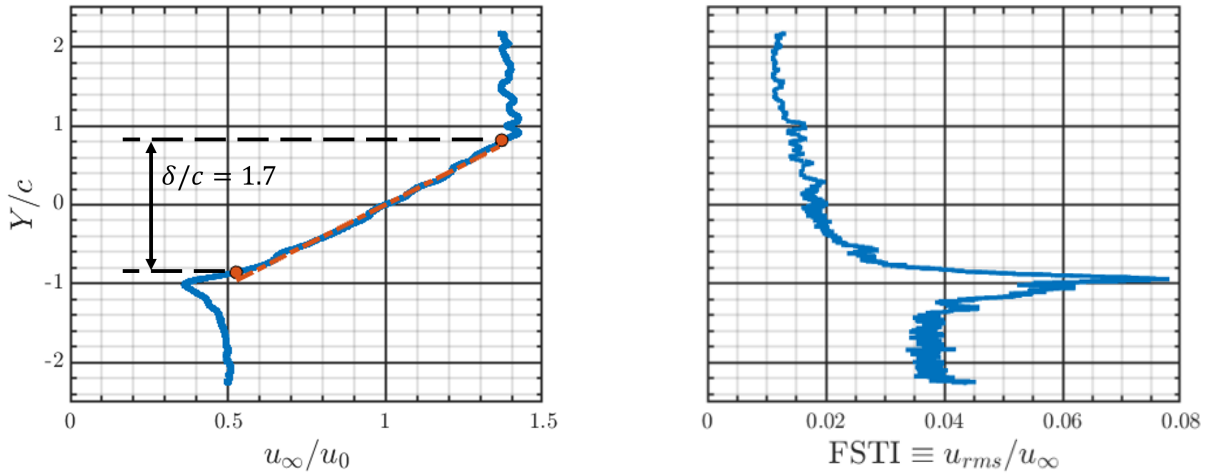

(a) (b)

Figure 2.4: **(a)** Freestream shear flow mean velocity and **(b)** FSTI profiles relative to the water tunnel centerline ($Y/c = 0$, $u_0 = 10.1$ cm/s) obtained by 1c-MTV. The red circles indicate the extent of the shear layer width δ/c and the red line indicates the linear fit within δ/c which gives $K \equiv (du_\infty/dy)(c/u_0) = 0.5$.

Y/c	Re_c	K	u_0 (cm/s)	$FSTI$ (%)
0.5	16500	0.40	12.4	1.6
0	13500	0.50	10.1	1.8
-0.5	9800	0.69	7.3	2.3

Table 2.1: Freestream flow parameters in shear flow acquired via 1c-MTV measurements $2c$ upstream of the airfoil leading edge. The uniform flow parameters are similar to those in shear except that $K = 0$ and $FSTI = 1.8\%$ at each position.

2.3 Airfoil Motion System

2.3.1 Equipment Description

To perform the plunging motion, the current study utilizes a three degree of freedom servo motion system[1] capable of pitch, plunge, and surge motions. The current study uses the pitch and plunge motions (see Figs. 2.3 and 2.5) which are driven by a Parker rotary servo motor (MPP1154A9D-KPSN) and a Parker Trilogy I-FORCE ironless motor positioner (T4DB0436NPAMA4), respectively. The airfoil is mounted about its quarter-chord to the shaft of the pitch motor that has an angular position resolution of 0.003°. The rotary motor is mounted to the linear positioner that has a linear position resolution of 1 μm. The motor and positioner are each driven by their own Parker Aries drive (AR-13AE), and both are controlled with a Parker ACR9000 controller (9000P1U4M1).

2.3.2 Plunging Airfoil Motion Profile and Dynamics

For moving airfoil measurements, the airfoil starts from rest at $1.5c$ (18 cm) above the water tunnel centerline in the high-speed uniform stream. An airfoil starting from rest is typically associated with flow transients, which are undesired for the current study. To ensure the airfoil reaches steady state prior to entering the shear region, the current study utilizes a tailored motion profile (TMP) to maintain a constant α_{eff} through the acceleration phase in the high-speed uniform stream. In the motion profile, the airfoil geometric angle of attack α and linear acceleration are coordinated such that the change in α_i from linear acceleration is counteracted by pitching the airfoil, resulting in constant α_{eff}. By mitigating the transients in the measured load, this technique allows for the airfoil to plunge at higher speeds in this study. The coordinated pitch and acceleration stop once the prescribed steady velocity V_a and α for the plunge are reached. The prescribed V_a and α are chosen to obtain the desired V_r and α_{eff}, respectively, based on the flow conditions at the centerline. Once the airfoil reaches steady velocity, it continues across the water tunnel before coming to rest at -1.5c

[1]The original design, assembly, and testing of the system were done to varying degrees by Dr. Bruno Monnier and Dr. David Olson. See Olson (2017) for more details.

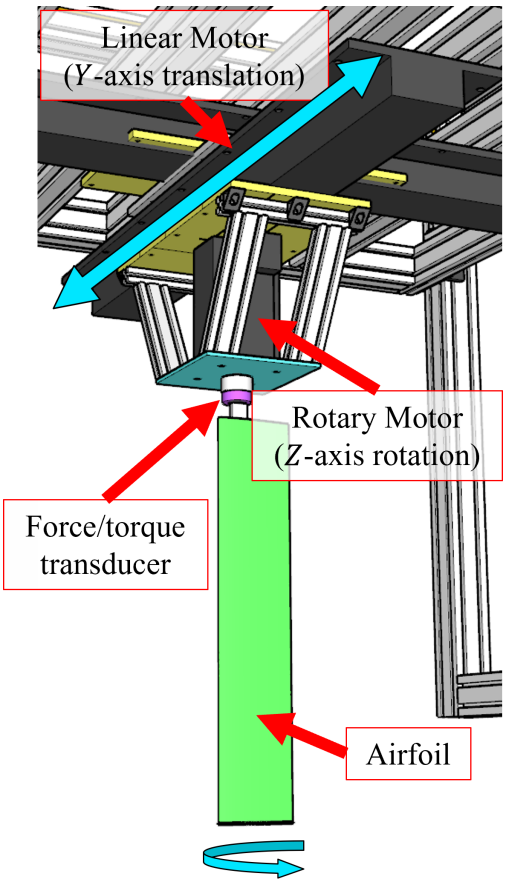

Figure 2.5: Motion and force measurement systems. Blue arrows denote the axes of motion.

relative to the centerline. The total motion stroke corresponds to 59% of the test section width. The plunge speeds used in this study are chosen to explore the range of V_r similar to the typical glide slope of 3-7° for a jet landing on an aircraft carrier, which corresponds to $V_r \approx 0.05$-0.12 (Kaul et al., 1980; Cook et al., 2010; Kelly et al., 2016; Watson et al., 2019).

The dynamics of the downstroke portion of the airfoil motion profile are exemplified by the parameters in Figs. 2.6-2.13 for the cases of $V_a = 0.5$ and 1.0 cm/s in shear flow, in which the intended centerline parameters are $V_r = 0.05$ and 0.1, respectively, and $\alpha_{eff} = 2.5°$. The effect on the aerodynamic load measurements from using the TMP will be discussed in the following section. The results in Figs. 2.6-2.13 are from the measured phase-averaged data acquired during the plunging procedure described in the next section. Figure 2.6 shows the plunging airfoil position versus time, with the linear acceleration region starting at $t = 0$ and ending at point A, before the start of the shear region at point B. It is observed from the angle of attack parameters in Figs.

2.7-2.9 that the TMP coordinates α and α_i to maintain α_{eff} in the linear acceleration region. The airfoil continues its plunge with constant V_a and α between points A-E. At the centerline, point C, Figs. 2.9a and 2.11a show the desired α_{eff} and V_r values, respectively, of the two cases are also achieved.

The complexity of the plunging airfoil in shear problem is demonstrated by the spatial and temporal changes in the chord Reynolds number Re_c, dimensionless shear rate K, and velocity ratio V_r shown in Fig. 2.11-2.13. Note in Fig. 2.13 that the K values are not calculated in the high- and low-speed uniform streams of the flow profile. The Re_c, K, and V_r here are calculated based on the freestream velocity profile $u_\infty(Y)$, since the contribution to u_{eff} by the plunging airfoil motion is small. For example, in Fig. 2.11a at Y/c = -1 where $V_r \approx 0.28$ is the maximum for the faster plunging case, from Eq. 1.3 the effective freestream velocity only varies by $\sqrt{1+{V_r}^2} \approx \sqrt{1+0.28^2} \approx 1.04$, or about 4%. This exercise demonstrates how the current study falls on the lower end of unsteadiness in the context of other literature and why the current study is motivated to analyze the experiments in the quasi-steady limit.

The low unsteadiness is further demonstrated by considering the dimensionless pitch rate of the airfoil, characterized by $\Omega^* \equiv \dot{\alpha}c/2u_0$, which is typically used in the context of dynamic stall (McCroskey, 1982; Carr, 1988). Though the airfoil is not being actively pitched after reaching its prescribed V_a and α, the local approach velocity u_0 changes in time while it is plunging through the shear freestream. The time-varying u_0 corresponds to a time-varying α_i and therefore an apparent pitching from the reference frame of the airfoil. This is derived in Eq. 2.1-2.3, noting that du_0/dt < 0 and du_∞/dY < 0 during the airfoil plunge from the high- to low-speed uniform streams such that a mathematically consistent Ω^* > 0 is produced. Typically $V_r^2 \ll 1$, which allows for Ω^* to be approximated by Eq. 2.4.

$$\dot{\alpha} \equiv \frac{d\alpha_{eff}}{dt} = \frac{d}{dt}(\alpha + \alpha_i) = \frac{d}{dt}\tan^{-1}\left(\frac{V_a}{u_0}\right) \tag{2.1}$$

$$\dot{\alpha} = -\frac{1}{1+\left(\frac{V_a}{u_0}\right)^2}\frac{V_a}{u_0^2}\frac{du_0}{dt} = -\frac{1}{1+\left(\frac{V_a}{u_0}\right)^2}\left(\frac{V_a}{u_0}\right)^2\frac{du_\infty}{dY} \tag{2.2}$$

$$\Omega^* \equiv \frac{\dot{\alpha}c}{2u_0} = -\frac{1}{1+V_r^2}V_r^2\frac{du_\infty}{dY}\frac{c}{2u_0} \tag{2.3}$$

$$\Omega^* \equiv \frac{\dot{\alpha}c}{2u_0} \approx \frac{V_r^2 K}{2} \tag{2.4}$$

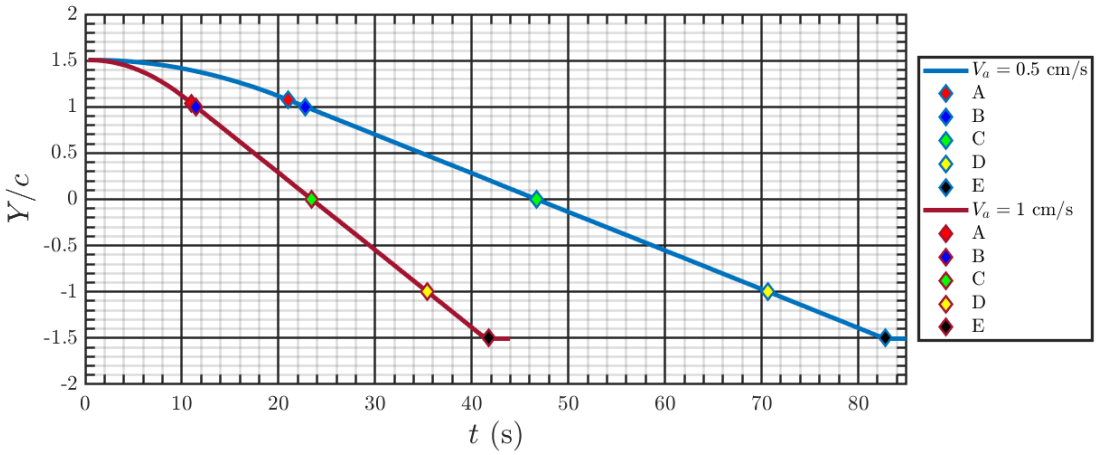

Figure 2.6: Phase-averaged cross-stream position history Y/c versus time t for the plunging airfoil in shear flow with the tailored motion profile. In this example, the intended centerline parameters are V_r = 0.05 and 0.1, for V_a = 0.5 and 1.0 cm/s, respectively, and α_{eff} = 2.5° for both plunge speeds. Time t = 0 corresponds to the instant when the airfoil starts moving from rest after waiting for the flow to reach steady state. The diamond symbols correspond to the instances of the motion profile at which the airfoil: (A) reaches steady V_a, (B) enters the shear region, (C) passes the tunnel centerline, (D) exits the shear region, and (E) stops all motion.

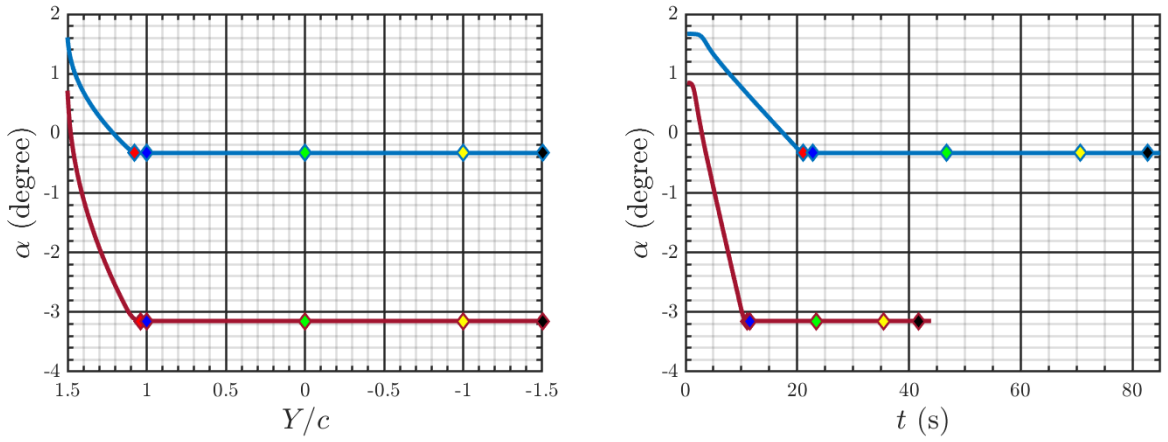

Figure 2.7: Phase-averaged geometric angle of attack α versus **(a)** cross-stream position Y/c and **(b)** time t for the plunging airfoil in shear flow with the tailored motion profile. In this example, the intended centerline parameters are V_r = 0.05 and 0.1, for V_a = 0.5 and 1.0 cm/s, respectively, and α_{eff} = 2.5° for both plunge speeds. Time t = 0 corresponds to the instant when the airfoil starts moving from rest after waiting for the flow to reach steady state. The diamond symbols correspond to the instances of the motion profile at which the airfoil: (A) reaches steady V_a, (B) enters the shear region, (C) passes the tunnel centerline, (D) exits the shear region, and (E) stops all motion.

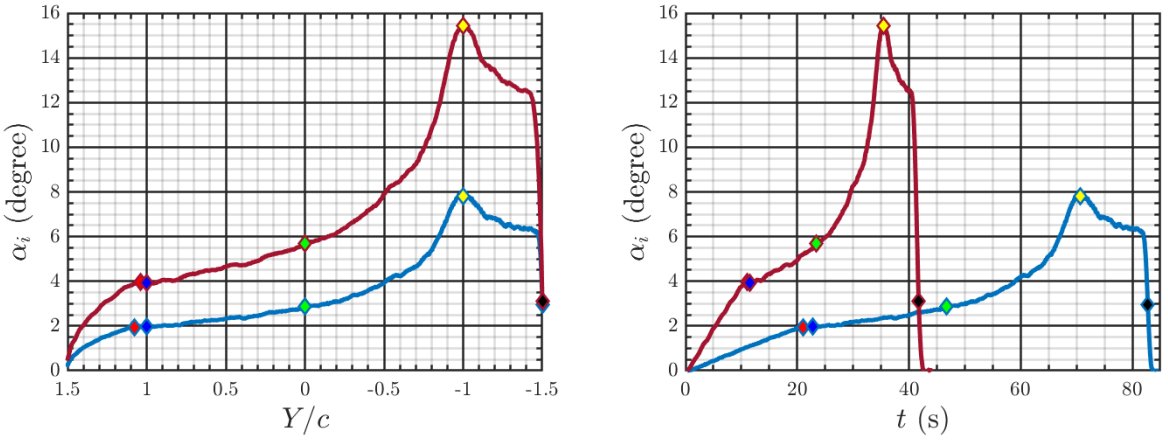

Figure 2.8: Phase-averaged induced angle of attack α_i versus **(a)** cross-stream position Y/c and **(b)** time t for the plunging airfoil in shear flow with the tailored motion profile. In this example, the intended centerline parameters are V_r = 0.05 and 0.1, for V_a = 0.5 and 1.0 cm/s, respectively, and α_{eff} = 2.5° for both plunge speeds. Time t = 0 corresponds to the instant when the airfoil starts moving from rest after waiting for the flow to reach steady state. The diamond symbols correspond to the instances of the motion profile at which the airfoil: (A) reaches steady V_a, (B) enters the shear region, (C) passes the tunnel centerline, (D) exits the shear region, and (E) stops all motion.

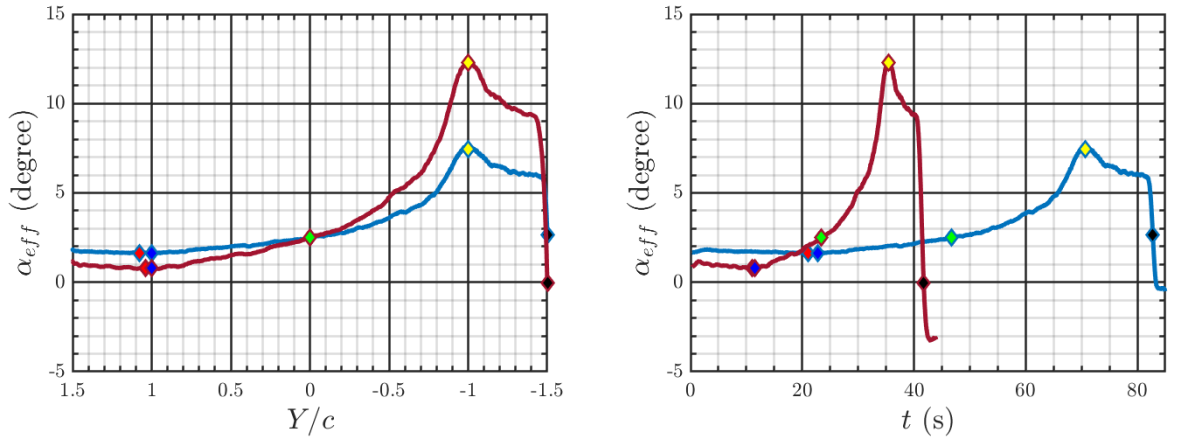

(a) (b)

Figure 2.9: Phase-averaged effective angle of attack α_{eff} versus **(a)** cross-stream position Y/c and **(b)** time t for the plunging airfoil in shear flow with the tailored motion profile. In this example, the intended centerline parameters are V_r = 0.05 and 0.1, for V_a = 0.5 and 1.0 cm/s, respectively, and α_{eff} = 2.5° for both plunge speeds. Time t = 0 corresponds to the instant when the airfoil starts moving from rest after waiting for the flow to reach steady state. The diamond symbols correspond to the instances of the motion profile at which the airfoil: (A) reaches steady V_a, (B) enters the shear region, (C) passes the tunnel centerline, (D) exits the shear region, and (E) stops all motion.

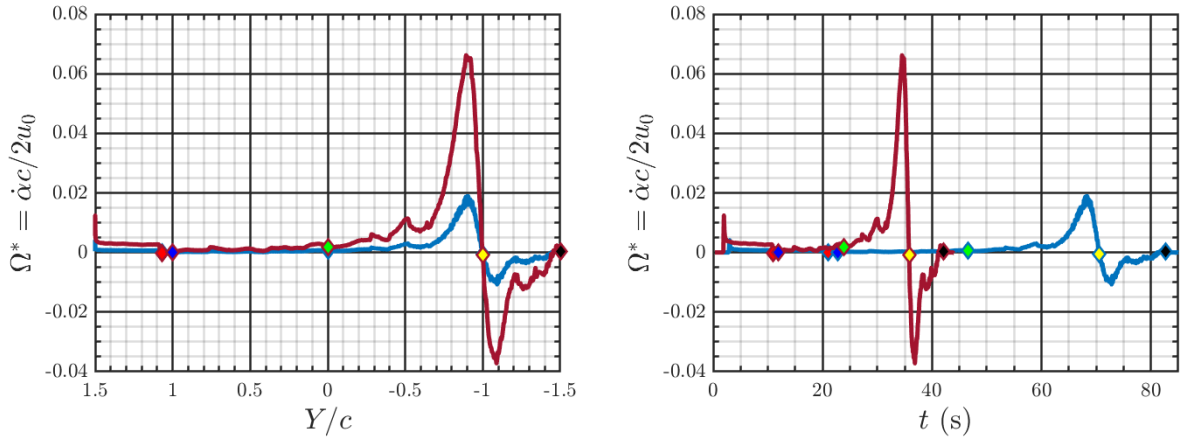

Figure 2.10: Phase-averaged dimensionless pitch rate $\Omega^* = \dot{\alpha}c/2u_\infty$ versus **(a)** cross-stream position Y/c and **(b)** time t for the plunging airfoil in shear flow with the tailored motion profile. In this example, the intended centerline parameters are V_r = 0.05 and 0.1, for V_a = 0.5 and 1.0 cm/s, respectively, and α_{eff} = 2.5° for both plunge speeds. Time t = 0 corresponds to the instant when the airfoil starts moving from rest after waiting for the flow to reach steady state. The diamond symbols correspond to the instances of the motion profile at which the airfoil: (A) reaches steady V_a, (B) enters the shear region, (C) passes the tunnel centerline, (D) exits the shear region, and (E) stops all motion.

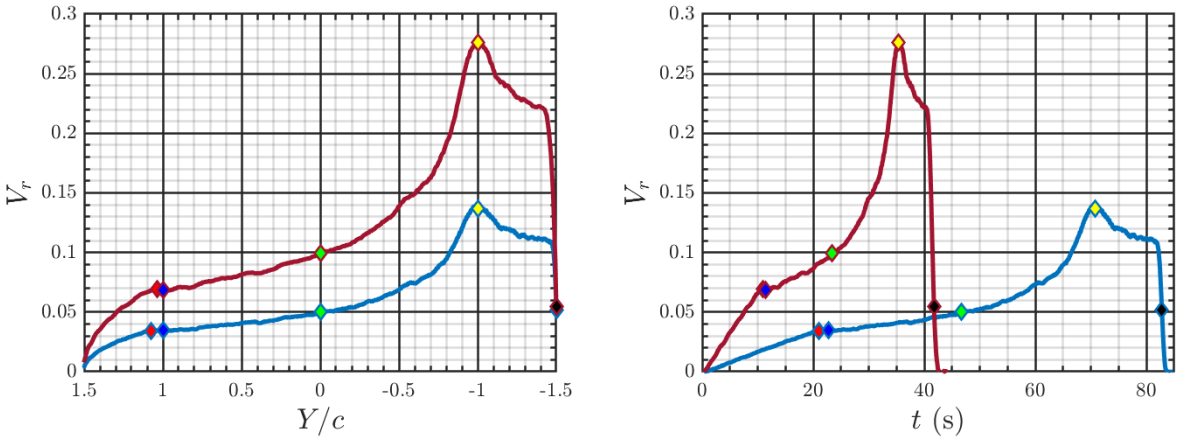

(a) (b)

Figure 2.11: Phase-averaged plunging velocity ratio V_r versus **(a)** cross-stream position Y/c and **(b)** time t for the plunging airfoil in shear flow with the tailored motion profile. In this example, the intended centerline parameters are V_r = 0.05 and 0.1, for V_a = 0.5 and 1.0 cm/s, respectively, and α_{eff} = 2.5° for both plunge speeds. Time t = 0 corresponds to the instant when the airfoil starts moving from rest after waiting for the flow to reach steady state. The diamond symbols correspond to the instances of the motion profile at which the airfoil: (A) reaches steady V_a, (B) enters the shear region, (C) passes the tunnel centerline, (D) exits the shear region, and (E) stops all motion.

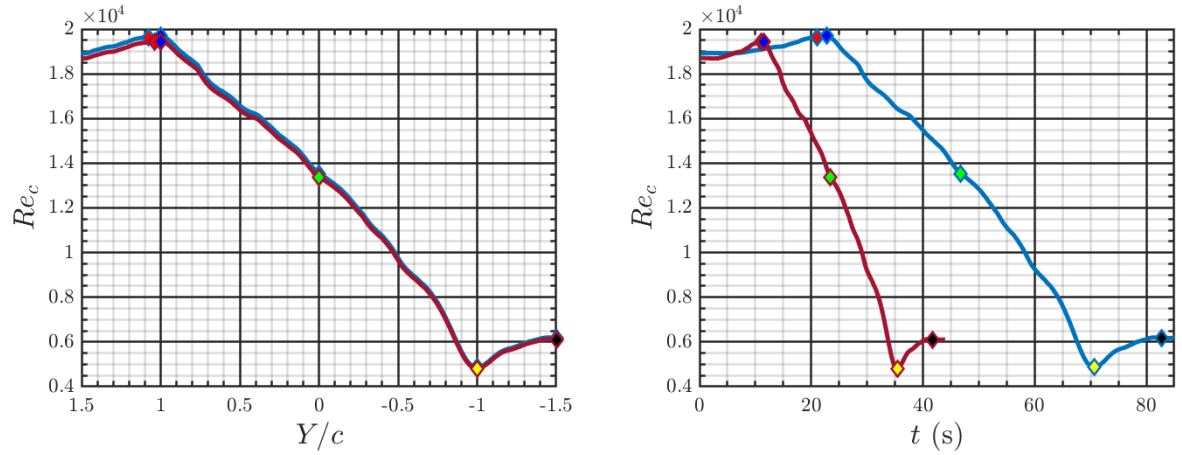

(a) (b)

Figure 2.12: Phase-averaged chord Reynolds number Re_c versus **(a)** cross-stream position Y/c and **(b)** time t for the plunging airfoil in shear flow with the tailored motion profile. In this example, the intended centerline parameters are V_r = 0.05 and 0.1, for V_a = 0.5 and 1.0 cm/s, respectively, and α_{eff} = 2.5° for both plunge speeds. Time t = 0 corresponds to the instant when the airfoil starts moving from rest after waiting for the flow to reach steady state. The diamond symbols correspond to the instances of the motion profile at which the airfoil: (A) reaches steady V_a, (B) enters the shear region, (C) passes the tunnel centerline, (D) exits the shear region, and (E) stops all motion.

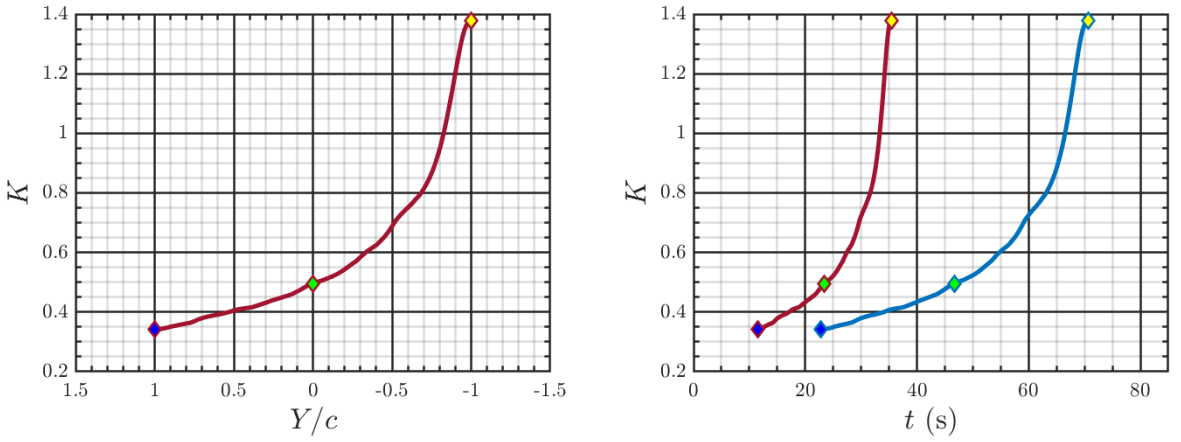

Figure 2.13: Phase-averaged dimensionless shear rate K versus **(a)** cross-stream position Y/c and **(b)** time t for the plunging airfoil in shear flow with the tailored motion profile. In this example, the intended centerline parameters are V_r = 0.05 and 0.1, for V_a = 0.5 and 1.0 cm/s, respectively, and α_{eff} = 2.5° for both plunge speeds. Time t = 0 corresponds to the instant when the airfoil starts moving from rest after waiting for the flow to reach steady state. The diamond symbols correspond to the instances of the motion profile at which the airfoil: (A) reaches steady V_a, (B) enters the shear region, (C) passes the tunnel centerline, (D) exits the shear region, and (E) stops all motion. Note that the K values are not calculated in the high- and low-speed uniform streams of the flow profile.

Figure 2.10 shows the instantaneous Ω^* throughout the two primary plunge cases. From entry into the shear layer at Y/c = 1.0 to the centerline at Y/c = 0 the dimensionless pitch rate $\Omega^* <$ 0.001 for V_a = 0.5 cm/s and $\Omega^* <$ 0.003 for V_a = 1.0 cm/s. From Y/c = 0.5 to Y/c = -0.5 where the current study limits its focus, $\Omega^* <$ 0.003 for V_a = 0.5 cm/s, while for V_a = 1.0 cm/s the pitch rate peaks at $\Omega^* \lesssim$ 0.011. The positions $Y/c <$ -0.5 are not considered due to potential effects of the undershoot region of the flow profile and the tunnel boundary. For context, Francis & Keesee (1985) investigated dynamic stall on the NACA 0012 airfoil pitching about the 31.7% chord point at Reynolds number as low as $Re_c = 7.7 \times 10^4$ and $0.001 \leq k \leq 0.21$, where $k \equiv \Omega^*$. Their results indicate that the C_L history for $\Omega^* \lesssim 0.05$ up to the maximum lift coefficient $C_{L_{max}}$ of the static airfoil is not affected. Another study by Jumper et al. (1987) investigated the lift curve characteristics of the NACA 0015 airfoil pitching at constant rate about its mid-chord. Their results for $Re_c \approx 1.8 \times 10^5$ and $\Omega^* \approx 0.01$ show close agreement in the C_L of the pitching airfoil and

the static airfoil up to about $\alpha = 10^\circ$. In Gendrich et al. (1995), the NACA 0012 airfoil pitching about its quart-chord at $Re = 1.2 \times 10^4$ and $\Omega^* = 0.1$ showed similar agreement and behavior with Francis & Keesee (1985) in the C_L history up to $\alpha = 20^\circ$, suggesting some independence of Reynolds number in the low Reynolds number range.

For the typical glide slope range of 3-7°, $\Omega^* \approx 0.0014K$-$0.0075K$ by Eq. 2.4. The air wake created by an aircraft carrier flight deck and superstructure was modeled by Cherry & Constantino (2010), from whom the dimensionless shear rate is estimated to be $K \approx 0.006$ in the region aft of the full-scale carrier through which landing aircraft fly. The resulting estimate for the dimensionless pitch rate for the landing aircraft is $\Omega^* \approx O(10^{-5})$, which falls into the quasi-steady range in the context of dynamic stall. By comparison, the current study has a similar V_r range as the glide slope of a landing aircraft and therefore a similar relation in approximating Ω^*. However, for $Y/c \geq -0.5$ in the current study the dimensionless shear is $K \approx 0.3$-0.69, i.e., two orders of magnitude greater than for the carrier landing estimate. As will be discussed later, the V_r values used in current study are limited by the effects of the flow transients originating from the airfoil starting from rest and the limited space in the test section to accelerate the airfoil before entering the shear region. Within the V_r limits, the dynamic stall studies discussed above indicate the Ω^* and α ranges observed for $Y/c \geq$ -0.5 are typically low enough that deviations from the static airfoil limit due to pitching ($\dot{\alpha} \rightarrow 0$) are not expected. However, the traditional dynamic stall studies do not consider freestream shear and, as is the purpose of this study to uncover, the effects of the freestream shear on the plunging airfoil are unknown.

2.4 Aerodynamic Load Measurements

The load on the airfoil is measured using an ATI Mini40 six-component force and torque transducer connected to a National Instruments (NI) data acquisition (DAQ) board.[2] The force and torque (F and T, respectively) sensing ranges and resolution of the transducer are given in Table

[2]The ATI Mini40 selection and details regarding its proper implementation were extensively worked out by Dr. David Olson, who also developed the overall stationary airfoil load measurement procedure.

2.2, where subscripts x, y, and z correspond to the sensor axes. The transducer is mounted along the connecting shaft between the rotary motor and the airfoil as shown in Fig. 2.5. The airfoil is cantilevered vertically into the water tunnel whereby the transducer directly measures the forces exerted on the airfoil.

The load on the stationary airfoil at a prescribed α is first recorded with the flow off to zero the load cell. The flow-on measurements are 180 s long and recorded at a rate of 2 kHz. The tunnel is then turned off and another flow-off measurement is acquired once the tunnel reaches a quiescent state. The total time for measurements is set to ensure negligible drift in the sensor's bias while allowing for convergence of the mean force. The mean force coefficient uncertainty is found to be dominated by the sensor drift over the duration of each experiment, taken by the difference between the flow-off measurements at the beginning and end. This uncertainty in C_L or C_D was always less than ± 0.008 among all the stationary airfoil measurements in both uniform flow and shear. Zero α is found by first setting the airfoil parallel to the test section walls and then performing force measurements in uniform flow at the centerline. Zero α is determined by the α where the measured C_L-α curve crosses zero and is found to within an uncertainty $\pm 0.1^\circ$. Consequently, all measurements are referenced to zero α determined at the centerline in uniform flow.

For the plunging airfoil load measurements, the load is first recorded on the stationary airfoil at the centerline and prescribed α with the flow off to zero the load cell. The airfoil then moves to the starting position and α based on the prescribed TMP described previously. The load is

F_i, T_i	Sensing Ranges	Resolution
F_x, F_y	20 N	5 mN
F_z	60 N	10 mN
T_x, T_y	1 N·m	0.125 N·m
T_z	1 N·m	0.125 N·m

Table 2.2: The force (F) and torque (T) sensing capability of the ATI Mini40 transducer. Subscripts refer to the sensor axes. The values are taken from the ATI F/T Transducer Six-Axis Force/Torque Sensor System Installation and Operation Manual, Document No. 9620-05-Transducer Section.

continuously recorded throughout five sets of five individual plunges (i.e., 25 total plunges), which is structured such that the total measurement time of each set allows the drift in the sensor's bias to remain negligible, like for the stationary airfoil experiments. For example, the time between the start of successive strokes for the nominal case of V_r = 0.05 is approximately 135 s. The elapsed time to complete all 25 strokes for a single angle of attack is approximately 1.6 h, which is the limiting factor for completing all experiments in a reasonable time frame. The elapsed time is reduced for higher plunge speeds, but not greatly due to the need to reposition the airfoil and reach steady state prior to each successive plunge. During motion, the airfoil tip oscillates at the airfoil structural frequency, and optical measurements of these oscillations show the amplitude to be less than 0.5% of the chord. The load as a function of time is temporally filtered to remove influence of these oscillations on the load history, which also reduces the high-frequency noise content of the measurement. All the plunge strokes are phase averaged relative to the start of motion at the beginning of each downstroke.

Though zeroing the load cell is performed initially, the load cell readings are dependent on the distributed weight of the airfoil, which varies slightly with position along the plunge stroke and angle of attack. This variation is accounted for using the calibration procedure described in Appendix B, such that the load cell may be zeroed as a function of α and Y/c at every instant along the airfoil trajectory relative to the centerline. There is also an effect of cross-stream position on the local zero-lift angle of attack ($\alpha_{L=0}$) and the C_L and C_D at zero α due to presence of the test section boundaries, which is discussed in Appendix C. The highlight of Appendix C is that the magnitude of the variation in $\alpha_{L=0}$ between -0.5 $\leq Y/c \leq$ 0.5 is approximately 0.06°, which is less than the uncertainty in α. Consequently, the shift in the local $\alpha_{L=0}$ is deemed negligible for the purpose of comparing the time- or phase-averaged load measurements in uniform or shear flow at each of the three cross-stream positions investigated. Furthermore, the magnitude of the variations in C_L and C_D at zero α over the range -1.5 $\leq Y/c \leq$ 1.5 are less than 0.0062 and 0.0033, respectively, compared to the plunging airfoil measurement uncertainty in C_L of ±0.06 and C_D of ±0.02 (described next). As such, the variation in C_L and C_D over the relevant measurement range

of is also neglected for the purpose of this study.

The uncertainty in the load measurements at each point along the trajectory is estimated by the standard deviation of the phase averaged load. With each plunge considered independent, the resulting uncertainty estimate in the force coefficients are typically less than $C_L = \pm 0.06$ and $C_D = \pm 0.02$ for u_0 = 10.1 cm/s and V_r = 5%. The uncertainty is sometimes greater than these estimates at higher angles of attack and at the lowest Reynolds number investigated, but in all cases is quantified by the uncertainty bars on each data point in the phase averaged load results. The estimated uncertainty in α_{eff} for the plunging airfoil is determined by the combined uncertainty in the geometric angle of attack (about 0.1°) and α_i. The uncertainty in α_i is a function of V_r and so is dependent on the fluctuation in the freestream velocity which may be given by the u_{rms} results in Fig. 2.4b. Conservatively using the results at Y/c = -0.5, where u_0 = 7.3 cm/s and FSTI ≅ 2.5%, and the highest plunge speed of V_a = 1 cm/s, the α_i is found to vary by ±0.2°. Therefore, the estimated uncertainty in α_{eff} is less than ±0.3° for over the range of plunge speeds for the three cross-stream positions, noting that the uncertainty in α_{eff} decreases as V_r or FSTI decrease.

The loads on the moving airfoil are recorded in the reference frame aligned with the x, y axes at the airfoil quarter-chord. A Galilean transformation is applied to the recorded loads to convert to the reference frame of the moving airfoil given by the (x', y') axes, as discussed in Chapter 1 using Eq. 1.4 and shown in Fig. 1.2. This enables comparison of the load on the plunging airfoil with the mean load measurement on the stationary airfoil at the same Y/c position and α_{eff} under the same flow conditions.

The tailored motion profile (TMP) described in the previous section enables investigation of higher plunge speeds while minimizing the effects of flow transients due to the airfoil starting from rest. In Fig. 2.14, the spatial history of the C_L on the plunging airfoil in uniform flow with the TMP is compared to that without the TMP. The Reynolds number $Re_c = 1.77 \times 10^4$ and plunge speed V_a = 0.9 cm/s (V_r = 0.07 cm/s) are chosen since they correspond to similar Re_c and V_r for the airfoil in the high-speed uniform stream of the shear profile prior to entering the shear zone (see Fig. 2.12a and 2.11a). As Fig. 2.14 shows, the transients associated with the airfoil starting

from rest are reduced to within 5% the steady state load at $Y/c = 1$, which is the location at which the linear shear region starts in shear flow. In other words, for the airfoil plunging in shear flow, utilizing the TMP effectively eliminates undesired flow transients prior to the airfoil entering the shear region and demonstrates the ability setup to perform measurements at higher V_r than without the TMP. Even with the TMP, the measurements are limited by the flow transients as the target V_r increases. This is demonstrated in Fig. 2.15 which shows the phase averaged C_L spatial history on the plunging airfoil using the TMP in $Re_c = 1.35 \times 10^4$ uniform flow at four different V_r and a nominal $\alpha_{eff} = 7.6°$. It is observed in Fig. 2.15 that the flow transients have a stronger influence on the C_L for $Y/c \geq 1$ as the V_r increases. The flow transient influence is expected to be even stronger at higher V_r and angles of attack, which also become greater influenced by the proximity to the test section wall. Therefore, performing the type of measurements in the current study to reach $V_r > 0.15$ prior to stopping the airfoil pitching and linear acceleration at $Y/c \approx 1.08$ is unlikely to sufficiently reduce the flow transients. It is also observed in Fig. 2.15 that there is still variation between the C_L histories at the different V_r for $Y/c < 1$. However, noting the scale of the ordinate axis and recalling the uncertainty in the phase-averaged C_L on the plunging airfoil is approximately ± 0.06, the C_L histories show much closer agreement than would otherwise be expected without the TMP being employed.

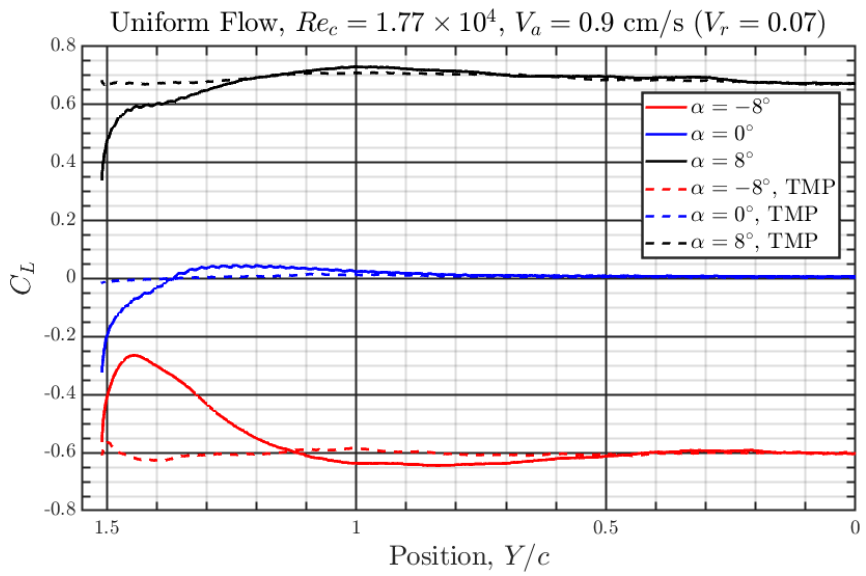

Figure 2.14: Lift coefficient on the plunging airfoil in uniform flow with the tailored motion profile (dashed lines) and without the tailored motion profile (solid lines) at the start to maintain constant α_{eff}. The Reynolds number $Re_c = 1.77 \times 10^4$ and plunge speed $V_a = 0.9$ cm/s ($V_r = 0.07$ cm/s) correspond to the similar Re_c and V_r for the airfoil in the high-speed uniform stream of the shear profile.

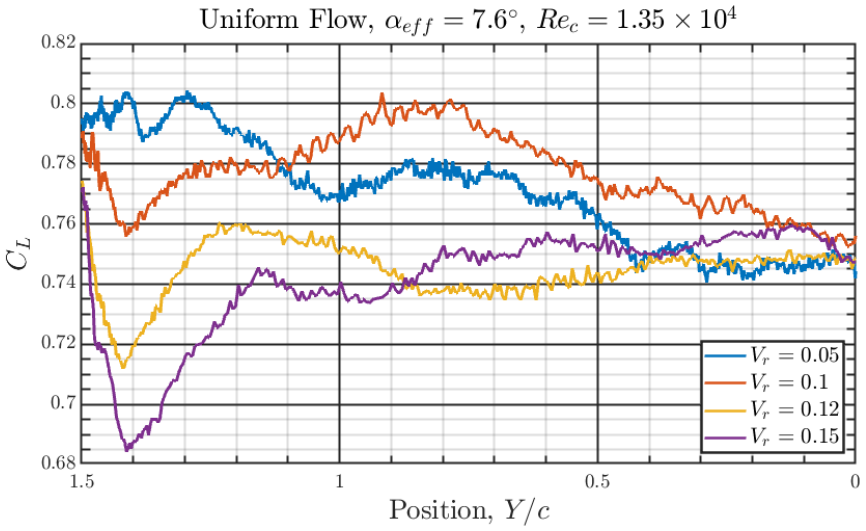

Figure 2.15: Lift coefficient on the plunging airfoil in uniform flow ($Re_c = 1.35 \times 10^4$) utilizing the tailored motion profile for a nominal $\alpha_{eff} = 7.6°$ and four different V_r.

2.5 Molecular Tagging Velocimetry

2.5.1 Background

The current study utilizes molecular tagging velocimetry (MTV) to investigate the flow around the airfoil. Molecular tagging velocimetry is a whole-field non-intrusive optical technique in which the flowing medium is premixed with molecules that can be turned into long-lifetime tracers upon excitation by photons of an appropriate wavelength (Gendrich et al., 1997; Koochesfahani & Nocera, 2007). The water tunnel facility contains a water-soluble phosphorescent supramolecule tracer (Gendrich et al., 1997) whose chemical composition nominally consists of: 1×10^{-4} M of maltosyl-β-cyclodextrin, 0.055 M of cyclohexanol, and a saturated solution of 1-bromonaphthalene ($\sim 1 \times 10^{-5}$ M). The lifetime of the current solution was measured to be $\tau \cong 4.0$ ms, where τ refers to the time when the emission has decayed to 37% (e^{-1}) of its initial intensity. Pulsed laser beams are used to "tag" regions of interest containing the phosphorescent supramolecule tracer and the resulting emission is interrogated twice with a prescribed time delay to form an image pair (Gendrich et al., 1997). The displacement of the tagged region between the two interrogation times determines the Lagrangian displacement vector which provides the estimate of the velocity vector. A comprehensive review of MTV development, photochemistry, and applications can be found in Koochesfahani & Nocera (2007).

2.5.2 Current Implementation

The current study requires measurement of the flow near the airfoil surface to characterize the boundary layer and such that the entire airfoil surface is included in a single frame. Using single-component MTV (1c-MTV) affords the ability to meet the requirements of this study, by which the streamwise component of the flow around the airfoil is measured at every pixel along the tagged lines with high spatial resolution. Here 1c-MTV is implemented using a Coherent COMPexPro 205C XeCl 308nm excimer laser as the excitation source with a pulse width of 20 ns. The beam path from the laser is shown in Fig. 2.16. The optical assembly depicted in Fig. 2.16b-c enables

the tagging pattern to be positioned independently in the streamwise, cross-stream and vertical directions.

The beam originates from the laser and is directed by a series of mirrors where it travels parallel to the test section. The beam is then directed vertically by a mirror through two focusing lenses which form the beam into a sheet less than 1 mm thick in the test section. The vertically traveling laser sheet is then reflected by a mirror such that it travels perpendicularly toward the test section and through a lens which expands the laser sheet. The expanded laser sheet passes through a brass beam blocker which has vertical slots to form the desired tagging pattern. After passing through the beam blocker, the sheet of laser lines enters the test section through the quartz window. A total of 51 lines are produced, of which 46 are typically incident on the airfoil surface at its midspan where they are spaced approximately 2.63 mm ($0.022c$) apart. The remaining few non-incident lines fall just upstream and downstream of the airfoil. Each line has a full-width ($1/e^2$ point) of approximately 1.8 mm and thickness less than 1 mm in the spanwise direction of the airfoil. In this implementation, UV optical access is only possible from the side of the test section with the quartz windows, which limits the flow measurements to only one side of the airfoil. In the default arrangement, the flow may be measured over the suction surface of the airfoil at positive α or the pressure surface at negative α, the latter of which is not considered in this study. Though the current setup may be modified by reversing the orientation of the shear device and allowing measurement on the opposite side of the airfoil, such as in Safaripour-Tabalvandani (2020), it is not done in the current study due to the additional measurement time it requires. For the purposes of this study, the flow measurements are only performed on the suction side of the airfoil at positive α, while flow measurements on the suction surface at negative α or the pressure surface at either positive or negative α are left for future work.

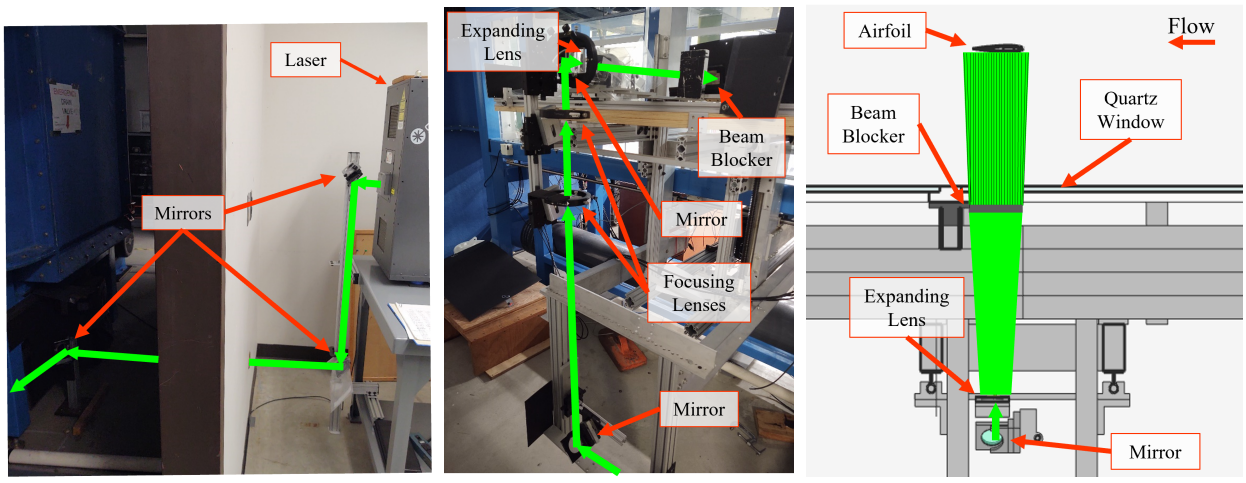

(a) (b) (c)

Figure 2.16: Laboratory 1c-MTV optical setup showing **(a)** the laser beam (represented in green) originating from the laser and being directed by mirrors to **(b)** the sheet-forming and expanding optics. The beam then passes through **(c)** the beam blocker which turns the sheet into many lines that enter the tunnel through the upstream quartz window.

2.5.3 Single-Component MTV Imaging Methods

To acquire the 1c-MTV data in a single frame, a pco.dimax S4 camera with a Nikon Nikkor 58mm f/1.2 lens is mounted beneath the water tunnel pointing upwards into the test section, as shown in Fig. 2.17. The pco.dimax S4 is a 12 bit complementary metal-oxide-semiconductor (CMOS) camera with a 2016 $\times$ 2016 pixel monochrome sensor, which can capture up to 1279 frames per second at full resolution. For this study, the field of view is cropped to 1776 pixel $\times$ 1536 pixel (13.72 cm $\times$ 11.87 cm) in this study and a resolution of 77.28 μm/pixel is achieved. The camera can be positioned independently in the streamwise, cross-stream and vertical directions by way of a traverse system. The camera traverse system indicated in the figure is for the cross-stream direction, which allows for 1c-MTV at the three primary Y/c positions.

Image pairs are captured by triggering the camera with two successive transistor-transistor-logic (TTL) pulses separated by the prescribed delay time Δt; i.e., each pulse corresponds to one image in the pair. The pulses are generated by the series of steps outlined in Appendix D. The camera is operated in correlated double image (CDI) mode, in which a reference image is

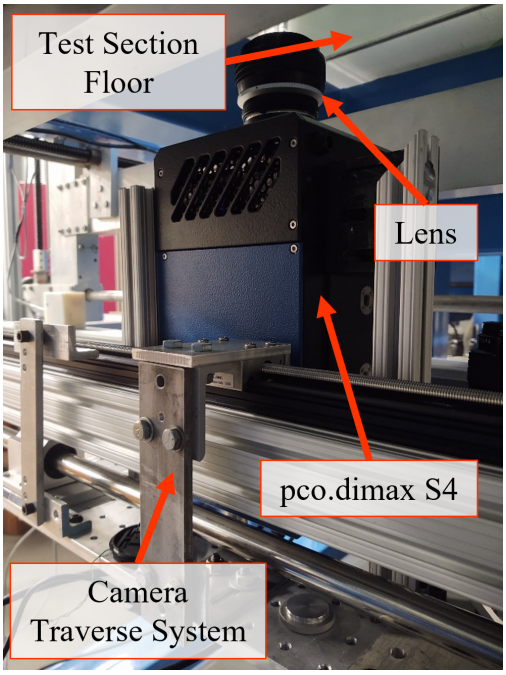

Figure 2.17: Photograph of the pco.dimax S4 CMOS camera with a Nikon Nikkor 58mm f/1.2 lens mounted beneath the water tunnel looking upwards through the test section floor. The camera can be positioned independently in the streamwise, cross-stream and vertical directions. The camera traverse system indicated in the figure is for the cross-stream direction, which allows for 1c-MTV at the three primary Y/c positions investigated in this study.

acquired immediately before each exposed image and used to compensate for dynamic noise. The consequences of using CDI mode are that images are recorded with increased dynamic range and improved performance on the low-intensity side of the images, but at the expense of half of the normal frame rate. Additional details about CDI mode are discussed in Appendix D.

The first image in the pair set to acquire 1 μs after the laser pulse to avoid the fluorescent light emission of the tagged regions. The images in each pair are separated by delay time Δt = 6 ms and use an exposure time t_e = 600 μs. For stationary airfoil measurements, the image pairs are acquired at a rate of 5.87 Hz. A representative image pair recorded under these conditions for α = 6° is shown in Fig. 2.18. The corresponding displacement of the freestream flow in this example is approximately 9 pixel (0.6%c). In Fig. 2.18b, the convection of the flow during the delay time is evident from the deformations in the tag lines relative to the tag lines in 2.18a.

The images are processed using the 1D implementation of the original 2D correlation technique used for processing two-component MTV data as in Gendrich et al. (1997). The procedure, based

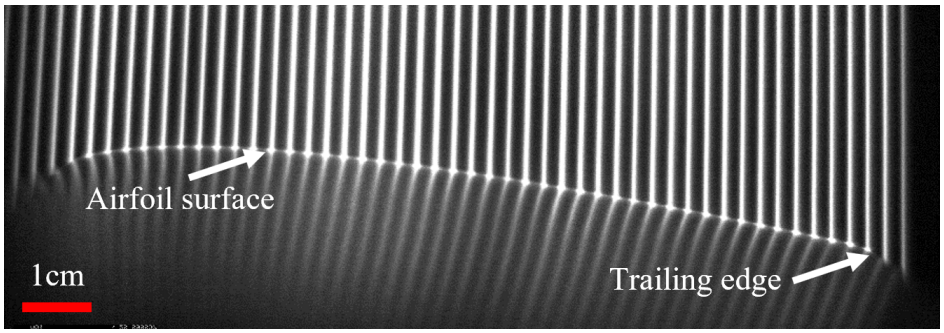

(a)

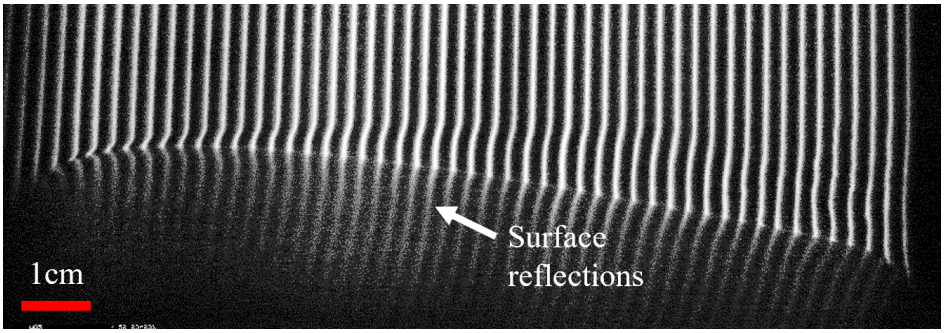

(b)

Figure 2.18: Instantaneous images of the 1c-MTV beam lines for the stationary airfoil at $\alpha = 6°$: **(a)** 1 μs after the laser pulse, and **(b)** $\Delta t = 6$ ms later. Both images are 1776×614 pixel ($1.14c \times 0.40c$), and the flow is from left to right.

on that of Chee (2005) and Katz (2010) and improved upon by Olson (2011), performs a line-by-line, row-by-row cross correlation between the intensity fields of the initial and displaced tagged lines. It then uses a 7th order polynomial fit to find the peak of the correlation map with sub-pixel accuracy. Olson (2011) proposed removing the contributions of white noise, from both camera and processing, to the fluctuating velocity measurements by using autocorrelation of the instantaneous velocity time-series, which is employed in this study.

There is an inherent error in 1c-MTV measurements due to the assumption of unidirectional flow and corresponding inability to measure the flow parallel to the laser lines which, from Hill & Klewicki (1996), can be calculated by:

$$\frac{\Delta u}{u} = \Delta t \left(\frac{v}{u} \frac{\partial u}{\partial y} \right) \tag{2.5}$$

In Eq. 2.5, u and v are the estimated velocity components normal and parallel to the tag line,

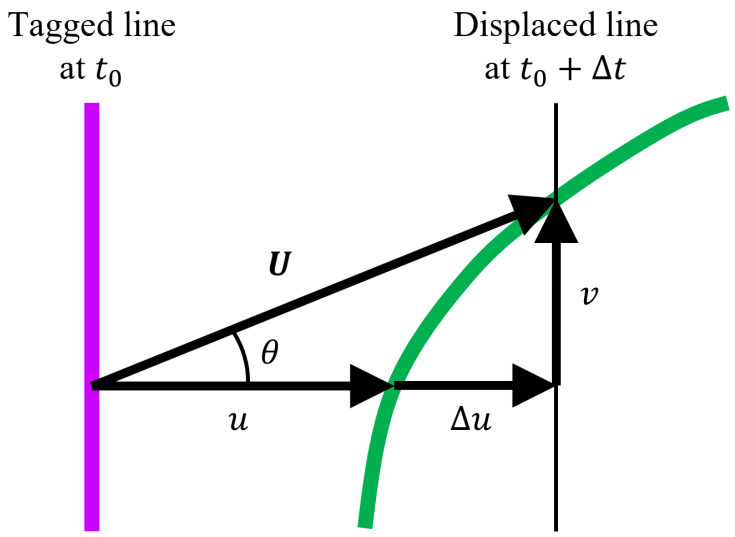

Figure 2.19: A schematic representation of how error can be produced in 1c-MTV due to the velocity component parallel to the tagged line. The total velocity at t_0 is given by $\boldsymbol{U}$ and the estimated lateral velocity is u. Due to the velocity v parallel to the tagged line, which cannot be measured using this method, the error Δu is produced.

respectively, Δu is the error in the estimated velocity, Δt is the time delay between the interrogation images, and $\partial u/\partial y$ is the instantaneous streamwise velocity gradient. Figure 2.19 provides a schematic representation of how this error arises in 1c-MTV. A priori knowledge of the flow is clearly required to provide an estimate of the error. However, the error is observed to be identically zero in parts of the flow where $v = 0$ or $\partial u/\partial y = 0$. These scenarios are not present in realistic flows and though reducing Δt will reduce the error, a large enough Δt is required for the resulting displaced line to be measurable with sufficient accuracy. This error must ultimately be considered near the airfoil surface and along the boundary layer for the current study.

The estimated uncertainty in measured pixel displacement is estimated in-situ by creating a representative image pair with the same signal-to-noise ratio as the actual experiment and having a known zero displacement between the image sequences. To generate the images in this manner, the camera cannot be used in the mode which generates two consecutive images since the exposure cannot be changed between the images, nor can the time between frames be arbitrarily reduced since the signal level of the second image would increase. Therefore, two separate images sequences are used in which the first image sequence is acquired 1 μs after the laser pulse and t_e = 600 μs,

just as the actual experiment, while a second image sequence, also acquired 1 μs after the laser pulse, is acquired with the laser energy and t_e decreased until the intensity of the tag lines match those of the actual experiment acquired at Δt = 6 ms and t_e = 600 μs. The two sequences, which are each comprised of 512 images, are processed as if they were image pairs in the experiments and the fluctuations from the known zero displacement are used to estimate the 95% confidence interval of the instantaneous pixel displacement $(\delta x)_{0.95}$. The resulting uncertainty is estimated to be $(\delta x)_{0.95} < 0.25$ pixel, which is conservative since the actual experiment uses 1024 image pairs and the image pairs for this calculation were not of the same flow, i.e., in separate sequences instead of true consecutive image pairs. At the water tunnel centerline, nominally $Re_c \approx 1.35 \times 10^4$ and there are $u_0 t/c \approx 145$ convective cycles for a typical image sequence with 1024 pairs for the stationary airfoil. Conservatively using the convective cycles as the number of samples N, the uncertainty in the mean velocity is $(\delta x)_{0.95}/\sqrt{N} < 0.23\%$ for a typical displacement of 9 pixel in the freestream. Following Benedict & Gould (1996) and assuming a Gaussian distribution, the standard deviation in the root-mean-square (RMS) pixel displacement is given by $1/\sqrt{2N} < 5.9\%$.

For plunging airfoil flow measurements, one image pair is acquired along each stroke at the same cross-stream position as its stationary airfoil counterpart. Due to the time constraints of performing flow measurements on the plunging airfoil at multiple cross-stream positions, the flow over the plunging airfoil is measured only at the centerline. The α is chosen such that the α_{eff} based on the motion matches that of the corresponding stationary airfoil measurement. The plunging procedure for the flow measurements does not have the same time limitation as that caused by the sensor bias for load measurements, and so successive strokes are repeated without the need to shut down and restart the water tunnel. In fact, the tunnel is left running so that there is no ambiguity in the repeatability of the freestream flow. Further time savings is obtained since the airfoil only needs to move through the image acquisition plane, making the full plunging profile unnecessary. In that case, the airfoil stops shortly after the requisite image pair is acquired and before the airfoil decelerates. However, to preserve the flow history of each measurement, the beginning of the motion is always the same and does not begin until the prescribed time required

to reach steady state. The total time saved by taking the above steps allows for faster 1c-MTV sample acquisition. Ultimately 50-100 strokes are completed per α_{eff} for 1c-MTV measurements to complete all measurements in a reasonable time frame, as compared to the 25 strokes for the load measurements. The image pairs are processed the same as the stationary airfoil measurements; however, the resulting velocity measurements of each individual stroke are phase averaged rather than time averaged like the stationary airfoil measurements.

The uncertainty in the mean velocity for the plunging airfoil measurements is estimated by considering each image pair acquired for the plunging airfoil as an independent sample. For the minimum $N = 50$ samples, the uncertainty in the mean velocity for the plunging airfoil is $(\delta x)_{0.95}/\sqrt{N} < 0.4\%$ based on the typical displacement of 9 pixel in the freestream and the standard deviation in the RMS velocity for the plunging airfoil is $1/\sqrt{2N} < 10\%$ (Benedict & Gould, 1996).

The resulting streamwise velocity measurement for the plunging airfoil is in the laboratory reference frame. To compare it to its stationary airfoil counterpart, the measurement is transformed to the airfoil reference frame to obtain the component aligned with the direction of u_{eff}. This is accomplished using the axis-rotation transformation of the velocity vector components from the laboratory coordinate system (X, Y) to the moving airfoil (x', y') coordinate system (with x' aligned with u_{eff}). Specifically, the streamwise velocity component for the plunging airfoil in the airfoil frame u' should be calculated using Eq. 2.6.

$$u' = u\cos(\alpha_i) + (v + V_a)\sin(\alpha_i) \tag{2.6}$$

However, since the vertical velocity component v is not measurable using this implementation of 1c-MTV, it is neglected in the transformation such that Eq. 2.6 is reduced to Eq. 2.7.

$$u' \cong u\cos(\alpha_i) + V_a\sin(\alpha_i) \tag{2.7}$$

Neglecting the contribution of v relative to u in calculating u' leads to an error of the order calculated by Eq. 2.8.

$$\frac{v\sin(\alpha_i)}{u\cos(\alpha_i)} = \frac{v}{u}\tan(\alpha_i) = \frac{v}{u}V_r \tag{2.8}$$

The freestream velocity component is generally the dominant component except near the leading edge, and possibly near the separation and reattachment locations. Thus, the ratio v/u is expected to be small for most of the measurement domain. However, if this ratio is assumed to be unity to provide a conservative error estimate, the inaccuracy in the transformation is then on the order of the velocity ratio V_r. This does not affect the accuracy of the separation and reattachment location measurements, which are based on the measured direction change of the streamwise flow, not the magnitude.

2.5.4 Boundary Layer Characterization

In this study, one way to establish the effects of shear and airfoil motion on the airfoil's boundary layer is by characterizing the flow separation and reattachment locations. Olson et al. (2013) discuss the challenges associated with determining separation and reattachment positions, x_s and x_r, respectively, including effects of Reynolds number, freestream turbulence intensity, and near-wall spatial resolution of the velocity profile. With respect to the Reynolds number effects, Re_c is carefully controlled here by calibrating the freestream speed and recording the water temperature. Concerning FSTI, the FSTI levels along the shear profile vary between 1.5-3% in the range of the airfoil positions investigated, as 2.4b shows, but are the same between the stationary and moving airfoil cases at a given position. The most prevalent challenge here is the near-wall spatial resolution which is affected by using a reference image shortly after the laser pulse in the current 1c-MTV implementation which creates a glare on the airfoil surface when the laser lines strike it. Due to this surface glare, approximately 8 pixels (0.62 mm) above the airfoil surface are not usable in the current study, which becomes particularly important at low α and thin separation regions.

Separation and reattachment points are estimated following similar methods of Olson et al. (2013) in which x_s and x_r are estimated based on the mean velocity direction reversal at the first velocity measurement above the surface. Whereas Olson et al. (2013) uses the midpoint between

the lines that measured the velocity reversal, the current study interpolates between the lines to estimate where the velocity crosses zero. In principle, the interpolation enhances the accuracy of the calculation since it is based on the local velocity measurements instead of only splitting the difference in location of the tagged lines. For example, if the velocity measurement at one tag line is much closer to zero than that of the other, the interpolation will reflect that the zero crossing is likely closer to the tag line with the velocity closer to zero, whereas the midpoint method would be further away. The streamwise uncertainty of the measurement is expected to be less than one-half the distance between lines, or approximately $\pm 0.011c$, since it is equal to the midpoint method in the limit of the interpolated location being exactly at the midpoint. Figure 2.20 shows an example of this method, in which x_s and x_r are shown in the red and blue triangles, respectively.

The boundary layer is also characterized by determining the variation of the boundary layer thickness (δ) along the chord, which is defined as the height above the airfoil surface such that $u = 0.99u_e$, where u_e is the velocity at the edge of the boundary layer and equal to u_∞. In uniform-shear flow, u_∞ is linearly varying, which makes it difficult to determine u_e in the freestream based on the mean velocity profile measured along the tag line. However, since the velocity profile outside the boundary layer is linear, this problem is tackled by calculating $\partial u/\partial y$ in the freestream along the tag line and finding the height above the airfoil surface where $\partial u/\partial y$ reaches the freestream value. The calculation of $\partial u/\partial y$ along the tag line involves first smoothing the mean velocity profile using a simple moving average at each pixel to reduce the noise in the derivative. The moving average uses the points along the line approximately $\pm 0.005c$ (± 8 pixel) on either side of each pixel. A second-order accurate, first-order derivative is then performed on the smoothed line profile. The freestream $\partial u/\partial y$ is determined by the average of $\partial u/\partial y$ from the top of the line profile extending $0.25c$ toward the airfoil surface, well outside the boundary layer. Starting from the maximum $\partial u/\partial y$ measurement, the line profile is followed until it crosses the freestream $\partial u/\partial y$ value, i.e., where δ is defined. The result of the smoothing can be seen in Figure 2.21, which shows the mean velocity and normalized $\partial u/\partial y$ profiles. Figure 2.21 also shows examples of the calculated $(\partial u/\partial y)_{max}$ and δ.

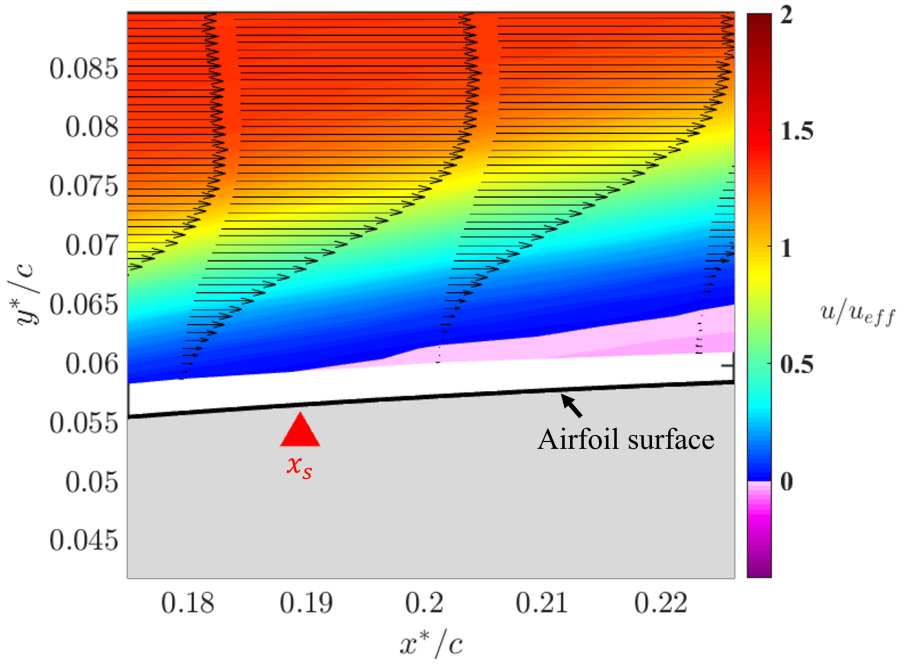

(a)

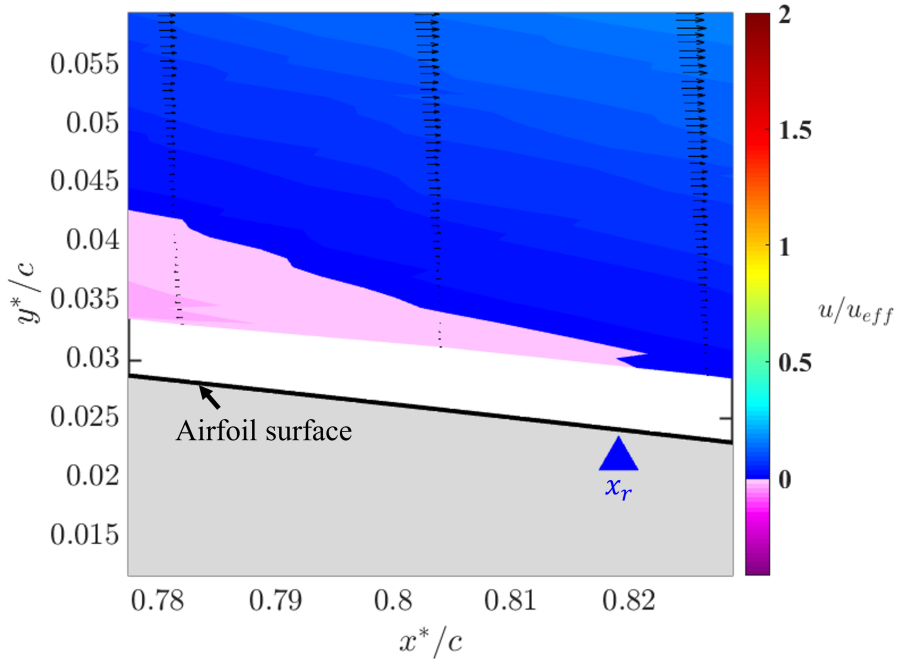

(b)

Figure 2.20: Mean velocity profiles overlaid on a contour map in denoting **(a)** separation and **(b)** reattachment positions for the stationary airfoil in shear at 7.6°. The freestream flow direction is left to right. Reversed flow is shown in the contour maps by the shades of pink/purple.

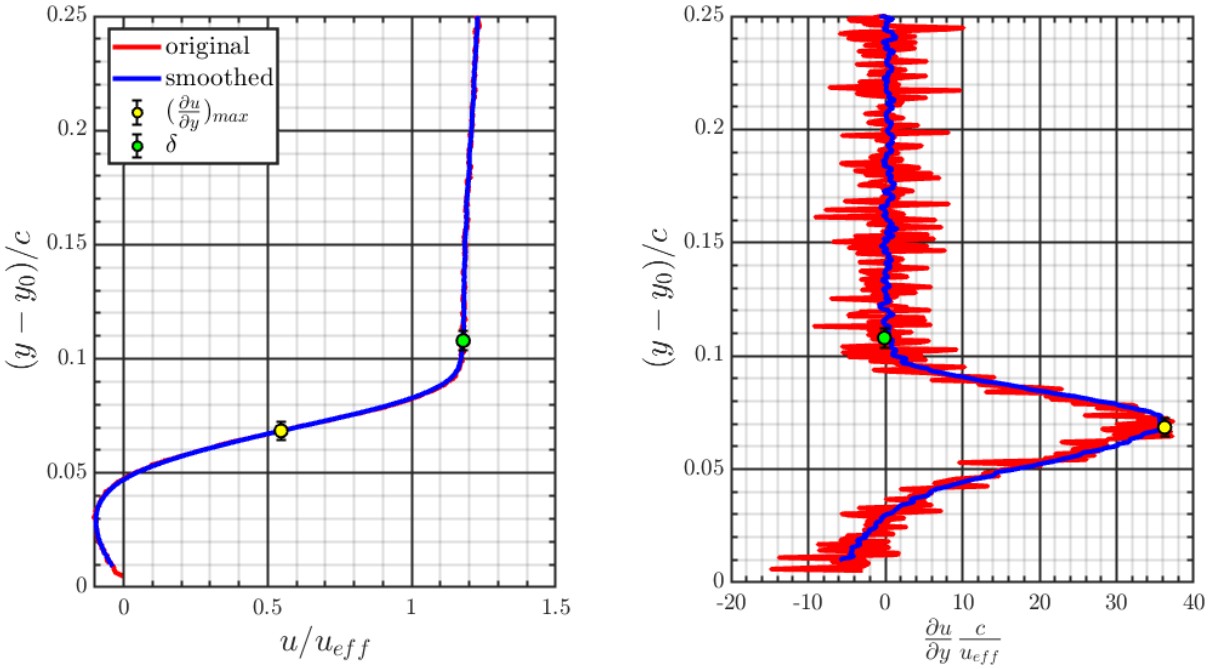

(a) (b)

Figure 2.21: **(a)** Mean velocity and **(b)** normalized $\partial u/\partial y$ for the stationary airfoil in shear at 5.6°, with calculated points for $(\partial u/\partial y)_{max}$ and δ. Though hard to see, the original and smoothed mean velocity profiles are on top of each other, and the freestream normalized $\partial u/\partial y$ approaches 0.5, which is the expected value based on the dimensionless shear rate K.

CHAPTER 3

UNIFORM FLOW RESULTS AND SETUP VALIDATION

Measurements are first performed in uniform flow to validate various aspects of the experimental setup and to provide references for the shear measurements. In traditional force balance measurements, the test model is kept on the centerline of the test section while stationary or oscillating over an amplitude that is negligible relative to the test section's width. Therefore, an important aspect of this study is to validate the present experimental approach, ensuring the large motion of the airfoil relative to the test section width does not cause significant artifacts due to blockage or confinement effects. Validating the experimental approach in this manner also demonstrates its viability for obtaining load measurements on the airfoil traversing across the measurement domain in shear flow. In uniform flow, the aerodynamic load on the airfoil steadily moving perpendicular to the freestream may be predicted by equating its effective angle of attack α_{eff} with the geometric angle of attack α of the stationary airfoil under the same flow conditions. Therefore, another important aspect of this study is to ensure that the current setup reproduces the theoretical relation between the steadily plunging airfoil and stationary airfoil in uniform flow. Since $\alpha = \alpha_{eff}$ for the stationary airfoil, the notation of α_{eff} is used for stationary airfoil angles of attack to simplify comparison with the moving airfoil results. As noted in Chapter 2, typically $V_r^2 \ll 1$ for the plunging airfoil, which means $u_{eff} \cong u_0$. For simplicity, the Re_c values reported are based on the local freestream velocity u_0; however, note the u_{eff} is used to precisely calculate the load coefficients in the airfoil frame of reference. The sensitivity in Re_c noted in Chapter 2 is not considered regarding the relation between the stationary and moving airfoils since the variation is expected to be small, scaling with $\sqrt{1 + {V_r}^2}$.

3.1 Load on the Stationary Airfoil at Multiple Cross-stream Locations

The validations are first approached in the current study by measuring the time averaged C_L and C_D on the stationary airfoil at the three primary cross-stream positions of interest, $Y/c = 0$

and ±0.5 at the same Reynolds number of $Re_c = 1.28 \times 10^4$. Comparing the stationary airfoil load measurements at these positions characterizes the basic effects of the airfoil being confined by the test section boundaries. The resulting C_L- and C_D-α_{eff} curves for the stationary airfoil in uniform flow at the three Y/c positions are shown in Fig. 3.1, in which the $\alpha_{eff} = 0$ is referenced by the zero lift α_{eff} at $Y/c = 0$. The results in Fig. 3.1 show that over the angle of attack range -15° < α_{eff} < 15° the load is impacted very little by the presence of the tunnel boundaries. The results at each Y/c in Fig. 3.1 at zero α_{eff} show the C_L, C_D and $\alpha_{L=0}$ vary less than the respective uncertainty in each value; C_L or C_D less than ±0.008 and zero lift α_{eff} < ±0.1°. At high α_{eff}, the variation in C_L and C_D is also within typical measurement uncertainty. Further discussion of the relationship between cross-stream position, zero-lift angle of attack, and load near zero α is provided in Appendix C.

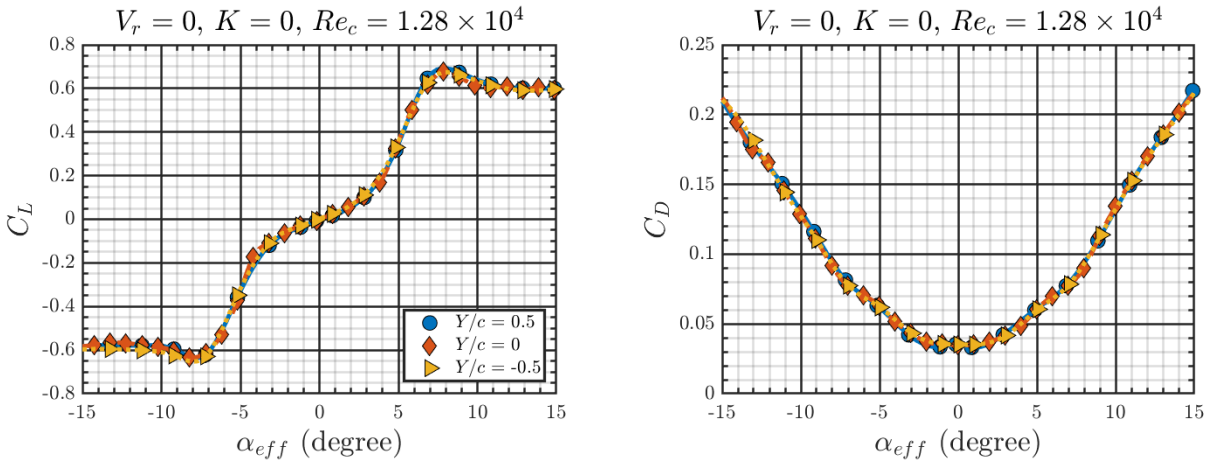

(a) (b)

Figure 3.1: **(a)** C_L- and **(b)** C_D-α_{eff} curves for the stationary airfoil in uniform flow at $Re_c = 1.28 \times 10^4$ at the three cross-stream positions: $Y/c = 0$ and ±0.5. Spline interpolants are used to connect points for clarity due to overlapping data.

3.2 Relating the Loads on the Stationary and Plunging Airfoils

The next step in the validations involves measuring the phase averaged load on the plunging airfoil in uniform flow and comparing it to the time averaged load on the stationary airfoil under the same flow conditions. In the comparison, the α_{eff} for the moving airfoil is equated to the α of

the stationary airfoil at the time instant when the former is at the same cross-stream location as the latter. That is, the load on the plunging airfoil with a prescribed α_{eff} during each stroke is phase averaged and extracted at the prescribed positions where the stationary airfoil measurements were made at the equivalent α. The comparison is made using plunge velocity ratios in the range V_r = 0.05-0.15 at three primary cross-stream locations, Y/c = 0 and ±0.5, which are encompassed by the plunging airfoil stroke range used for the shear flow experiments.

The mean C_L- and C_D-α_{eff} characteristics of the plunging airfoil at V_r = 0.05-0.15 in uniform flow at each of the three primary Y/c locations are shown in Figures 3.2-3.4, respectively, with the same measurements for the stationary airfoil (V_r = 0) for reference. At each Y/c in Figs. 3.2-3.4, close agreement is observed in the C_L-α_{eff} curves for $|\alpha_{eff}| \lesssim 6^\circ$ between the plunging airfoils at each V_r and the stationary airfoil, noting the relatively coarse angle of attack resolution for the plunging airfoil compared to the stationary airfoil. At $|\alpha_{eff}| \approxeq 8^\circ$, the C_L on the plunging airfoil at each V_r tends to be 7-14% higher than for the stationary airfoil. However, it is noted that load measurements on the plunging airfoil are difficult to make at this α_{eff} since it is the approximate α_{eff} of the peak C_L and stall based on the stationary airfoil C_L-α_{eff} curve, which corresponds to higher unsteadiness in the flow. The C_D results in Figs. 3.2-3.4 show agreement with the stationary airfoil for only the V_r = 0.05 and 0.1 plunging airfoil cases, typically to within the measurement uncertainty. The subtle differences in the loads between the V_r = 0-0.1 cases are more apparent in the C_D results than for the C_L results based on the different scales of their respective ordinate axes. By contrast, the C_D results for the V_r = 0.12 and 0.15 plunging airfoil cases show consistently lower C_D than for the V_r = 0-0.1 cases.

At V_r = 0.12 and 0.15, the C_D results at each Y/c do not even agree among themselves for the plunging airfoil, and at Y/c = -0.5 the $C_D < 0$ (i.e., thrust) near zero angle of attack. Though the C_L time history does not show large transients persisting far into the airfoil motion trajectory (see Chapter 2), analysis of the C_D time history for the V_r = 0.12 and 0.15 cases show transients persisting from the start of motion and far into the airfoil motion trajectory. This result indicates that measuring the loads on the plunging airfoil at these V_r for the purpose of connecting to the

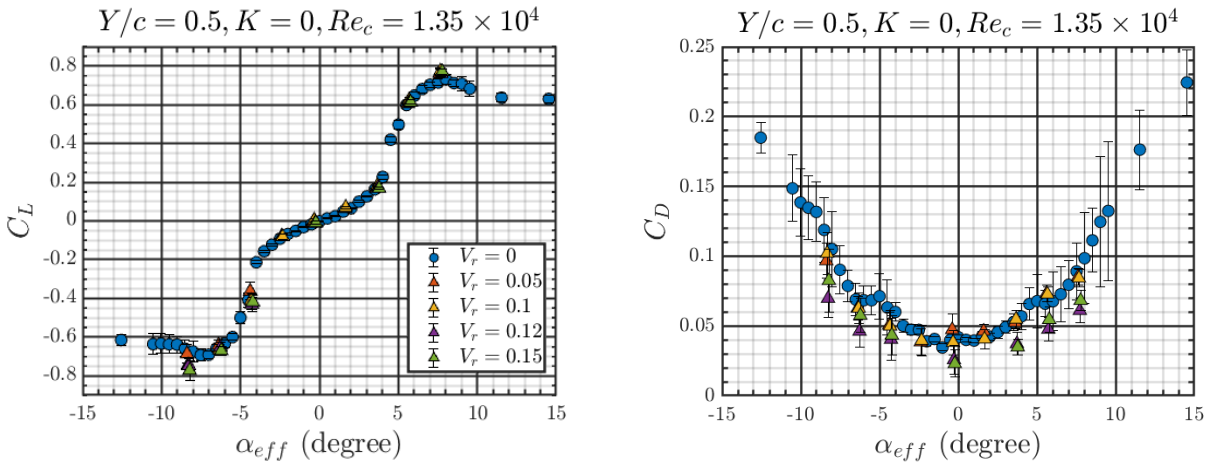

(a) (b)

Figure 3.2: **(a)** C_L- and **(b)** C_D-α_{eff} curves for the stationary and plunging airfoils at $Y/c = 0.5$, $Re_c = 1.35 \times 10^4$ in uniform flow ($K = 0$).

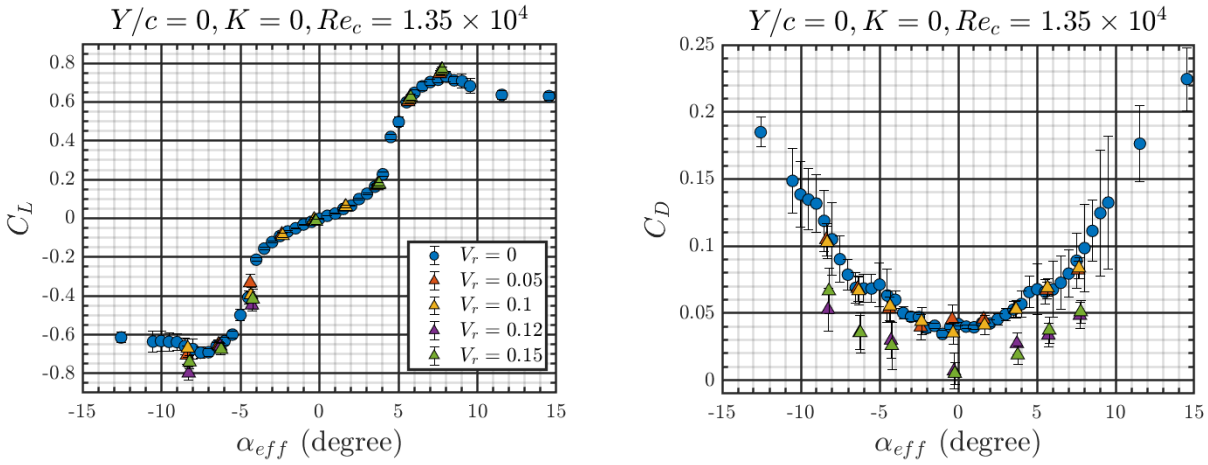

(a) (b)

Figure 3.3: **(a)** C_L- and **(b)** C_D-α_{eff} curves for the stationary and plunging airfoils at $Y/c = 0$, $Re_c = 1.35 \times 10^4$ in uniform flow ($K = 0$).

stationary airfoil loads cannot be performed in shear flow with the current experimental setup. As such, the nominal plunge speed of $V_a = 1$ cm/s ($V_r = 0.1$ at the centerline) is the limit of the current study such that lower V_r are realized in the high-speed uniform stream of the shear flow profile, as demonstrated in Fig. 2.11a, where transient loads on the airfoil are ensured not to persist into the shear zone.

In summary, the agreement in the mean C_L and C_D results between the stationary and moving

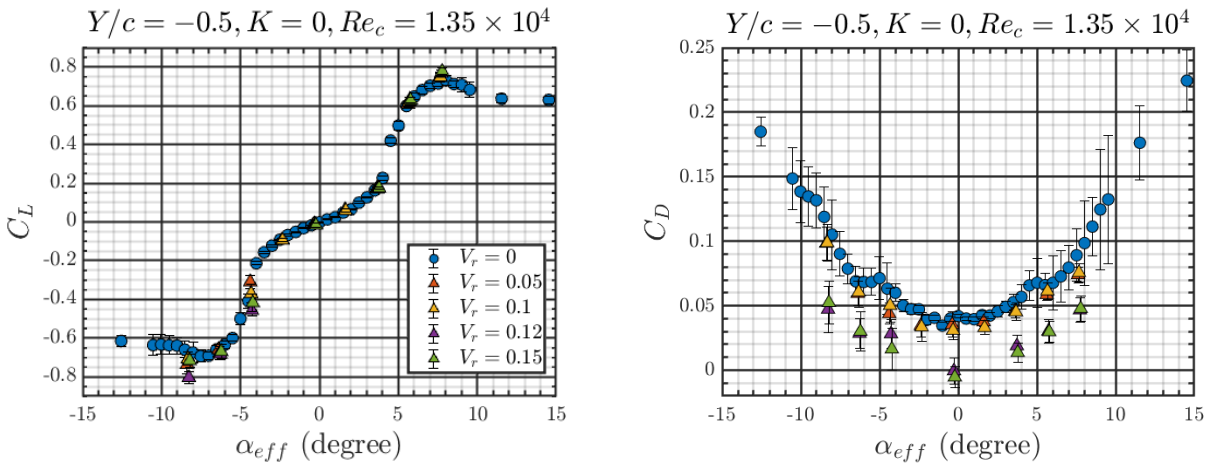

(a) (b)

Figure 3.4: **(a)** C_L- and **(b)** C_D-α_{eff} curves for the stationary and plunging airfoils at Y/c = -0.5, $Re_c = 1.35 \times 10^4$ in uniform flow ($K = 0$).

airfoil cases in uniform flow indicates there are no significant blockage, confinement, or other artifacts up to $V_r = 0.1$. These measurements also validate the viability of the experimental approach for obtaining load measurements on the airfoil traversing across the measurement domain in shear flow, with limits on the plunge speed prescribed in the high-speed uniform stream. Furthermore, the current setup reproduces the Galilean transformation between the steadily plunging airfoil and stationary airfoil in uniform flow.

3.3 Flow Measurement Validation and Baseline Cases

Flow measurements are obtained in uniform flow for the stationary and plunging airfoils to validate the 1c-MTV setup for the plunging airfoil and provide baseline cases for the flow measurements in shear. The streamwise velocity component of the flow around the plunging airfoil in uniform flow is measured at the water tunnel centerline and compared to that of the stationary airfoil by relating their α_{eff} under the same flow conditions. An example of these flow results is provided in Figs. 3.5 and 3.6 which contain the mean and RMS streamwise velocity results, respectively, for the airfoil in uniform flow with $V_r = 0$ (stationary), 0.05 and 0.1 at $\alpha_{eff} = 3.6°$. The flow results are plotted relative to the chordwise and chord-normal coordinates (x^*, y^*) referenced at the leading edge after applying the axis rotation to match the stationary and plunging airfoil reference frames

as described in Chapter 2 using Eq. 2.7. For simplicity, the streamwise velocity measurements for either the stationary or plunging airfoil are given in the reference frame of the airfoil and denoted by u', noting that $u \equiv u'$ for the stationary airfoil. The results in Figs. 3.5 and 3.6 show good agreement in the overall flow behavior between the stationary and plunging airfoil cases. This agreement is expected based on the agreement between the C_L and C_D results at $\alpha_{eff} = 3.6°$ from Figs. 3.2-3.4, which are shown in the subfigures of Figs. 3.5 and 3.6 for reference.

The streamwise velocity results are more closely examined by considering the boundary layer separation and reattachment locations, x_s and x_r, respectively, which are determined by the locations along the airfoil surface where the flow changes direction as described in Chapter 2. The x_s and x_r given by chordwise position x^*/c for the stationary and plunging airfoils in uniform flow at the centerline are shown in Fig. 3.7 for several α_{eff}. The mean and RMS streamwise velocity results for each α_{eff} for the stationary and plunging airfoils in uniform flow are provided in Appendix E. In Fig. 3.7, good agreement in x_s is observed between the stationary and plunging airfoils at each α_{eff} investigated, with the difference in x_s between the cases at a given α_{eff} of less than $0.05c$. Open separation is denoted in Fig. 3.7 by $x^*/c = 1$ in the results for x_r and is observed for each case up to $\alpha_{eff} = 3.6°$. For $\alpha_{eff} > 3.6°$, reattachment is observed ($x^*/c < 1$ for x_r results) for the stationary and both plunging airfoil cases; however, the reattachment point is approximately 0.06-0.09c farther upstream for $V_r = 0.05$ and 0.1 compared to the stationary airfoil. Recalling that the estimated uncertainty in x_s and x_r is approximately $\pm 0.011c$, it is difficult to discern whether the observed variation in x_s and x_r can be attributed to real flow phenomena or the limited number of samples for the plunging airfoil cases.

The boundary layer thickness δ/c as a function of chordwise position x^*/c is also considered and determined as outlined in Chapter 2. The growth of δ/c along the airfoil surface for the stationary and both plunging airfoil cases is shown for example in Fig. 3.8 for $\alpha_{eff} = 3.6°$ and demonstrates excellent agreement up to the separation point near $x^*/c \approx 0.5$. Good agreement in the growth rate of δ/c is still observed for $x^*/c > 0.5$, though there is more variation between the cases which, like the x_s and x_r variation, could be attributed to the limited number of samples for

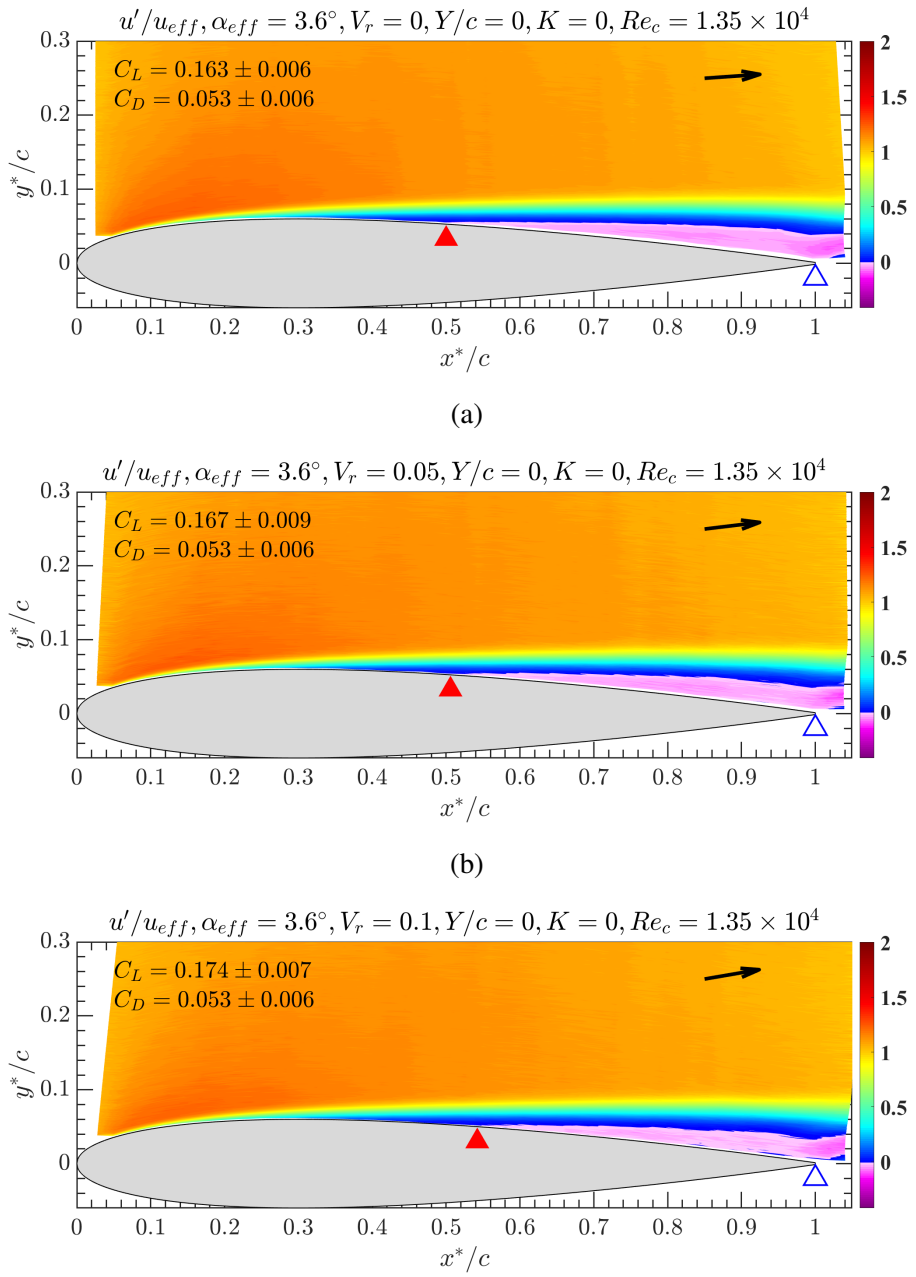

Figure 3.5: Mean streamwise velocity measurements by 1c-MTV for **(a)** the stationary airfoil ($V_r = 0$), and the plunging airfoil with **(b)** $V_r = 0.05$ and **(c)** $V_r = 0.1$ at $\alpha_{eff} = 3.6°$; uniform flow, $Y/c = 0$, $Re_c = 1.35 \times 10^4$. The black arrow in the upper right corner of each subfigure indicates the direction of the approach stream in the laboratory reference frame. The boundary layer separation location is denoted by the red triangle and the open separation at the trailing edge is denoted by the open blue triangle. Reversed flow is indicated by the shades of pink/purple.

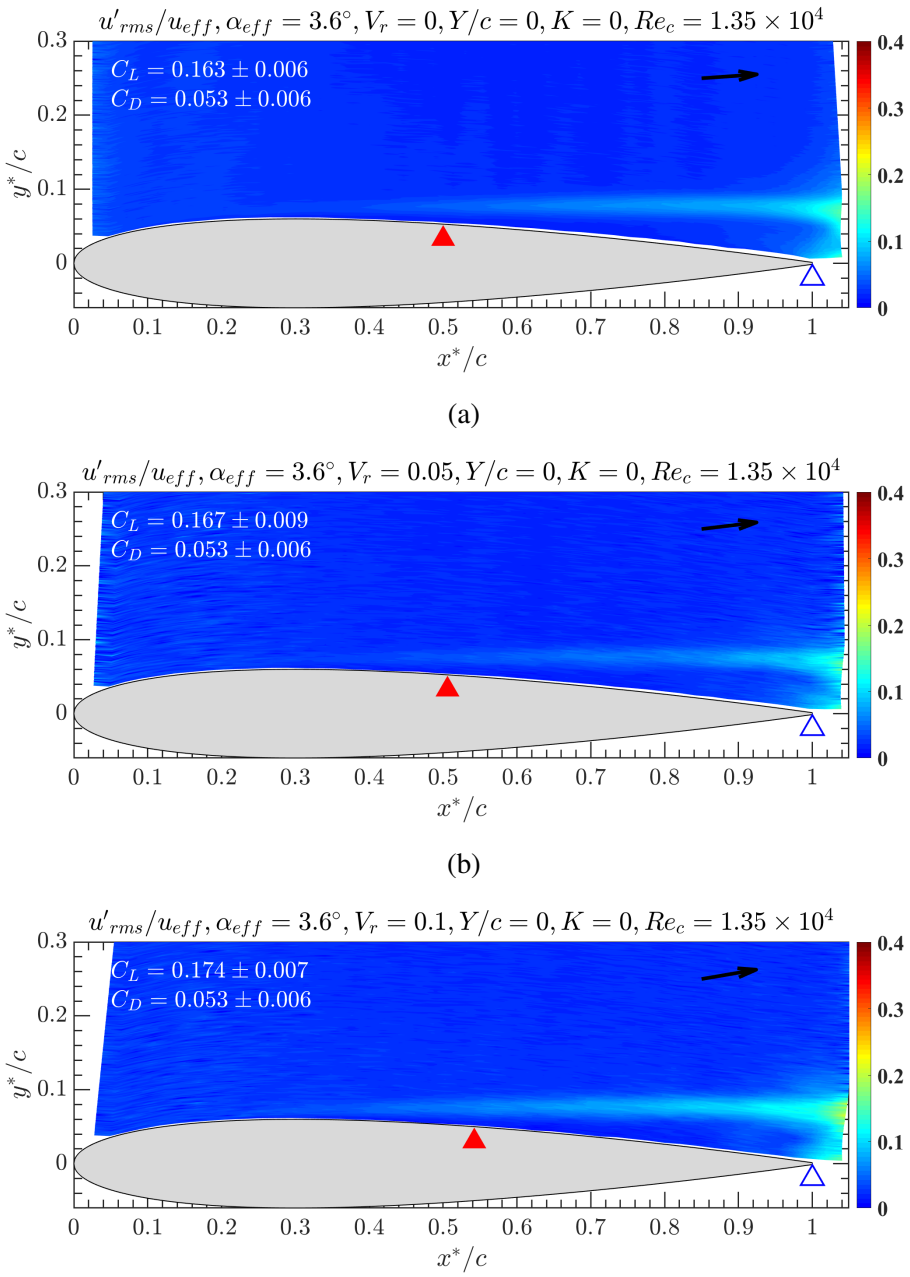

Figure 3.6: RMS streamwise velocity measurements by 1c-MTV for **(a)** the stationary airfoil ($V_r = 0$), and the plunging airfoil with **(b)** $V_r = 0.05$ and **(c)** $V_r = 0.1$ at $\alpha_{eff} = 3.6°$; uniform flow, $Y/c = 0$, $Re_c = 1.35 \times 10^4$. The black arrow in the upper right corner of each subfigure indicates the direction of the approach stream in the laboratory reference frame. The boundary layer separation location is denoted by the red triangle and the open separation at the trailing edge is denoted by the open blue triangle.

the plunging airfoil cases, especially in the more unsteady regions of the flow.

The 1c-MTV results in uniform flow demonstrate the ability of the current 1c-MTV implementation to measure the streamwise velocity component of the flow for both the stationary and plunging airfoil. Performing the axis rotation on the flow measurements to match the α_{eff} of the stationary and plunging airfoils proves to be accurate for the current setup. The flow, including boundary layer thickness, and separation and reattachment locations, agrees well overall between the stationary and plunging airfoil, which is expected since the aerodynamic loads also show good agreement. Furthermore, the 1c-MTV results for uniform flow demonstrate the ability of the setup to perform the same measurements in shear flow.

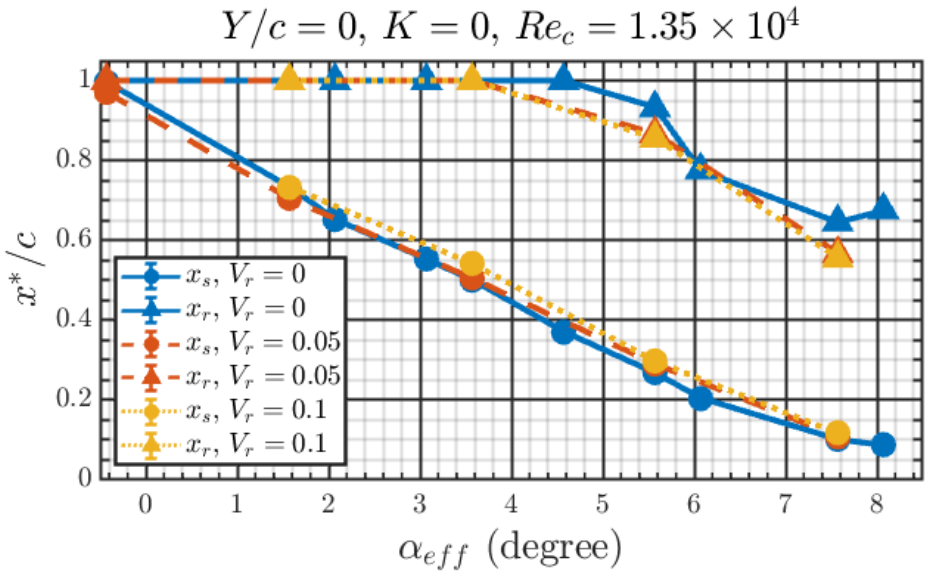

Figure 3.7: The separation and reattachment locations, x_s and x_r, respectively, given by chordwise position x^*/c for the stationary ($V_r = 0$) and plunging ($V_r \neq 0$) airfoils in uniform flow ($K = 0$) at the centerline ($Y/c = 0$) where $Re_c = 1.35 \times 10^4$. Circle symbols indicate x_s while triangle symbols indicate x_r. Open separation is indicated by $x^*/c = 1$ in the results for x_r.

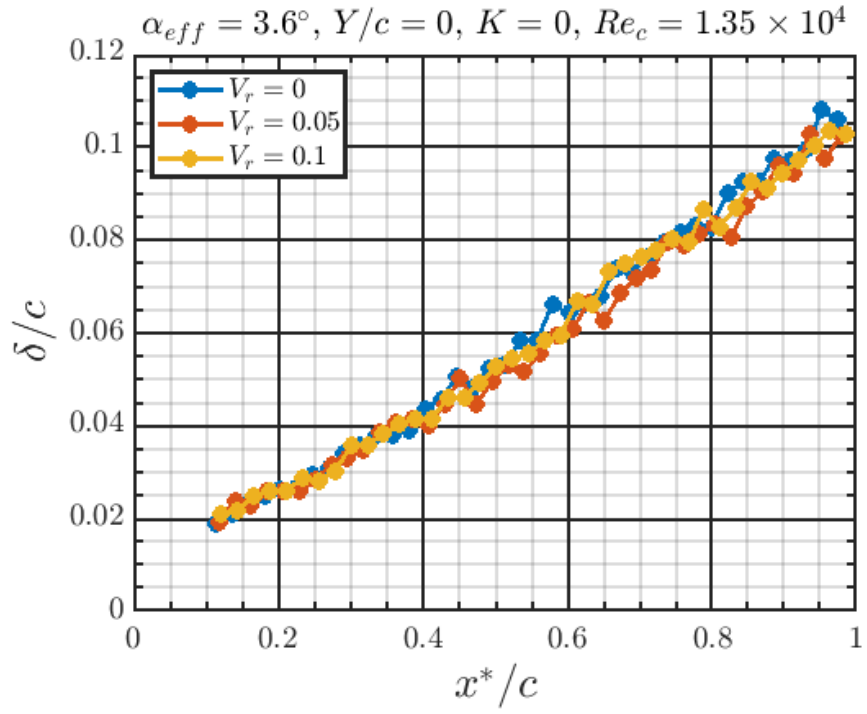

Figure 3.8: Boundary layer thickness δ/c as a function of chordwise position x^*/c for the stationary ($V_r = 0$) and plunging ($V_r \neq 0$) airfoils at $\alpha_{eff} = 3.6°$ in uniform flow ($K = 0$) at the centerline ($Y/c = 0$) where $Re_c = 1.35 \times 10^4$.

3.4 Reynolds Number Effect Based on Cross-stream Position

By nature of the varying velocity profile of the shear flow considered in the current study, the local freestream parameters are different at the three cross-stream locations of primary interest, $Y/c = 0$ and ± 0.5. Therefore, it is important to first establish the basic effects on the airfoil in uniform flow at the same Reynolds numbers that are defined in shear flow at the three respective locations: $Re_c = 1.65 \times 10^4$ at $Y/c = 0.5$, $Re_c = 1.35 \times 10^4$ at $Y/c = 0$ and $Re_c = 0.98 \times 10^4$ at $Y/c = -0.5$. Establishing a baseline of the expected aerodynamic loads and flow field for the NACA 0012 airfoil is non-trivial, as compiled by McCroskey (1987) for $Re_c > 10^5$ and discussed by Tank et al. (2017) focused near $Re_c = 5 \times 10^4$. Resolving the relevant flow phenomena, such as separation and reattachment locations, at low Re_c is especially difficult as they are highly impacted by the facility freestream turbulence intensity (FSTI) and the thinness of the separation zone, as discussed in Olson et al. (2013). To address these concerns and establish self-consistent baseline

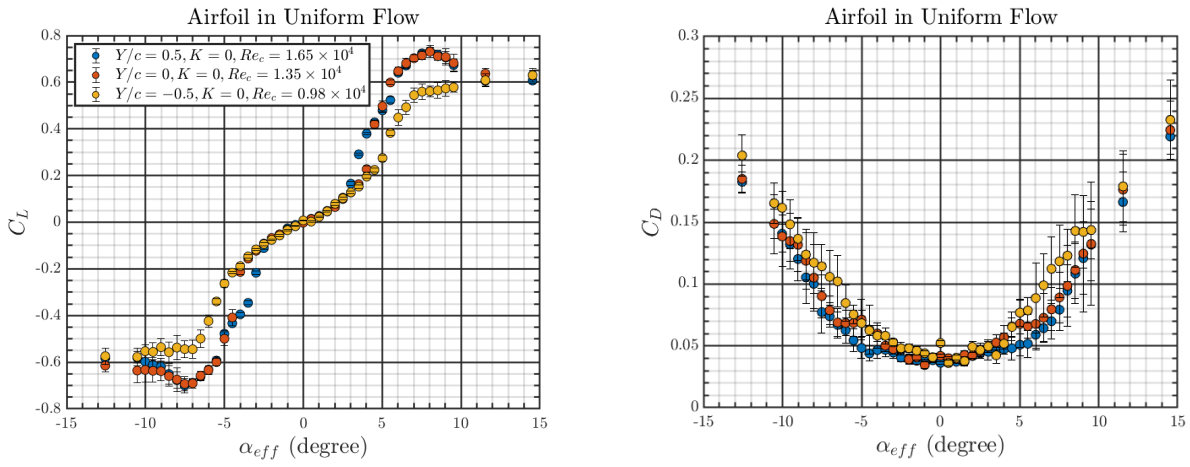

(a) (b)

Figure 3.9: **(a)** C_L- and **(b)** C_D-α_{eff} curves for the stationary airfoil in uniform flow at each of the three cross-stream positions used for measurements. The Reynolds numbers are set based on the Y/c and Re_c pairs in Table 2.1; $Re_c = 1.65 \times 10^4$ at $Y/c = 0.5$, $Re_c = 1.35 \times 10^4$ at $Y/c = 0$ and $Re_c = 0.98 \times 10^4$ at $Y/c = -0.5$.

results for the current setup, load and flow measurements on the stationary airfoil in uniform flow are performed at each of the three positions where the freestream speed is accordingly adjusted to match the Re_c at each position from Table 2.1. The C_L- and C_D-α_{eff} curves for the stationary airfoil in uniform flow, given in Fig. 3.9, shows the general effect of Reynolds number over the current experimental parameter space. There is clear variation observed between the cases which comprise the rather small Reynolds number range $Re_c = 0.98 \times 10^4$-1.65×10^4. It is observed in Fig. 3.9a for both $Re_c = 1.35 \times 10^4$ and $Re_c = 1.65 \times 10^4$ that the peak mean $|C_L| \approxeq 0.7$ and occurs at $|\alpha_{eff}| \approxeq 8°$, and typical leading edge stall behavior is observed in the C_L-α_{eff} curve. By contrast, at $Re_c = 0.98 \times 10^4$ the mean $|C_L| \approxeq 0.55$ (21% lower) at $|\alpha_{eff}| \approxeq 8°$ and the C_L-α_{eff} curve overall exhibits behavior typically associated with trailing edge stall. In Fig. 3.9b, a complementary observation is made as the C_D at $|\alpha_{eff}| \approxeq 8°$ is approximately the same for both $Re_c = 1.35 \times 10^4$ and $Re_c = 1.65 \times 10^4$ ($C_D \approxeq 0.10$), whereas at $Re_c = 0.98 \times 10^4$ the C_D is around 30% higher ($C_D \approxeq 0.13$).

Perhaps the most interesting observation in the load results is the variation in the C_L- and C_D-α_{eff} curves between $0° \lessapprox |\alpha_{eff}| \lessapprox 8°$. To highlight this angle of attack range, the load results from Fig. 3.9 are reproduced in Fig. 3.10 with a zoomed-in α_{eff} range focused on positive

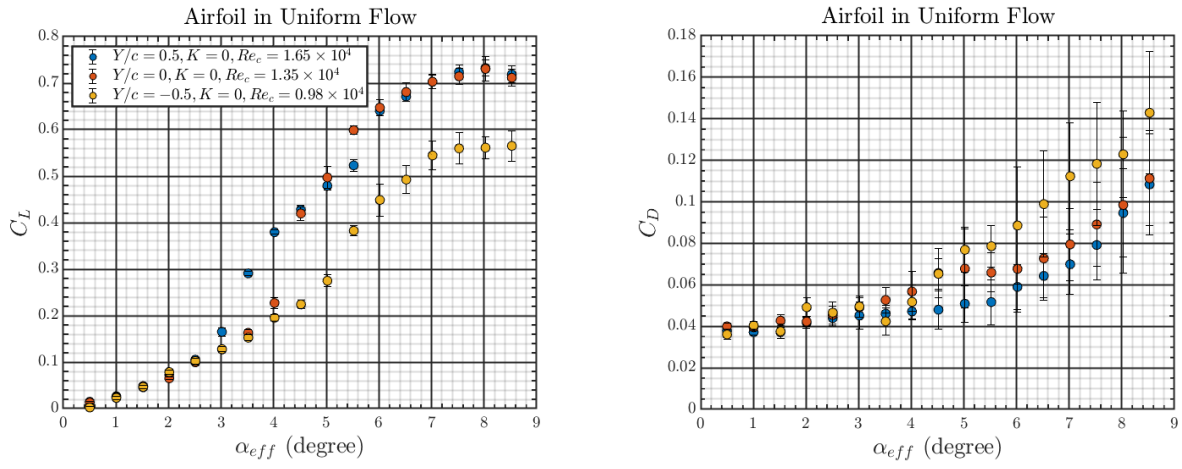

(a) (b)

Figure 3.10: **(a)** C_L- and **(b)** C_D-α_{eff} curves for the stationary airfoil in uniform flow at each of the three cross-stream positions used for measurements. The Reynolds numbers are set based on the Y/c and Re_c pairs in Table 2.1; $Re_c = 1.65 \times 10^4$ at $Y/c = 0.5$, $Re_c = 1.35 \times 10^4$ at $Y/c = 0$ and $Re_c = 0.98 \times 10^4$ at $Y/c = -0.5$.

angles since the C_L- and C_D-α_{eff} curves show good symmetry. It is observed in Fig. 3.10 that the C_L- and C_D-α_{eff} curves are in close agreement up to $\alpha_{eff} \approxeq 2.5°$ for each Re_c. However, beginning at $\alpha_{eff} \approxeq 2.5°$ the C_L on the airfoil for $Re_c = 1.65 \times 10^4$ increases at a faster rate, while its C_D remains comparatively lower, than for the other two Re_c cases. Meanwhile, the C_L at the two lower Re_c maintain close agreement up to $\alpha_{eff} \approxeq 3.5°$, but a trend in the C_D results is not conclusive. At $\alpha_{eff} \approxeq 3.5°$ the C_L on the airfoil at $Re_c = 1.35 \times 10^4$ begins to increase at a faster rate than for $Re_c = 0.98 \times 10^4$ and by $\alpha_{eff} \approxeq 5°$ surpasses the C_L for $Re_c = 1.65 \times 10^4$. Between $5° \lessapprox \alpha_{eff} \lessapprox 8°$ the C_D on the airfoil is highest on the airfoil at $Re_c = 0.98 \times 10^4$ and decreases with increasing Re_c over the current Re_c range. By contrast, in the same α_{eff} range, the C_L on the airfoil for $Re_c = 1.35 \times 10^4$ and $Re_c = 1.65 \times 10^4$ are in close agreement while it is considerably lower for $Re_c = 0.98 \times 10^4$.

The difficulty with establishing the expected aerodynamic loads at low Re_c is exemplified in Fig. 3.11 which shows the unsurprising disagreement in the C_L-α_{eff} results for the NACA 0012 airfoil from data found in literature and the current study at similar Re_c. Figure 3.11a compares the C_L-α_{eff} curves for $Re_c \leq 1.0 \times 10^4$ from the studies of Sunada et al. (1997), Cleaver et al. (2013), Ohtake et al. (2007) and the current study. There is considerable disagreement between all

cases in Fig. 3.11a, especially at higher α_{eff}, even though they have nearly the same Re_c. On the other hand, Fig. 3.11b compares the C_L-α_{eff} curves for $1.65 \times 10^4 \leq Re_c \leq 2.07 \times 10^4$ from the studies of Cleaver et al. (2010), Laitone (1997), Ohtake et al. (2007) and the current study. The results in Fig. 3.11b show that there is fair agreement up to about $\alpha_{eff} = 5^\circ$ among the cases excluding Ohtake et al. (2007); however, the stall behavior drastically varies despite the small variation in Re_c. Notwithstanding these differences, a common interesting feature in the C_L-α_{eff} results for the Re_c shown thus far is the presence of multiple regions prior to stall. For example, for $Re_c = 2.0 \times 10^4$ of Cleaver et al. (2010) in Fig. 3.11b, there is a low-slope region in the range $0^\circ \lesssim \alpha_{eff} \lesssim 2^\circ$, a high-slope region in the range $2^\circ \lesssim \alpha_{eff} \lesssim 4^\circ$, and a moderate-slope region in the range $4^\circ \lesssim \alpha_{eff} \lesssim 10^\circ$. Similar multi-region features are observed in the results for the current study, Ohtake et al. (2007) and Laitone (1997) in Fig. 3.11b.

For low Reynolds numbers such as those examined here, the separated boundary layer quickly transitions to turbulent flow, and can ultimately allow turbulent reattachment and the formation of a closed separation bubble. Based on surface pressure distribution data for $Re_c = 2.3 \times 10^4$-4.8×10^4, Kim et al. (2011) connected the change from a low-slope to high-slope region in their C_L-α curves to switch from an open separation to a closed separation bubble, demonstrating the complex and sensitive aerodynamic patterns within this Reynolds number range. Such a connection was further explored by Albrecht et al. (2022), who directly connected the behavior of the aerodynamic loads to the flow switching from an open separation to a closed separation bubble by characterizing the separation and reattachment locations using 1c-MTV. To characterize the flow phenomena associated with observations in the load results for the current study, flow measurements using 1c-MTV are made for a subset of α_{eff} at each of the three cross-stream positions under the same flow conditions as the load measurements, i.e., the same pairs of Y/c and Re_c values. The α_{eff} subset chosen for flow measurements is based on specific features observed in the load results, such as the α_{eff} after which there is a sharp change in the slope of the C_L-α curve. The α_{eff} selection is primarily motivated by the load results in shear, but flow measurements are made in uniform flow at the same α_{eff} for reference.

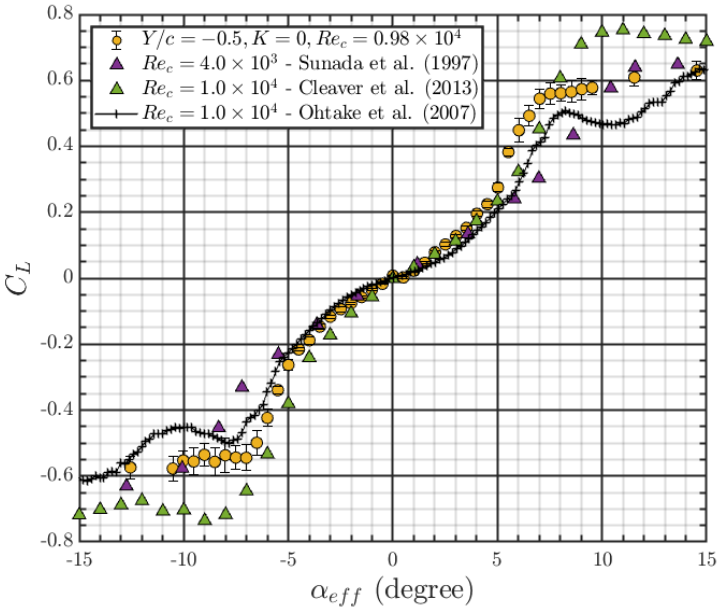

(a)

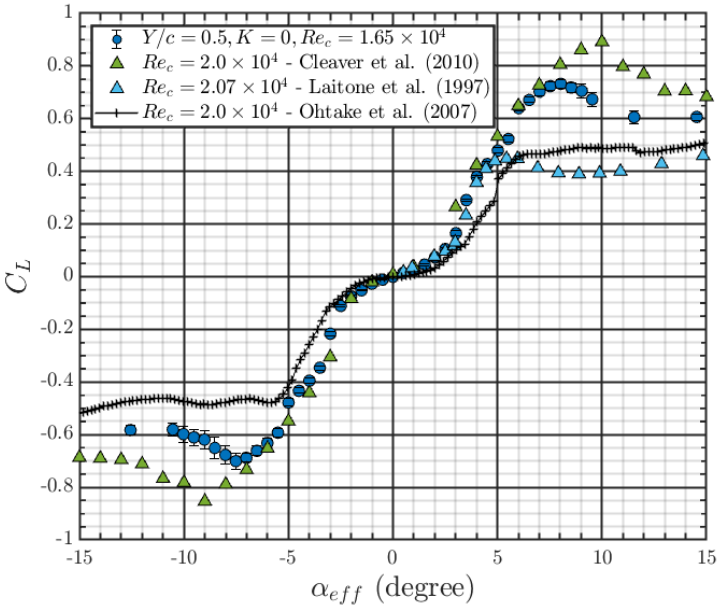

(b)

Figure 3.11: C_L-α_{eff} curves for the stationary NACA 0012 airfoil in uniform flow for the current study and data from literature in the Reynolds number ranges **(a)** $Re_c \leq 1.0 \times 10^4$ and **(b)** $1.65 \times 10^4 \leq Re_c \leq 2.07 \times 10^4$.

Figures 3.12 and 3.13 show the mean streamwise and RMS velocity results, respectively, for the stationary airfoil at $\alpha_{eff} = 6.1^{\circ}$ and each Y/c and Re_c pair, while the same results for the other angles are provided in Appendix E. It is clear from Fig. 3.12 and 3.13 that the variation C_L- and C_D-α_{eff} curves for the airfoil at each Y/c and Re_c pair are rooted in significantly different flow behavior. At $Re_c = 1.65 \times 10^4$ in Fig. 3.12a there is a closed separation bubble covering about 38% of the airfoil surface, and in Fig. 3.13a there is a region of high RMS close to the airfoil surface roughly at the reattachment point. By contrast, at $Re_c = 1.35 \times 10^4$ in Fig. 3.12b, a closed separation bubble is observed to cover 57% of the airfoil surface, with a region of high RMS observed in Fig. 3.13b centered farther away from airfoil surface and slightly upstream of the reattachment point. At $Re_c = 0.98 \times 10^4$ in Fig. 3.12c, open separation is observed with reversed flow covering 74% of the airfoil surface and in Fig. 3.13c the high RMS region appears to be formed at and past the trailing edge.

The variation in the flow behavior over the angle of attack range studied is demonstrated by the separation and reattachment locations at each Y/c and Re_c pair shown in Fig. 3.14. No single trend is observed in the separation behavior between the three Re_c cases. However, the reattachment behavior between the three Re_c cases clearly shows that as α_{eff} increases the reattachment location occurs further upstream at the highest Re_c compared to the other two Re_c, while no reattachment is observed on the airfoil at the lowest Re_c. Though the α_{eff} resolution in Fig. 3.14 coarse, it is also observed that the C_L and C_D behavior in Fig. 3.10 is connected to the separation and reattachment behavior, like the connection made by Kim et al. (2011) and (Albrecht et al., 2022). The start of the sudden rise in C_L observed at $\alpha_{eff} \approxeq 2.5^{\circ}$ for $Re_c = 1.65 \times 10^4$ and $\alpha_{eff} \approxeq 3.5^{\circ}$ for $Re_c = 1.35 \times 10^4$ is connected to the switch from an open separation to a closed separation bubble on the airfoil surface.

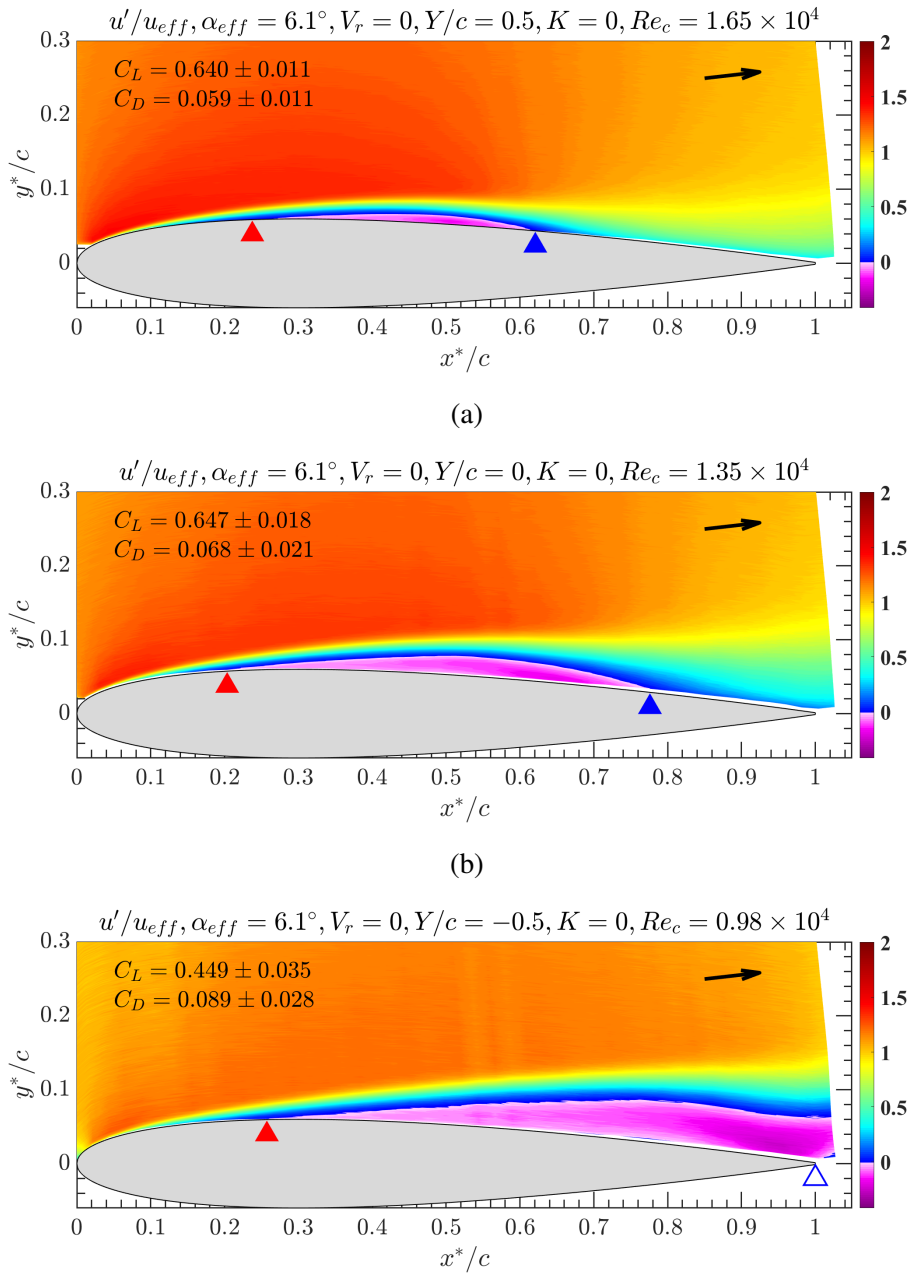

Figure 3.12: Mean streamwise velocity measurements by 1c-MTV for the stationary airfoil at $\alpha_{eff} = 6.1°$ in uniform flow ($K = 0$) for **(a)** $Y/c = 0.5$, $Re_c = 1.65 \times 10^4$, **(b)** $Y/c = 0$, $Re_c = 1.35 \times 10^4$, and **(c)** $Y/c = -0.5$, $Re_c = 0.98 \times 10^4$. The black arrow in the upper right corner of each subfigure indicates the direction of the approach stream in the laboratory reference frame. The boundary layer separation location is denoted by the red triangle, open separation at the trailing edge is denoted by the open blue triangle, and reattachment with a closed separation bubble is denoted by the closed blue triangle. Reversed flow is indicated by the shades of pink/purple.

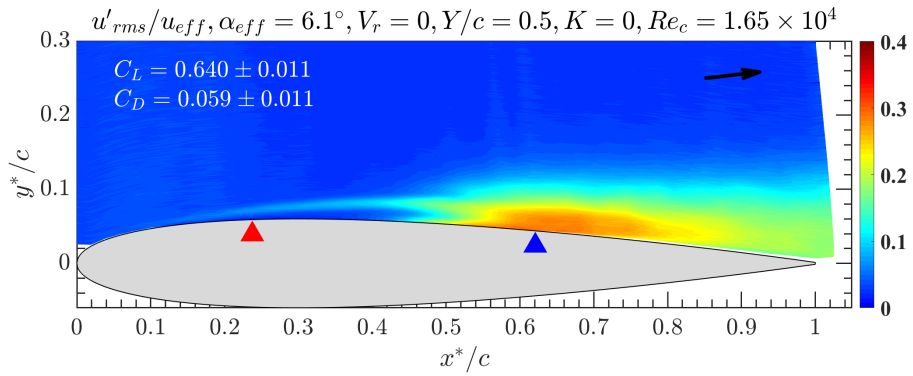

(a)

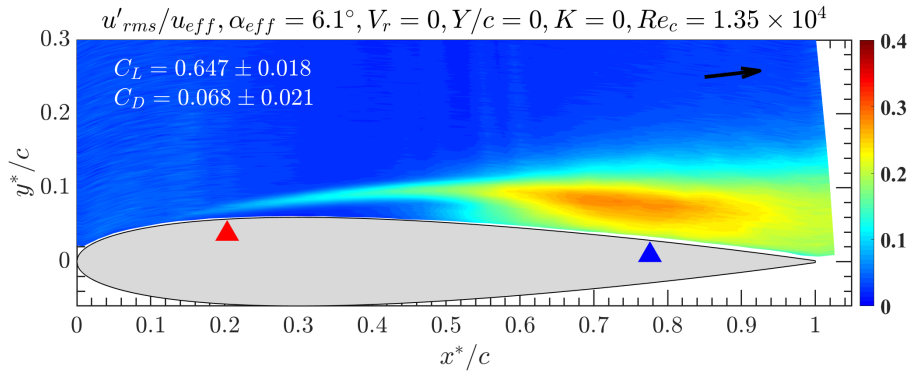

(b)

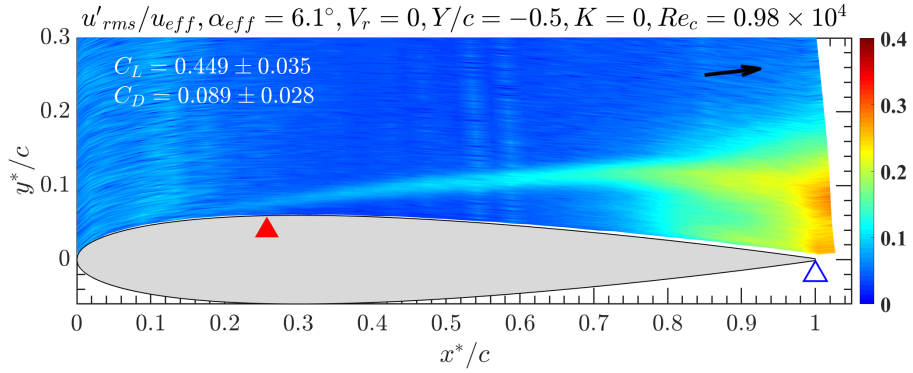

(c)

Figure 3.13: RMS streamwise velocity measurements by 1c-MTV for the stationary airfoil at $\alpha_{eff} = 6.1°$ in uniform flow ($K = 0$) for **(a)** $Y/c = 0.5$, $Re_c = 1.65 \times 10^4$, **(b)** $Y/c = 0$, $Re_c = 1.35 \times 10^4$, and **(c)** $Y/c = -0.5$, $Re_c = 0.98 \times 10^4$. The black arrow in the upper right corner of each subfigure indicates the direction of the approach stream in the laboratory reference frame. The boundary layer separation location is denoted by the red triangle and the open separation at the trailing edge is denoted by the open blue triangle. Reversed flow is indicated by the shades of pink/purple.

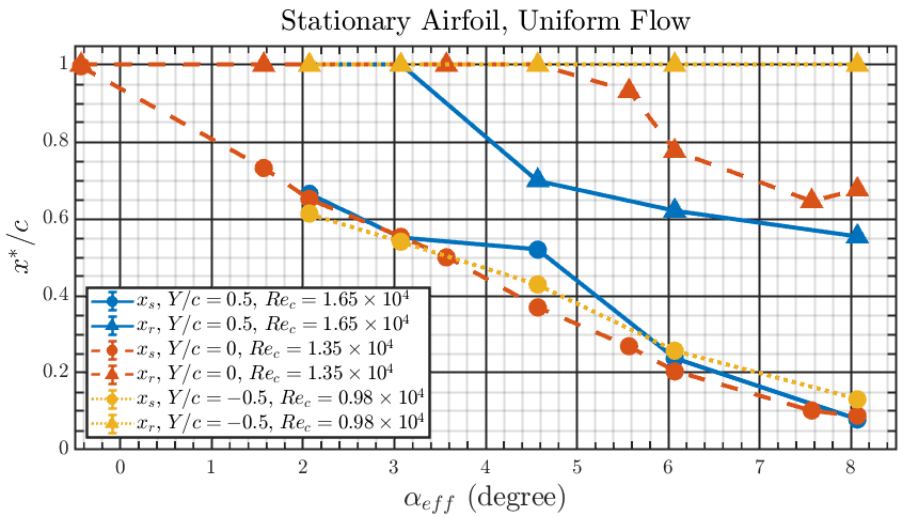

Figure 3.14: The separation and reattachment locations, x_s and x_r, respectively, given by chordwise position x^*/c for the stationary ($V_r = 0$) airfoil in uniform flow ($K = 0$) at **(a)** $Y/c = 0.5$, $Re_c = 1.65 \times 10^4$, **(b)** $Y/c = 0$, $Re_c = 1.35 \times 10^4$, and **(c)** $Y/c = -0.5$, $Re_c = 0.98 \times 10^4$. Circle symbols indicate x_s while triangle symbols indicate x_r. Open separation is indicated by $x^*/c = 1$ in the results for x_r.

CHAPTER 4

SHEAR FLOW RESULTS

In this chapter, the aerodynamic load and streamwise velocity results for the airfoil in shear are presented. First, the stationary airfoil in shear is characterized in comparison to the stationary airfoil in uniform flow at the same Reynolds number to establish the effects of shear, which in turn provides baseline cases for the plunging airfoil in shear. Next, the plunging airfoil in shear is characterized in comparison to the stationary airfoil in shear to investigate the effects of the airfoil traversing across the shear zone. Recall, this study is motivated by determining if, and under what conditions, the load on the plunging airfoil in shear can be approximated by that on the stationary airfoil under the same flow conditions by relating their effective angles of attack. The plunge speeds investigated are varied over an order of magnitude range V_a = 0.1-1.0 cm/s, which correspond to the ratio of plunge speed to the local approach stream (V_r) defined at specific locations in the shear zone; nominally V_r = 0.01-0.1 at the centerline. Performing the measurements over this range of plunge speeds determines how low V_r must be in order for the load on the steadily plunging airfoil to be approximated by that on the steady airfoil. As was done in Chapter 3, the notation of α_{eff} and u' are used for both the stationary and plunging airfoil results to simplify the comparison between them in the reference frame of the airfoil.

4.1 The Effect of Shear and Baseline Cases for the Stationary Airfoil

Aerodynamic load and streamwise velocity measurements in shear are first performed on the stationary airfoil to establish the basic effect of dimensionless shear rate K at each of the respective Re_c values based on cross-stream location, which also provides a baseline for later investigating the effect of the plunging airfoil motion in shear. These measurements are performed in shear at each of the three primary cross-stream locations, Y/c = 0 and ±0.5. The corresponding Re_c and K pairs are listed in Table 2.1.

First examining the mean C_L results for $|\alpha_{eff}| \leq 4^\circ$ in Fig. 4.1, it is observed that one effect

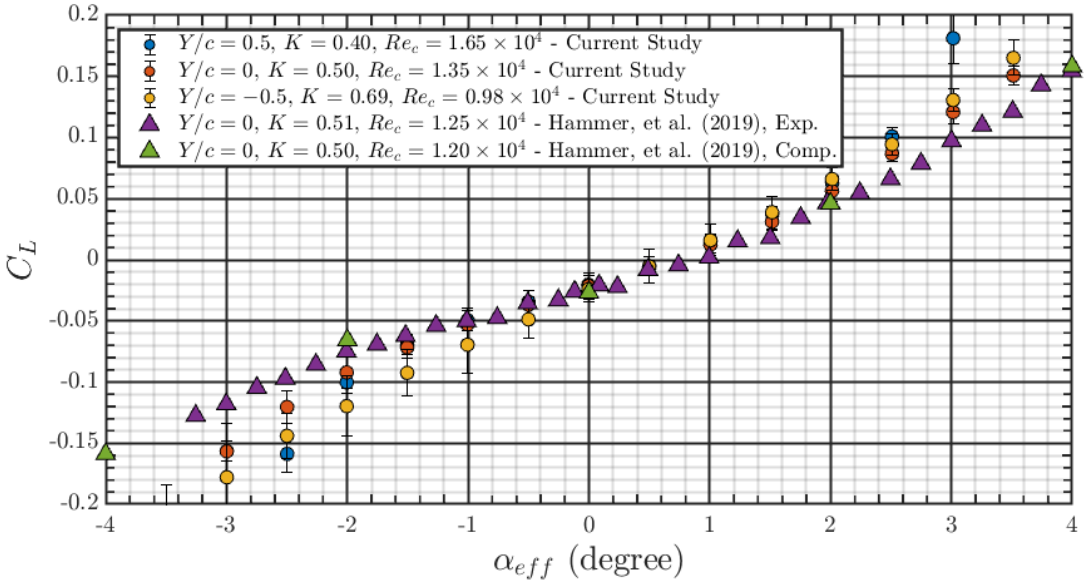

Figure 4.1: C_L-α_{eff} curves for the stationary NACA 0012 airfoil in a uniform-shear freestream for the current study at: $Re_c = 1.65 \times 10^4$ and $K = 0.40$, $Re_c = 1.35 \times 10^4$ and $K = 0.50$, and $Re_c = 0.98 \times 10^4$ and $K = 0.69$; and both the experimental and computational results from Hammer et al. (2019) at $Re_c \approx 1.2 \times 10^4$ and $K \approx 0.5$.

of shear is the negative mean C_L at zero α_{eff}, as opposed to $C_L = 0$ at zero α_{eff} in uniform flow. This effect was first observed in the previous works of Hammer et al. (2018) and Hammer et al. (2019), the latter of which is shown in Fig. 4.1 for comparison. The C_L results for the current study at $K = 0.5$ and $Re_c = 1.35 \times 10^4$ are consistent with the experimental and computational results of Hammer et al. (2019) at similar flow parameters of $K \approx 0.5$ and $Re_c \approx 1.20 \times 10^4$. Hammer et al. (2018) observed that the C_L at zero α_{eff} becomes more negative with increasing K at a fixed $Re_c = 1.20 \times 10^4$, as shown in Fig. 4.2. The C_L results at zero α_{eff} versus K are also shown in Fig. 4.2 for the current study and Albrecht et al. (2022) for several Re_c. An interesting observation from the current results is that the C_L does not become as negative as K increases and Re_c decreases; i.e., the two effects tend to counteract each other. This is why the C_L decreases more slowly than for the results of Hammer et al. (2018) for constant Re_c. A similar observation is inferred from the results of Albrecht et al. (2022) relative to Hammer et al. (2018) and it becomes clear that the effects of Re_c and K are inextricably linked.

Further effect of shear is demonstrated by the mean C_L- and C_D-α_{eff} curves for the stationary

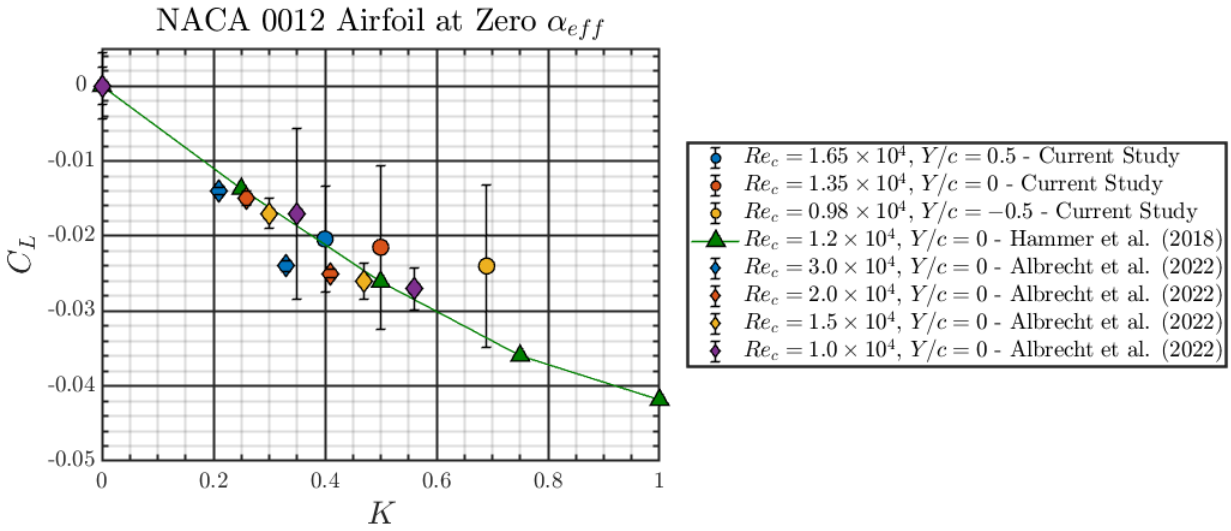

Figure 4.2: Mean C_L at zero α_{eff} versus dimensionless shear rate K for the stationary NACA 0012 airfoil in a uniform-shear freestream for the current study, the computational results from Hammer et al. (2019) at $Re_c = 1.2 \times 10^4$, and the results of Albrecht et al. (2022) at several Re_c.

airfoil in shear at the three cross-stream positions compared with their uniform flow counterparts from Chapter 3. The aerodynamic load results are supplemented by flow measurements at each Y/c location in both uniform flow and shear for subsets of α_{eff}. From these flow measurements, which may be found in full in Appendices E and F, the separation and reattachment locations are characterized in uniform flow and shear at each of the three Y/c locations.

Beginning with the results for $Y/c = 0.5$ and $Re_c = 1.65 \times 10^4$ in Fig. 4.3, it is observed that the effect of shear is generally subtle, as observed by Albrecht et al. (2022) for similar Re_c and K pairs. A multi-region behavior is observed in the C_L-α_{eff} curves in Fig. 4.3a for shear, like for uniform flow as described in Chapter 3. For $K = 0.40$ and $Re_c = 1.65 \times 10^4$, the C_L- and C_D-α_{eff} curves show minor asymmetry compared to the uniform flow case, such as in the angles at which the peak $|C_L|$ occurs, or at $|\alpha_{eff}| \lesssim 3°$ due to the shift in the zero lift angle of attack. Between $2.5° \lesssim \alpha_{eff} \lesssim 6°$ it is observed that the C_L on the airfoil in shear is actually greater than that in uniform flow. The peak $|C_L|$ for shear flow is about 5-8% greater and occurs at an $|\alpha_{eff}|$ about 1° higher than for uniform flow. In Fig. 4.3b, which shows the C_D results for $Y/c = 0.5$ and $Re_c = 1.65 \times 10^4$, the C_D-α_{eff} curve shows asymmetry in shear compared to uniform flow. There is little difference in the C_D between the shear and uniform flow results for $|\alpha_{eff}| \lesssim 5°$, while the

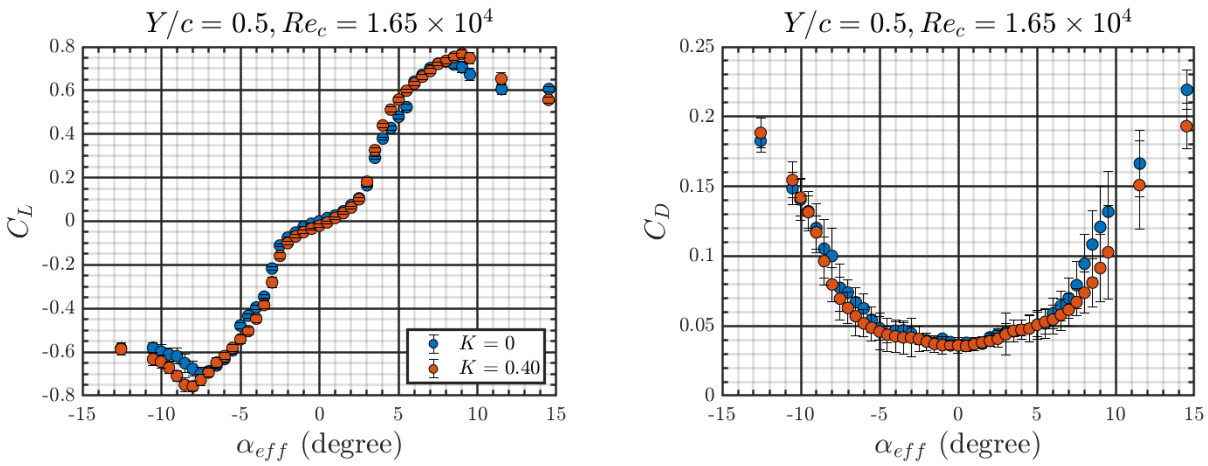

(a) (b)

Figure 4.3: **(a)** C_L- and **(b)** C_D-α_{eff} curves for the stationary airfoil at $Y/c = 0.5$, $Re_c = 1.65 \times 10^4$ in uniform flow ($K = 0$) and shear ($K = 0.40$).

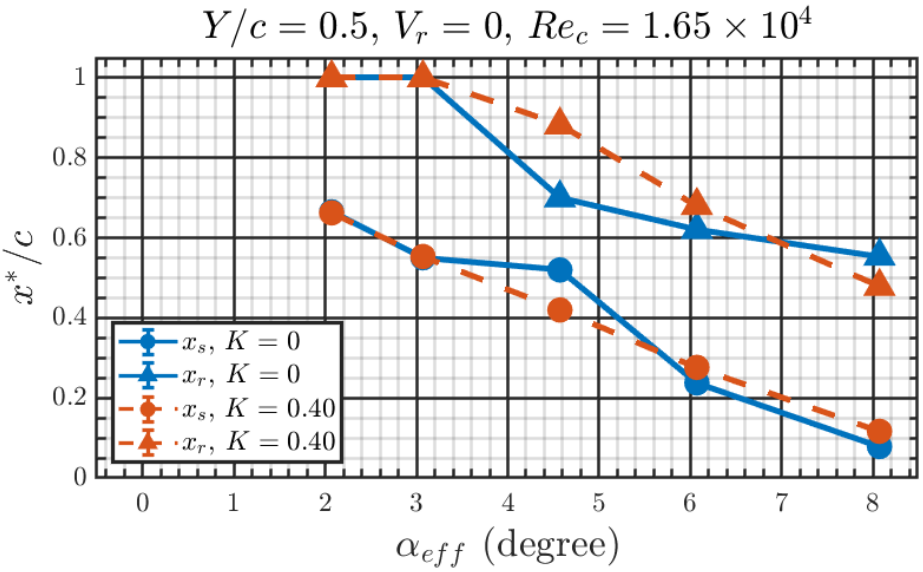

Figure 4.4: The separation and reattachment locations, x_s and x_r, respectively, given by chordwise position x^*/c for the stationary ($V_r = 0$) airfoil at $Y/c = 0.5$ and $Re_c = 1.65 \times 10^4$ in uniform flow ($K = 0$) and shear ($K = 0.40$). Circle symbols indicate x_s while triangle symbols indicate x_r. Open separation is indicated by $x^*/c = 1$ in the results for x_r.

disagreement becomes more pronounced for $|\alpha_{eff}| \gtrsim 5°$.

The separation and reattachment results for $Y/c = 0.5$ and $Re_c = 1.65 \times 10^4$ in Fig. 4.4 show open separation at $\alpha_{eff} = 2.1°$ and $3.1°$ for both the uniform flow and shear cases, with agreement in their separation locations x_s. At $\alpha_{eff} = 4.6°$, reattachment on the airfoil has occurred in both uniform flow and shear; however, x_s is $0.1c$ further upstream, and x_r is $0.18c$ further downstream,

for shear compared to uniform flow. Interestingly, despite this drastic difference in flow behavior, the C_L- and C_D-α_{eff} results in Fig. 4.3 show little difference between uniform flow and shear. From $\alpha_{eff} = 6.1°$ to $8.1°$, the x_s for both uniform flow and shear move upstream at about the same rate, although the resolution in α_{eff} is coarse, with the x_s for shear consistently further downstream than uniform flow by about $0.04c$. The x_r is observed to continue to move further upstream in both uniform flow and shear between $\alpha_{eff} = 6.1°$ and $8.1°$. More generally, the switch from open separation to a closed separation bubble between $\alpha_{eff} = 3.1°$ and $4.6°$ coincides with the rapid change in slope of the C_L-α_{eff} curve in Fig. 4.3a.

For the C_L- and C_D-α_{eff} curves at $Y/c = 0$ and $Re_c = 1.35 \times 10^4$ shown in Fig. 4.5, the C_L in shear is observed to be less than that in uniform flow for a large portion of the curve, $-10° \lesssim \alpha_{eff} \lesssim 8°$. The largest differences in the C_L curves between uniform flow and shear occur around $|\alpha_{eff}| \approxeq 5°$, where the curves see a rapid change in slope due to the process of the airfoil switching from an open separation to a closed separation bubble as discussed in Chapter 3. The corresponding C_D results near $|\alpha_{eff}| \approxeq 5°$ also show variation between uniform flow and shear.

The boundary layer separation and reattachment results for $Y/c = 0$ and $Re_c = 1.35 \times 10^4$ between uniform flow and shear are shown in Fig. 4.6, noting the α_{eff} resolution is higher than at the other Y/c positions. It is observed that the x_s on the airfoil in both uniform flow and shear moves upstream nearly linearly with α_{eff}, though at a faster rate for the former than the latter. Although the x_s starts further upstream on the airfoil surface in shear than for uniform flow, the difference in rate of movement upstream leads to a crossover at $\alpha_{eff} \approxeq 3.3°$, after which the x_s for uniform flow is upstream of that for shear. It is observed that reattachment occurs in shear at a higher α_{eff} than for uniform flow, where the former occurs between $6.1° \lesssim \alpha_{eff} \lesssim 7.6°$ and the latter occurs between $4.6° \lesssim \alpha_{eff} \lesssim 5.6°$. The observed delayed reattachment in shear compared to uniform flow at this particular Reynolds number is interesting as the results for $Re_c = 1.65 \times 10^4$ and those of Albrecht et al. (2022) for $Re_c = 1.5\text{-}3.0 \times 10^4$ show the presence of shear does not noticeably impact the angle at which reattachment occurs. For $\alpha_{eff} \geq 4.6°$, the x_s and x_r for uniform flow are both further upstream than for shear flow, which corresponds to the observed rapid change in

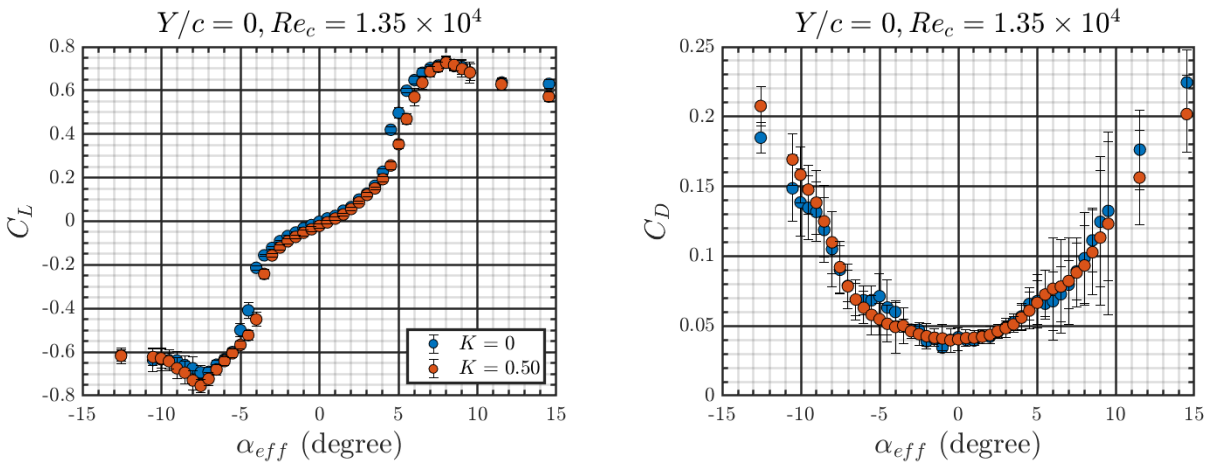

Figure 4.5: **(a)** C_L- and **(b)** C_D-α_{eff} curves for the stationary airfoil at $Y/c = 0$, $Re_c = 1.35 \times 10^4$ in uniform flow ($K = 0$) and shear ($K = 0.50$).

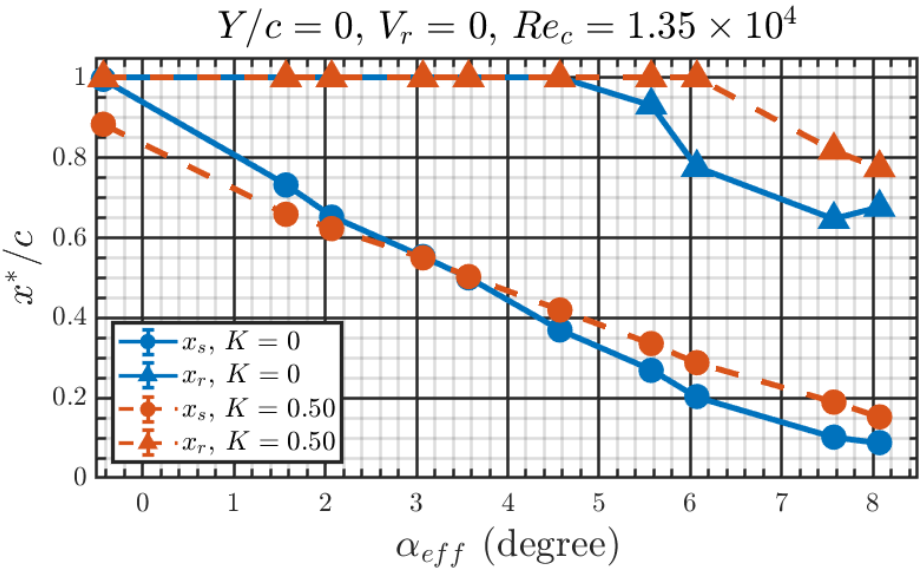

Figure 4.6: The separation and reattachment locations, x_s and x_r, respectively, given by chordwise position x^*/c for the stationary ($V_r = 0$) airfoil at $Y/c = 0$ and $Re_c = 1.35 \times 10^4$ in uniform flow ($K = 0$) and shear ($K = 0.50$). Circle symbols indicate x_s while triangle symbols indicate x_r. Open separation is indicated by $x^*/c = 1$ in the results for x_r.

slope of the C_L-α_{eff} curve in Fig. 4.5a for uniform flow occurring at lower α_{eff} than for shear.

The transition in the flow pattern from an open separation to a closed separation bubble in shear is demonstrated in Fig. 4.7, which shows the mean streamwise velocity u'/u_{eff} of the flow over the airfoil for $Y/c = 0$, $K = 0.5$ and $Re_c = 1.35 \times 10^4$ at multiple α_{eff}. From $\alpha_{eff} = 4.6°$ in Fig. 4.7a, to $\alpha_{eff} = 6.1°$ in Fig. 4.7b, to $\alpha_{eff} = 7.6°$ in Fig. 4.7c, the open separation clearly

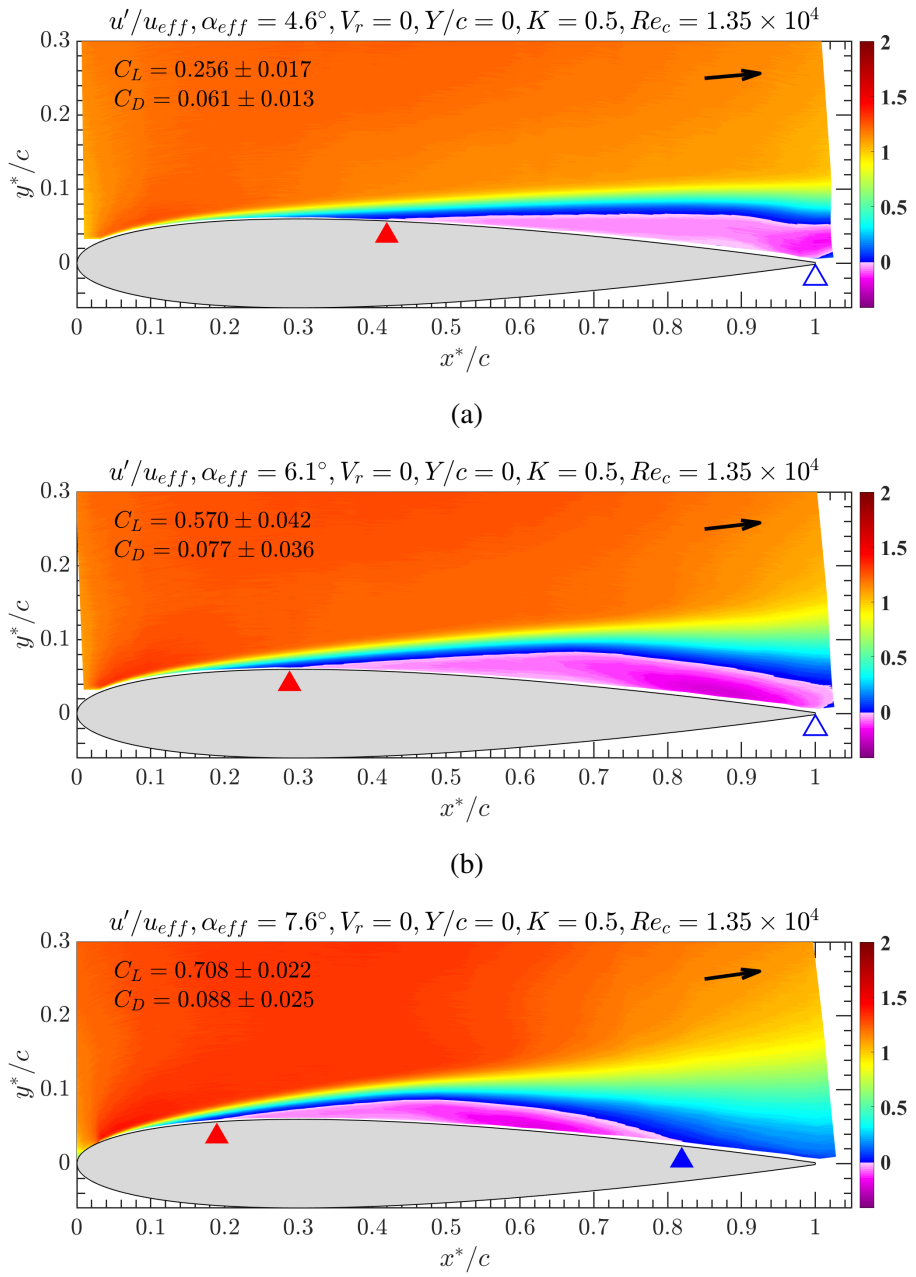

Figure 4.7: Mean streamwise velocity measurements by 1c-MTV for the stationary airfoil in shear flow for $Y/c = 0$, $K = 0.50$, and $Re_c = 1.35 \times 10^4$ for **(a)** $\alpha_{eff} = 4.6°$, **(b)** $\alpha_{eff} = 6.1°$, and **(c)** $\alpha_{eff} = 7.6°$. The black arrow in the upper right corner of each subfigure indicates the direction of the approach stream in the laboratory reference frame. The boundary layer separation location is denoted by the red triangle, open separation at the trailing edge is denoted by the open blue triangle, and reattachment with a closed separation bubble is denoted by the closed blue triangle. Reversed flow is indicated by the shades of pink/purple.

switches to a closed separation bubble, with an increase in C_L by a factor of ultimately about 2.8. See Appendices E and F for additional contour plots demonstrating the flow transition, including the RMS streamwise velocity results corresponding to Fig. 4.7.

The C_L- and C_D-α_{eff} curves at Y/c = -0.5 and $Re_c = 0.98 \times 10^4$ in Fig. 4.8 show the strongest effect of shear among the three Y/c positions, noting that it is the case with highest K and lowest Re_c. Particularly, the asymmetry in the C_L- and C_D-α_{eff} curves in Fig. 4.8 for shear is very strong. For the airfoil in shear, the peak $|C_L|$ at $\alpha_{eff} \cong$ -7° is about 40-43% greater than the $|C_L|$ at $|\alpha_{eff}| \cong 9°$ in uniform flow. Moreover, the C_L results in shear at negative α_{eff} show a traditional leading edge stall behavior, compared to the plateau-like stall behavior either in shear at positive α_{eff} or in uniform flow at either positive or negative α_{eff}. From Fig. 4.8b, it is observed that the C_D in shear is higher than in uniform flow for $\alpha_{eff} \lesssim 7°$, while fair agreement between uniform flow and shear is observed in the range of $7° \lesssim \alpha_{eff} \lesssim 15°$.

In Fig. 4.9, which shows the separation and reattachment results between uniform flow and shear for Y/c = -0.5 and $Re_c = 0.98 \times 10^4$, it is observed that the x_s for shear is consistently further downstream than for uniform flow over the α_{eff} studied. Between $2.1° \lesssim \alpha_{eff} \lesssim 4.6°$, the x_s is about $0.06c$ further downstream in shear than in uniform, where the corresponding C_L results in Fig. 4.8a show close agreement, and the C_D results in Fig. 4.8b show disagreement. As α_{eff} increases past 4.6°, the difference in x_s between uniform flow and shear increases, up to $0.14c$ at $\alpha_{eff} = 8.1°$, which corresponds with a greater C_L for uniform flow than shear.

The C_L- and C_D-α_{eff} curves for the stationary airfoil in shear at each Y/c are compared against each other in Fig. 4.10. Although the effects of Re_c and K are both present in the results in Fig. 4.10, the comparison allows for general observations to be made for the airfoil located at different positions in the same shear approach stream, which is motivated by the airfoil traversing across the width of the shear zone in the current work. The C_L-α_{eff} curves between $0° \lesssim \alpha_{eff} \lesssim 8°$ show a pattern similar to what was observed over the same angle range in uniform flow (see Fig. 3.9a). For example, the C_L-α_{eff} results in shear are characterized by initial agreement between the three cases up to $\alpha_{eff} \cong 2.5°$, after which the slope of the curve for K = 0.40 and $Re_c = 1.65 \times 10^4$

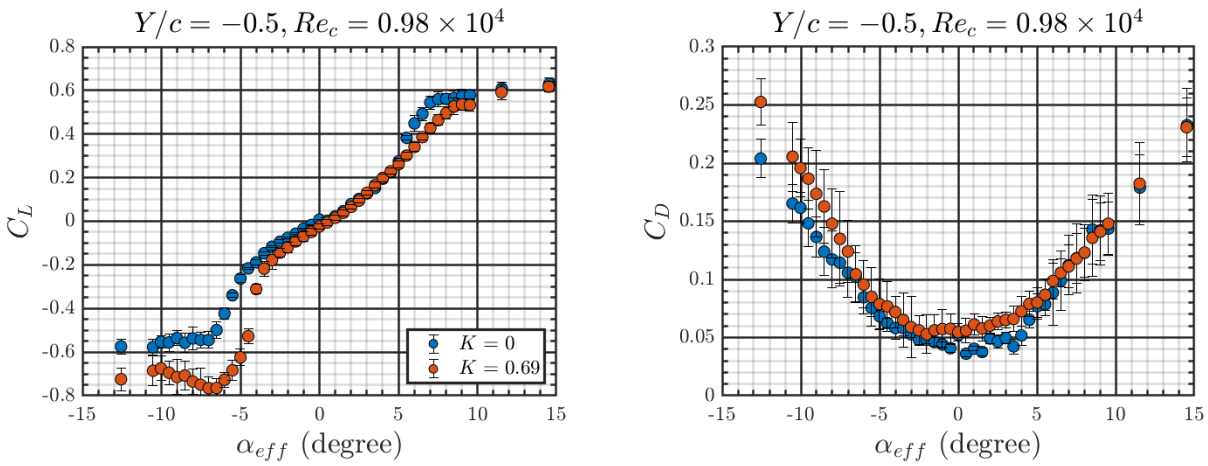

(a) (b)

Figure 4.8: **(a)** C_L- and **(b)** C_D-α_{eff} curves for the stationary airfoil at Y/c = -0.5, $Re_c = 0.98 \times 10^4$ in uniform flow (K = 0) and shear (K = 0.69).

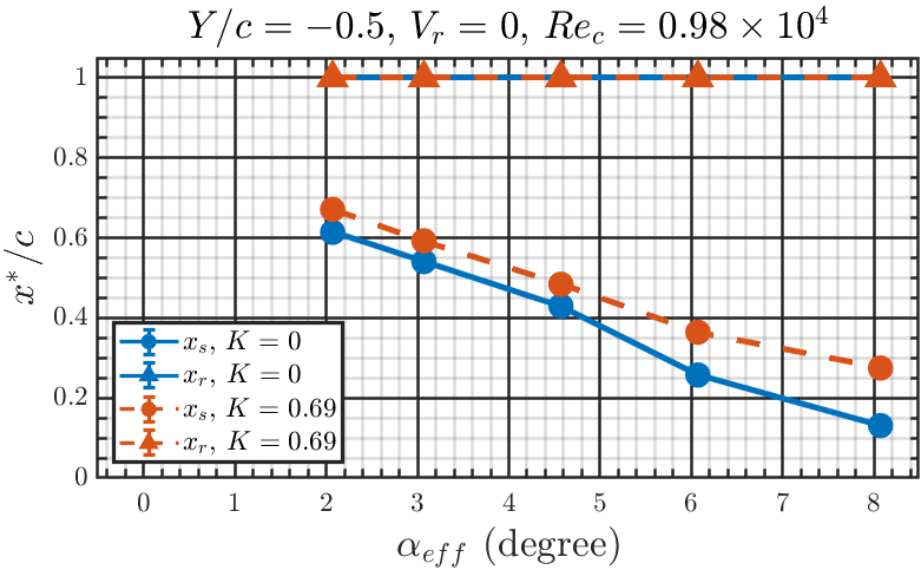

Figure 4.9: The separation and reattachment locations, x_s and x_r, respectively, given by chordwise position x^*/c for the stationary ($V_r = 0$) airfoil at $Y/c = -0.5$ and $Re_c = 0.98 \times 10^4$ in uniform flow ($K = 0$) and shear ($K = 0.69$). Circle symbols indicate x_s while triangle symbols indicate x_r. Open separation is indicated by $x^*/c = 1$ in the results for x_r.

rapidly increases. There is continued agreement between the two other cases with lower Re_c and higher K up to $\alpha_{eff} \cong 4°$, after which the slope of the curve for K = 0.50 and $Re_c = 1.35 \times 10^4$ rapidly increases. At negative angles of attack, the C_L results in Fig. 4.10a show much less effect of shear compared to positive angles, and a crossover of each of the three C_L-α_{eff} curves is observed at $\alpha_{eff} \cong -4°$. Interestingly, the peak $|C_L|$ at negative α_{eff} for each case is approximately the same, around C_L = -0.76; however, the $|\alpha_{eff}|$ at which it occurs decreases with increasing K and decreasing Re_c. The C_D results for the airfoil in shear in Fig. 4.10b show the systematic increase in C_D with increasing K and decreasing Re_c based on the cross-stream position in the shear zone. This is in contrast with the C_D results in uniform flow which showed agreement at each Re_c at low angles of attack (see Fig. 3.9b).

The variation in C_L and C_D for each K and Re_c pair is explored further by considering the corresponding boundary layer separation and reattachment locations for a subset of the positive α_{eff} range investigated, as shown in Fig. 4.11. The x_s for the two higher Re_c, lower K cases show close agreement, while the x_s for the highest K, lowest Re_c case is consistently further downstream than the other two. The switch from open separation to a closed separation bubble is captured in the results for x_r, which shows the K = 0.40 and $Re_c = 1.65 \times 10^4$ case switching first between $3.1° \lesssim \alpha_{eff} \lesssim 4.6°$, followed by the K = 0.50 and $Re_c = 1.35 \times 10^4$ case between $6.1° \lesssim \alpha_{eff} \lesssim 7.6°$. The K = 0.69 and $Re_c = 0.98 \times 10^4$ case shows only open separation, as is the case for uniform flow at the same Re_c.

The difference in the flow behavior is exemplified in Figs. 4.12 and 4.13, which show the mean streamwise and RMS velocity results, respectively, for the stationary airfoil at $\alpha_{eff} = 6.1°$ and each K and Re_c pair. Flow results for the other angles are provided in Appendix F. At K = 0.40 and $Re_c = 1.65 \times 10^4$ in Fig. 4.12a, there is a closed separation bubble covering about 40% of the airfoil surface, and correspondingly in Fig. 4.13a the streamwise location of the maximum fluctuation is at approximately the same streamwise location as the reattachment point. By contrast, at K = 0.50 and $Re_c = 1.35 \times 10^4$ in Fig. 4.12b, open separation is observed with reverse flow covering 71% of the airfoil surface and extending only about $0.02c$ past the trailing edge. The corresponding RMS

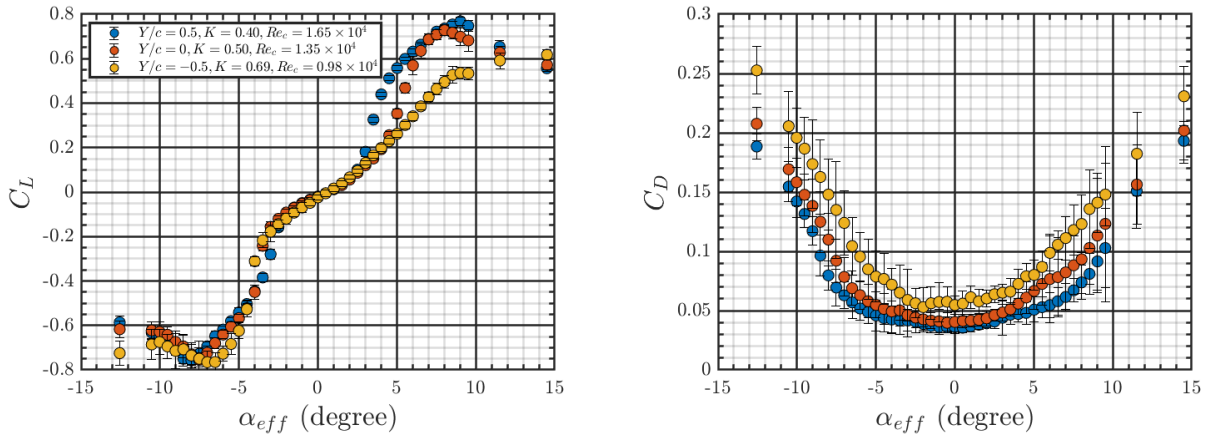

(a) (b)

Figure 4.10: **(a)** C_L- and **(b)** C_D-α_{eff} curves for the stationary airfoil in shear flow at each cross-stream position: $Y/c = 0.5$, $K = 0.40$, $Re_c = 1.65 \times 10^4$; $Y/c = 0$, $K = 0.50$, $Re_c = 1.35 \times 10^4$;Y/c = -0.5, $K = 0.69$, $Re_c = 0.98 \times 10^4$.

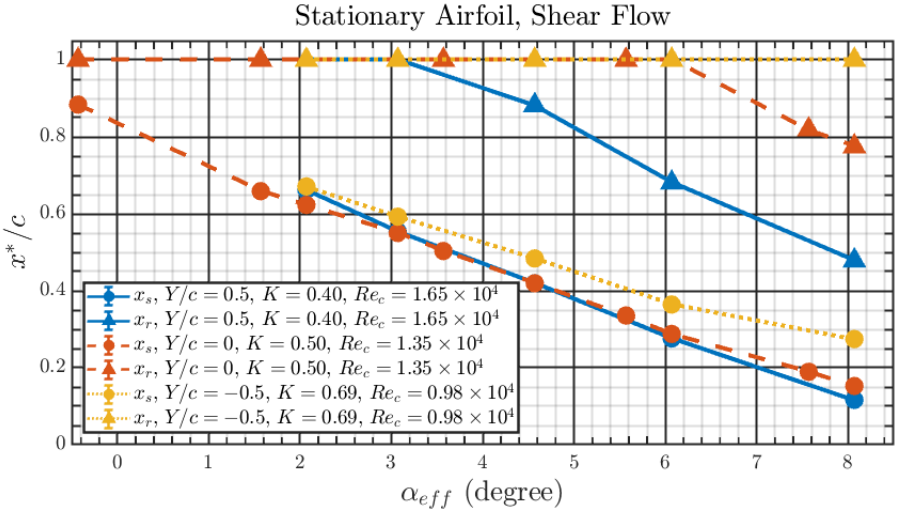

Figure 4.11: The separation and reattachment locations, x_s and x_r, respectively, given by chordwise position x^*/c for the stationary ($V_r = 0$) airfoil in shear flow at **(a)** $Y/c = 0.5$, $K = 0.40$, $Re_c = 1.65 \times 10^4$, **(b)** $Y/c = 0$, $K = 0.50$, $Re_c = 1.35 \times 10^4$, and **(c)** $Y/c = -0.5$, $K = 0.69$, $Re_c = 0.98 \times 10^4$. Circle symbols indicate x_s while triangle symbols indicate x_r. Open separation is indicated by $x^*/c = 1$ in the results for x_r.

velocity results in Fig. 4.13b shows a region of high RMS formed above and downstream of the trailing edge. At $K = 0.69$ and $Re_c = 0.98 \times 10^4$ in Fig. 4.12c, open separation is observed with reversed flow covering about 64% of the airfoil surface and in Fig. 3.13c the high RMS region appears to be formed downstream the trailing edge.

Summarizing the results for the stationary airfoil in shear, it is observed that the current study reproduces the negative C_L at zero angle of attack consistent with recent computational and experimental work from TMUAL. The C_L- and C_D-α_{eff} curves for the stationary airfoil in shear typically show a weak effect of shear at higher Re_c and lower K, and vice versa. The two higher Re_c, lower K cases exhibit a similar multi-region behavior that is observed in uniform flow, which is connected to the airfoil switching from open separation to a closed separation bubble. At positive α_{eff}, the flow switching from open separation to a closed separation bubble occurs at higher α_{eff} in shear compared to in uniform flow for $Re_c = 1.35 \times 10^4$, whereas there is no observed change in the α_{eff} for $Re_c = 1.65 \times 10^4$. For the highest K, lowest Re_c case, only open separation is observed at positive α_{eff}, like the corresponding results in uniform flow. The common observation in the C_L- and C_D-α_{eff} curves for the stationary airfoil in shear is asymmetry, which is shown, for example, by the different stall behavior between positive and negative angles of attack.

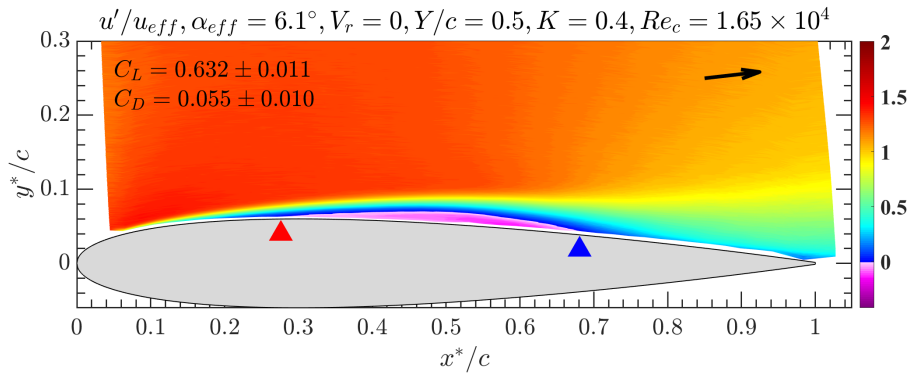

(a)

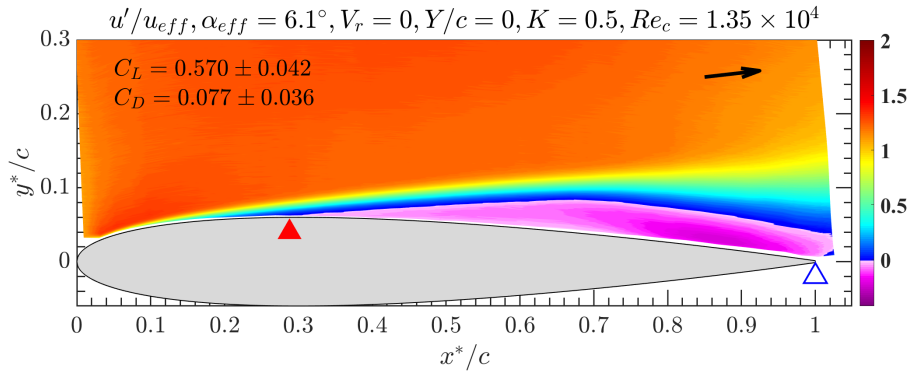

(b)

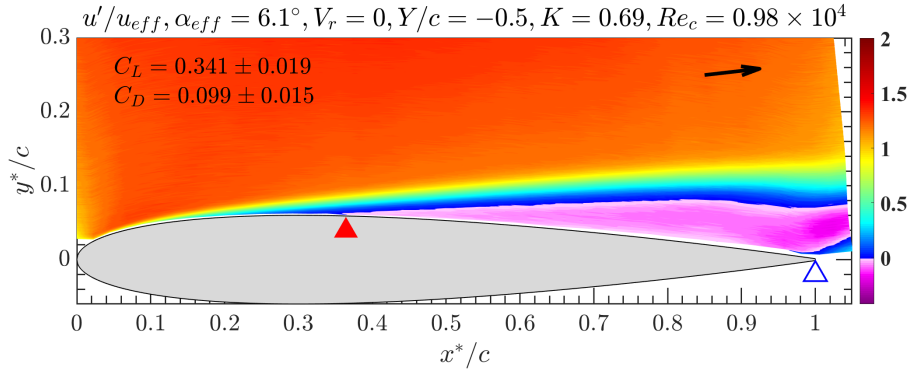

(c)

Figure 4.12: Mean streamwise velocity measurements by 1c-MTV for the stationary airfoil at $\alpha_{eff} = 6.1°$ in shear flow for **(a)** $Y/c = 0.5$, $K = 0.40$, $Re_c = 1.65 \times 10^4$, **(b)** $Y/c = 0$, $K = 0.50$, $Re_c = 1.35 \times 10^4$, and **(c)** $Y/c = -0.5$, $K = 0.69$, $Re_c = 0.98 \times 10^4$. The black arrow in the upper right corner of each subfigure indicates the direction of the approach stream in the laboratory reference frame. The boundary layer separation location is denoted by the red triangle, open separation at the trailing edge is denoted by the open blue triangle, and reattachment with a closed separation bubble is denoted by the closed blue triangle. Reversed flow is indicated by the shades of pink/purple.

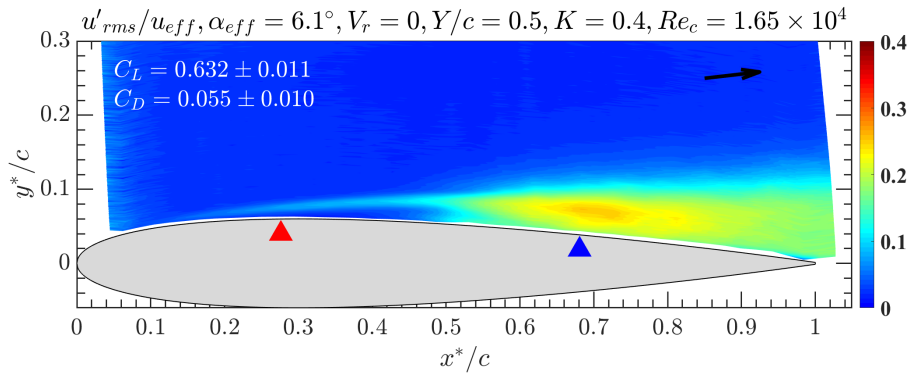

(a)

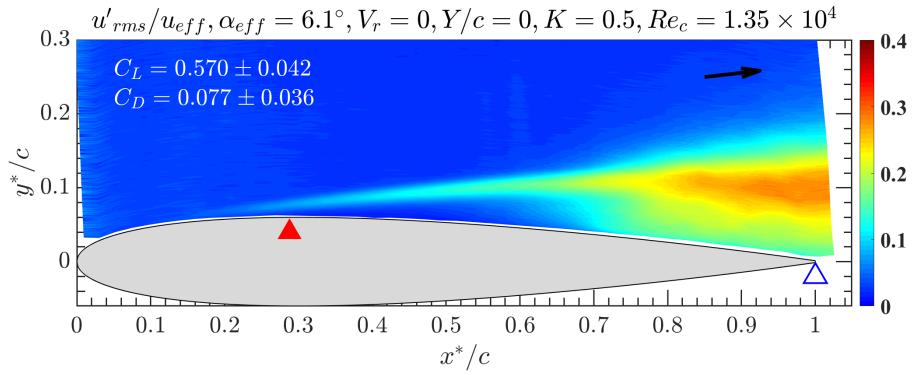

(b)

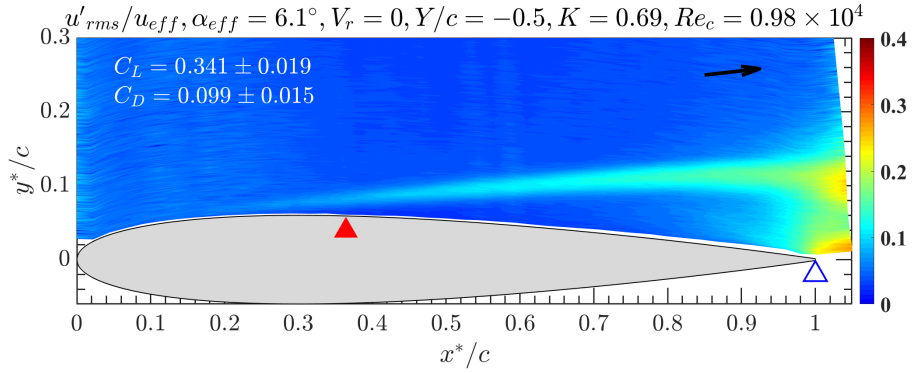

(c)

Figure 4.13: RMS streamwise velocity measurements by 1c-MTV for the stationary airfoil at $\alpha_{eff} = 6.1°$ in shear flow for **(a)** $Y/c = 0.5$, $K = 0.40$, $Re_c = 1.65 \times 10^4$, **(b)** $Y/c = 0$, $K = 0.50$, $Re_c = 1.35 \times 10^4$, and **(c)** $Y/c = -0.5$, $K = 0.69$, $Re_c = 0.98 \times 10^4$. The black arrow in the upper right corner of each subfigure indicates the direction of the approach stream in the laboratory reference frame. The boundary layer separation location is denoted by the red triangle, open separation at the trailing edge is denoted by the open blue triangle, and reattachment with a closed separation bubble is denoted by the closed blue triangle.

4.2 Plunging Airfoil Load and Flow Results for V_a = 0.5 and 1.0 cm/s

In this section, the aerodynamic load on the steadily plunging airfoil in a positive uniform-shear approach stream is compared to its stationary airfoil counterpart by relating their α_{eff} and u_{eff}, the apparent angle of attack and local approach velocity, respectively, in the reference frame of the airfoil. It is here that the central purpose of this study is examined, which is to determine the conditions, if any exist, under which the aerodynamic load on the steadily plunging airfoil in shear in the reference frame of the airfoil is the same as that on the stationary airfoil after considering α_{eff} and u_{eff}. In a uniform freestream, the load on the steadily plunging airfoil can be predicted by relating it to the stationary airfoil, or vice versa, in the reference frame of the airfoil using a simple Galilean transformation. However, it is unknown whether the same relationship can be made for the airfoil steadily moving perpendicular to the freestream direction in shear flow. Knowing whether a connection between the stationary and moving airfoil aerodynamics in shear flow can be made, and the conditions under which such a connection works, can alleviate the need to conduct experiments and/or computations on a moving model to study the aerodynamics of airfoils steadily traversing across shear flow.

The load comparisons between the stationary and plunging airfoils are made at the three primary cross-stream locations in the shear zone, Y/c = 0 and ±0.5, for -15° < α_{eff} < 15°. The chord Reynolds number (Re_c) and dimensionless shear (K) pairs are different at each Y/c location by nature of the linearly varying approach stream. Since the freestream parameters are fixed at each position, the influence of the airfoil motion can be studied relative to the stationary airfoil under the same flow conditions.

Note, it is considered that $u_{eff} \cong u_0$ since typically $V_r^2 \ll 1$ for the plunging airfoil in shear, as was done for the uniform flow plunging airfoil results. For simplicity, the Re_c values noted are based on the local freestream velocity u_0, though u_{eff} is used to precisely calculate the load coefficients in the airfoil frame of reference. The sensitivity in Re_c noted in Chapter 2 is not considered regarding the relation between the stationary and moving airfoils since the variation is expected to be small, scaling with $\sqrt{1 + {V_r}^2}$. The load results on the plunging airfoil are supplemented with mean and

RMS streamwise velocity measurements at the centerline position, $Y/c = 0$, which are also related to those for the stationary airfoil by equating the α_{eff} and u_{eff}. The flow measurements provide a physical description of the observations in the load results, including the overall flow structure, separation and reattachment locations, and boundary layer thickness.

The C_L- and C_D-α_{eff} curves for the stationary and plunging airfoils in shear at each of the three Y/c locations are first examined in Figs. 4.14-4.16. The two plunge speeds investigated are V_a = 0.5 and 1.0 cm/s, which correspond to the V_r values noted in the figures. Beginning with the C_L and C_D results for $Y/c = 0.5$ in Fig. 4.14, where $K = 0.40$ and $Re_c = 1.65 \times 10^4$, it is observed at $\alpha_{eff} = 0$ that the C_L on the plunging airfoil is greater than for the stationary airfoil. Shown more closely in the inset plot in Fig. 4.14a, the C_L at zero α_{eff} increases as V_r increases, with $C_L < 0$ for $V_r = 0.04$ and $C_L \cong 0$ for $V_r = 0.08$. Note, however, that these differences are small within the context of the measurement uncertainty in both the C_L and α_{eff} denoted by the uncertainty bars. More generally, close agreement in C_L is observed between the stationary and the moving airfoil cases for -2° $\lesssim \alpha_{eff} \lesssim$ 8°, while for -8° $\lesssim \alpha_{eff} \lesssim$-2°, the $V_r = 0.08$ plunging airfoil results show a $|C_L|$ between 5-10% greater than the other cases. For $|\alpha_{eff}| \geq 8°$, there is little agreement between the stationary and moving airfoil cases, especially at positive α_{eff}. Though the data are coarse for $\alpha_{eff} \geq 8°$, the peak C_L and the α_{eff} at which it occurs are observed to increase with increasing V_r. At negative α_{eff}, the peak $|C_L|$ on the plunging airfoil is only about 3% greater than on the stationary airfoil, while the α_{eff} at which peak $|C_L|$ occurs for either is approximately the same.

The C_D results in 4.14b show that at zero α_{eff} the C_D on the airfoil for $V_r = 0.04$ is about 24% lower than for $V_r = 0$, while for $V_r = 0.08$ it is only 13% lower. More generally, for -7° $\lesssim \alpha_{eff} \lesssim$ 3° the plunging airfoil cases show a lower $|C_D|$ compared to the stationary airfoil, while there is surprisingly good agreement between each of the cases for -15° $\lesssim \alpha_{eff} \lesssim$ -7° and 3° $\lesssim \alpha_{eff} \lesssim$ 8°. Considering the overall shapes of the C_L- and C_D-α_{eff} results at $K = 0.40$ and $Re_c = 1.65 \times 10^4$, the load on the plunging airfoil up to $V_r = 0.08$ is well-approximated by the load on the stationary airfoil under the same flow conditions over a large range of the α_{eff} investigated, apart from angles

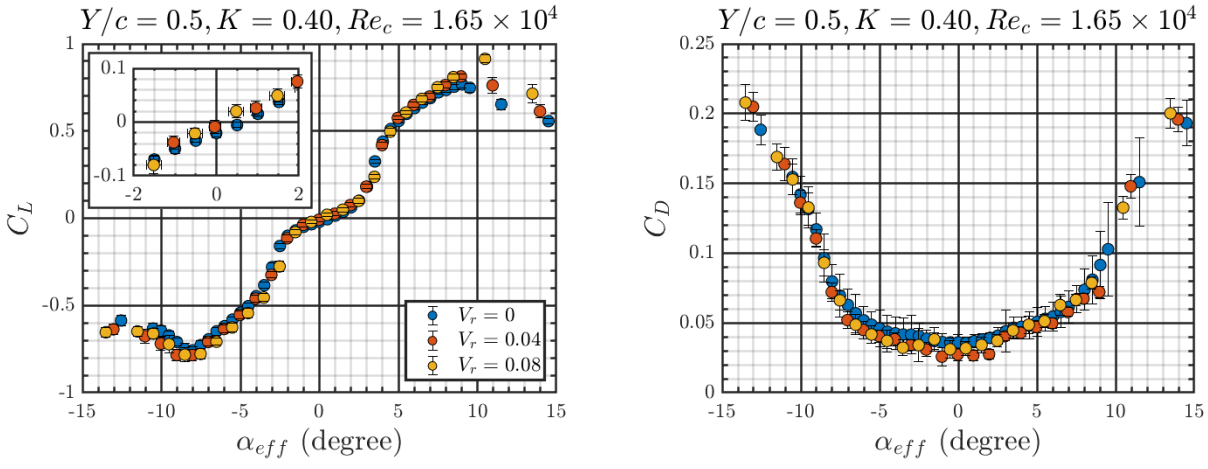

(a) (b)

Figure 4.14: **(a)** C_L- and **(b)** C_D-α_{eff} curves comparing the stationary ($V_r = 0$) and plunging ($V_r \neq 0$) airfoils in shear flow at $Y/c = 0$ where $K = 0.40$ and $Re_c = 1.65 \times 10^4$. The inset plot shows a zoomed-up view of the C_L-α_{eff} curve near zero α_{eff}, including uncertainty bars for α_{eff} that are otherwise smaller than the symbol size in the main plot.

beyond positive angle of attack stall.

The C_L and C_D results in Fig. 4.15 for $Y/c = 0$, where $K = 0.50$ and $Re_c = 1.35 \times 10^4$, show considerably more variation compared to the results at $Y/c = 0.5$. Similar to the case at $Y/c = 0.5$, the C_L at zero α_{eff} in Fig. 4.15a tends to be slightly higher for the plunging airfoil cases compared to the stationary airfoil. Connecting the data surrounding zero α_{eff} in the inset plot of Fig. 4.15a, the C_L at zero α_{eff} for $V_r = 0.05$ is slightly negative, while for $V_r = 0.1$ the $C_L \approxeq 0$; however, the differences are very close to the measurement uncertainty. At positive α_{eff}, it is observed that the rapid rise in the slope of the C_L-α_{eff} curve occurs at a lower α_{eff} for the plunging airfoil than for the stationary airfoil, but it is unclear whether the α_{eff} at which the slope change occurs is the same for both plunging airfoil cases. A higher C_L is observed on the plunging airfoil compared to the stationary airfoil for positive α_{eff} approaching stall, which is further observed in the increasing peak C_L with increasing V_r. At negative α_{eff}, it is observed that there is a rapid rise in the slope of the C_L-α_{eff} curve, which begins at smaller $|\alpha_{eff}|$ with increasing V_r. For $V_r = 0$, this rise in slope occurs at $\alpha_{eff} \approxeq$ -3°, while for $V_r = 0.05$ and $V_r = 0.1$ it occurs at $\alpha_{eff} \approxeq$ -2° and $\alpha_{eff} \approxeq$ -1.5°, respectively. The positive α_{eff} at which peak C_L occurs for the plunging airfoil cases is

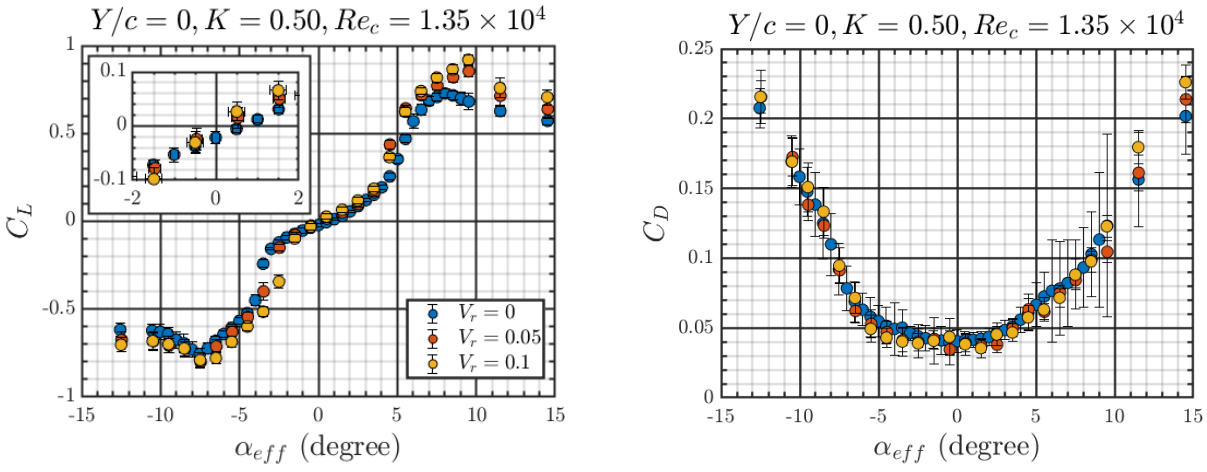

(a) (b)

Figure 4.15: **(a)** C_L- and **(b)** C_D-α_{eff} curves comparing the stationary ($V_r = 0$) and plunging ($V_r \neq 0$) airfoils in shear flow at $Y/c = 0$ where $K = 0.50$ and $Re_c = 1.35 \times 10^4$. The inset plot shows a zoomed-up view of the C_L-α_{eff} curve near zero α_{eff}, including uncertainty bars for α_{eff} that are otherwise smaller than the symbol size in the main plot.

about 2° greater than for the stationary airfoil, whereas the peak $|C_L|$ at negative α_{eff} appears to be the approximately the same between all cases.

The results in 4.15b show close agreement overall between the C_D on the stationary airfoil and $V_r = 0.05$ and 0.1 cases for -15° $\lesssim \alpha_{eff} \lesssim$ 9°. The plunging airfoil cases tend to show a slightly lower $|C_D|$ for -7° $\lesssim \alpha_{eff} \lesssim$ 3° compared to the stationary airfoil, though the difference is close to the measurement uncertainty. Given the variation near zero α_{eff}, it is difficult to precisely determine how the C_D for the $V_r = 0.05$ and $V_r = 0.1$ plunging airfoils at zero α_{eff} compared to that for the stationary airfoil. For $\alpha_{eff} \gtrsim 9°$, which is beyond stall for each of the cases, the C_D on the plunging airfoil is greater than that on the stationary airfoil and increases with increasing V_r.

Considering the overall C_L-α_{eff} results at $K = 0.50$ and $Re_c = 1.35 \times 10^4$, good agreement is observed between the stationary airfoil and $V_r = 0.05$ plunging airfoil case at negative and low-positive α_{eff}, but not at α_{eff} approaching positive angle of attack stall and beyond. The $V_r = 0.1$ plunging airfoil case overall shows little agreement in C_L with the stationary airfoil C_L, with only loose agreement at low α_{eff}. More importantly, it is observed that the $|C_L|$ on the plunging airfoil is greater than that on the stationary airfoil under these flow conditions at α_{eff} associated with

the rapid rise in the slope of the $|C_L|$ curve. At positive α_{eff}, it is observed that the maximum C_L, and the α_{eff} at which it occurs, are greater for the plunging airfoil than for the stationary airfoil and increase with increasing V_r. The corresponding flow measurements for this behavior will be discussed later. By contrast, the C_D-α_{eff} curves for the plunging airfoil at K = 0.50 and $Re_c = 1.35 \times 10^4$ are well-approximated by the C_D on the stationary airfoil under the same flow conditions over a large range of the α_{eff} investigated.

The C_L and C_D results in Fig. 4.16 for Y/c = -0.5, where K = 0.69 and $Re_c = 0.98 \times 10^4$, i.e., the highest K, lowest Re_c pair studied, show the most variation between the stationary and plunging airfoils compared to the results at Y/c = 0 and 0.5. From the inset plot of Fig. 4.16a, the C_L at zero α_{eff} for V_r = 0.07 is slightly negative, while for V_r = 0.14 the $C_L \approxeq 0$ at zero α_{eff}, noting the highest uncertainty in α_{eff} on the plunging airfoil is observed at these flow conditions. There is a rapid rise in the slope of the C_L-α_{eff} curve at negative α_{eff} which occurs at smaller $|\alpha_{eff}|$ with increasing V_r. For example, for V_r = 0 this rise in slope occurs at $\alpha_{eff} \approxeq$ -3°, while for V_r = 0.05 and V_r = 0.1 it occurs at $\alpha_{eff} \approxeq$ -2.5° and $\alpha_{eff} \approxeq$ -0.5°, respectively. The peak $|C_L|$ on the moving airfoil at negative α_{eff} is not as greatly affected as at positive α_{eff} compared to the stationary airfoil case, but there is variation in the α_{eff} at which it occurs. At positive α_{eff}, there is a rapid rise in the slope of the C_L-α_{eff} curve at $\alpha_{eff} \approxeq 6°$ for the plunging airfoil cases compared to the stationary airfoil which only experiences open separation and whose C_L steadily increases up to $\alpha_{eff} \approxeq 8.5°$. Consequently, the plunging airfoil cases show a typical leading edge stall behavior with the peak C_L increasing and occurring at higher α_{eff} with increasing V_r, compared to the plateau-like stall behavior of the stationary airfoil case.

Identifying trends in the C_D results in 4.16b for Y/c = -0.5 is difficult due to the observed variation and higher uncertainty for plunging airfoil results compared to the stationary airfoil case. However, at low $|\alpha_{eff}|$ it is observed that the C_D on the plunging airfoil is typically lower than on the stationary airfoil and decreases with increasing V_r, which is similar to the results at the other two cross-stream locations. With respect to the overall shapes of the C_L- and C_D-α_{eff} results at K = 0.69 and $Re_c = 0.98 \times 10^4$, the load on the plunging airfoil at V_r = 0.07 and 0.14 are typically not

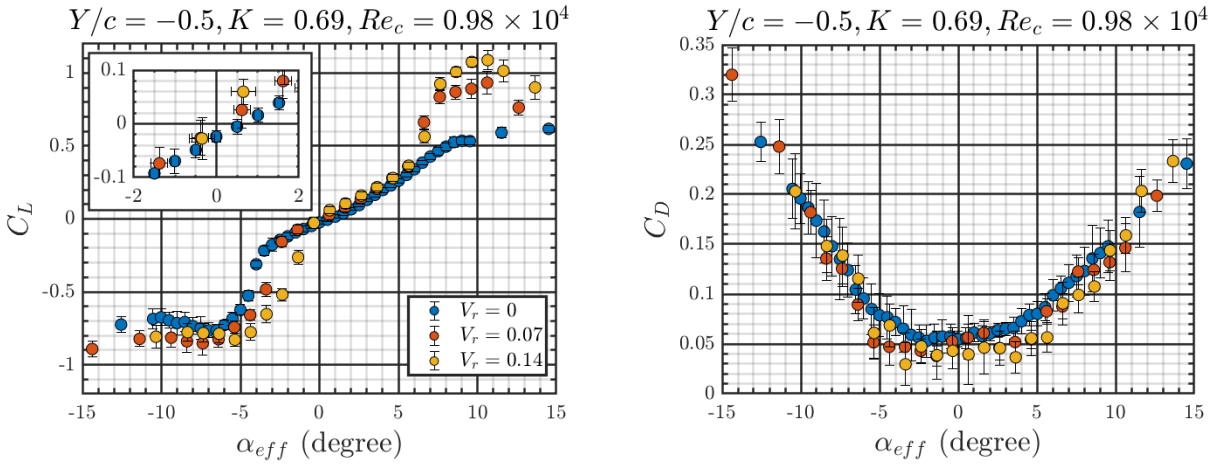

(a) (b)

Figure 4.16: **(a)** C_L- and **(b)** C_D-α_{eff} curves comparing the stationary (V_r = 0) and plunging ($V_r \neq 0$) airfoils in shear flow at Y/c = -0.5 where K = 0.69 and $Re_c = 0.98 \times 10^4$. The inset plot shows a zoomed-up view of the C_L-α_{eff} curve near zero α_{eff}, including uncertainty bars for α_{eff} that are otherwise smaller than the symbol size in the main plot.

well-approximated by the load on the stationary airfoil under the same flow conditions. As in the results at Y/c = 0, an important finding for the Y/c = -0.5 results is the observation of the $|C_L|$ on the plunging airfoil being greater than that on the stationary airfoil in association with the rapid rise in the slope of the $|C_L|$ curve at specific α_{eff}. However, the effect of the V_r on the slope change is strongest at K = 0.69 and $Re_c = 0.98 \times 10^4$, i.e., the highest K and lowest Re_c investigated, compared to the lower K, higher Re_c conditions at the other two cross-stream locations.

A study by Hamedani et al. (2019) performed similar measurements for a steadily plunging airfoil in shear in a wind tunnel reported at $Re_c = 7.5 \times 10^4$, K = 1.57 and V_r = 0.011-0.046. Their study found a qualitatively similar trend to this work, in which a noticeable change in the stall characteristics was observed for the plunging airfoil compared to its stationary counterpart, including a greater maximum C_L for the plunging airfoil. They observed stall characteristics at negative α_{eff} did not greatly differ between the stationary and the plunging airfoil, which is also observed for the two lower K, higher Re_c cases, but not the highest K, lowest Re_c case. Like the current results, they observed a limited α_{eff} range exists where the C_L on the plunging airfoil was approximated by its stationary counterpart. Though there are several differences between the

experimental setups, such as turbulence levels, airfoil aspect ratio, and shear profile, which are not considered, the qualitative similarities at different Re_c suggests a common physical phenomenon is occurring for the steadily plunging airfoil. Specifically, the shear flow in Hamedani et al. (2019) was unsteady and therefore they were unable to isolate shear effects from those of turbulence, whereas the steady shear flow in the current work allows for the isolation of shear effects.

Consider now the mean and RMS streamwise velocity measurements for the plunging airfoil compared to those for the stationary airfoil at the same α_{eff} and under the same flow conditions at $Y/c = 0$, where $K = 0.50$ and $Re_c = 1.35 \times 10^4$. The $\alpha_{eff} = 1.6$ is examined first to show the flow behavior which gives rise to the C_L- and C_D-α_{eff} results for the stationary airfoil and $V_r = 0.05$ and 0.1 cases at that angle. The mean and RMS streamwise velocity measurements are examined in Figs. 4.17 and 4.18, respectively, at $\alpha_{eff} = 1.6$ for $V_r = 0$, 0.05 and 0.1. Note from the C_L and C_D values referenced in the upper left corners in each subfigure of Figs. 4.17 and 4.18 that even at low α_{eff} the C_L on the plunging airfoil is slightly higher than on the stationary airfoil at $K = 0.50$ and $Re_c = 1.35 \times 10^4$, while the C_D results show close agreement. Here it is demonstrated how the subtle differences in the flow measurements give rise to these observations. The most obvious difference between the flows in Fig. 4.17 is the boundary layer separation location and subsequent extent of the reversed flow region. The separation point on the plunging airfoil is further downstream compared to the stationary airfoil and moves further downstream with increasing V_r. Consequently, the overall size of the reversed flow region is smaller for the plunging airfoil compared to the stationary airfoil and shrinks with increasing V_r. The RMS velocity results in 4.18 for the plunging airfoil show that the boundary layer maintains thin line of RMS velocity of $u'_{rms}/u_{eff} \approx$ 0.05-0.10 like for of the stationary airfoil.

The difference in the boundary layers between the stationary and plunging airfoils under these flow conditions is emphasized in Fig. 4.19, which shows the mean velocity profiles and boundary layer thicknesses δ/c at chordwise location $x^*/c \approx 0.88$ for $\alpha_{eff} = 1.6°$. The boundary layer thickness at $x^*/c \approx 0.88$ is observed to be about 10% and 30% smaller for the $V_r = 0.05$ and 0.1 plunging airfoils, respectively, compared to the stationary airfoil.

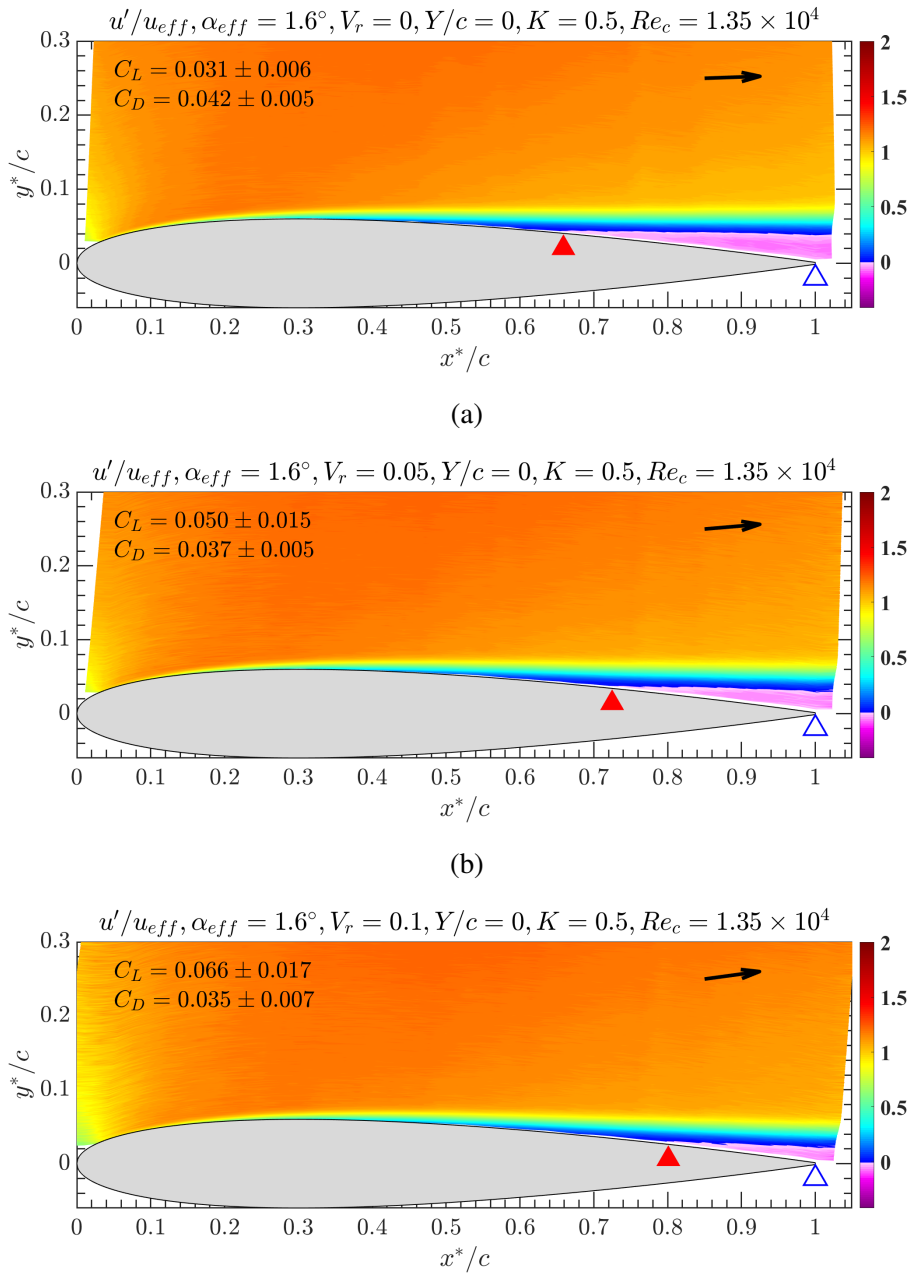

Figure 4.17: Mean streamwise velocity measurements by 1c-MTV for **(a)** the stationary airfoil ($V_r = 0$), and the plunging airfoil with **(b)** $V_r = 0.05$ and **(c)** $V_r = 0.1$ at $\alpha_{eff} = 1.6°$ in shear flow at $Y/c = 0$, $K = 0.50$ and $Re_c = 1.35 \times 10^4$. The black arrow in the upper right corner of each subfigure indicates the direction of the approach stream in the laboratory reference frame. The boundary layer separation location is denoted by the red triangle and the open separation at the trailing edge is denoted by the open blue triangle. Reversed flow is indicated by the shades of pink/purple.

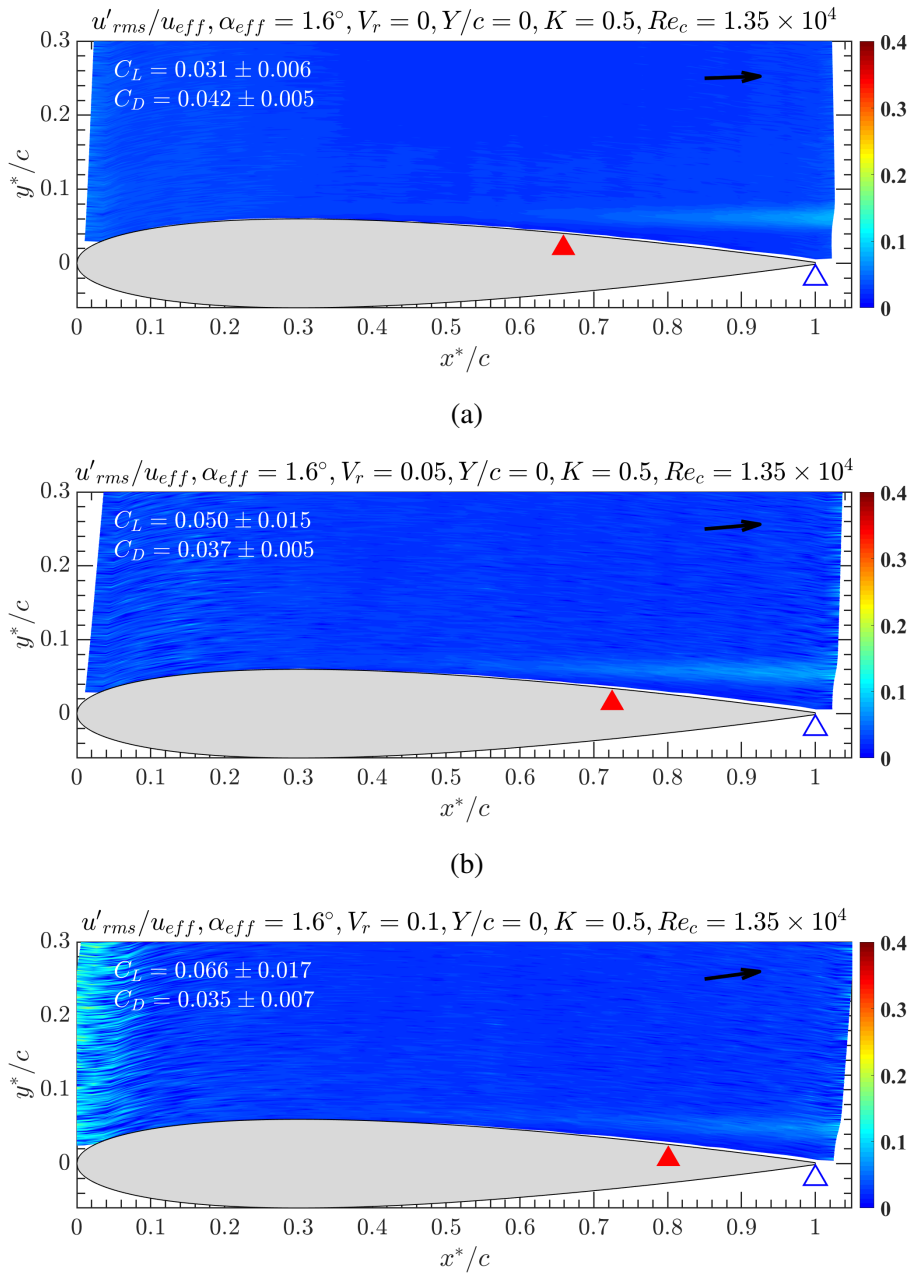

Figure 4.18: RMS streamwise velocity measurements by 1c-MTV for **(a)** the stationary airfoil ($V_r = 0$), and the plunging airfoil with **(b)** $V_r = 0.05$ and **(c)** $V_r = 0.1$ at $\alpha_{eff} = 1.6°$ in shear flow at $Y/c = 0$, $K = 0.50$ and $Re_c = 1.35 \times 10^4$. The black arrow in the upper right corner of each subfigure indicates the direction of the approach stream in the laboratory reference frame. The boundary layer separation location is denoted by the red triangle and the open separation at the trailing edge is denoted by the open blue triangle. Reversed flow is indicated by the shades of pink/purple.

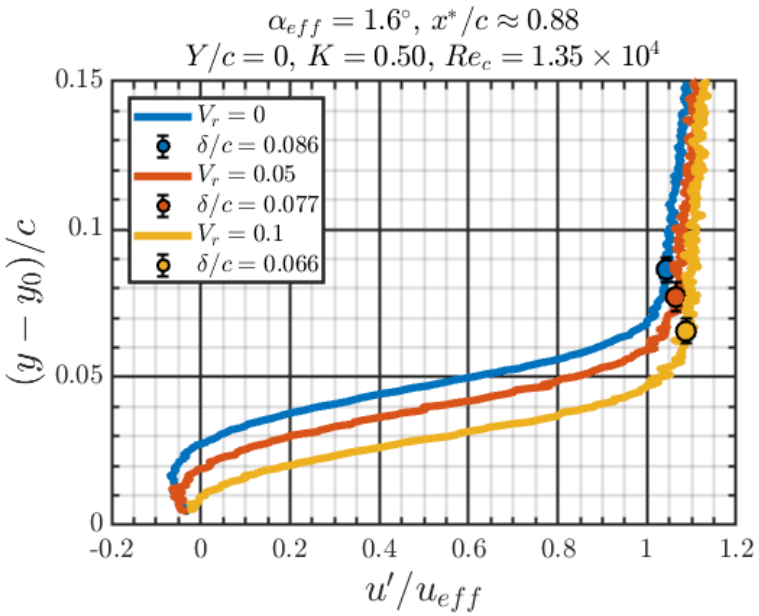

Figure 4.19: Mean velocity profiles (lines) and calculated boundary layer thickness δ/c (circles) for the stationary airfoil ($V_r = 0$), and the plunging airfoil with $V_r = 0.05$ and $V_r = 0.1$, at chordwise location $x^*/c \approx 0.88$ for $\alpha_{eff} = 1.6°$, in shear flow at $Y/c = 0$, $K = 0.50$ and $Re_c = 1.35 \times 10^4$.

Figures 4.20 and 4.21 show the mean and RMS streamwise velocity measurements, respectively, for the airfoil at a higher angle of $\alpha_{eff} = 5.6°$ for $V_r = 0$, 0.05 and 0.1 at $Y/c = 0$, where $K = 0.50$ and $Re_c = 1.35 \times 10^4$. Here it is demonstrated how the open separation on the stationary airfoil compared to the closed separation bubble on the plunging airfoil at the same α_{eff} and flow conditions gives a physical explanation for why the C_L is higher, and the C_D is lower, on the latter compared to the former. In Fig. 4.20, open separation is observed on the stationary airfoil with reversed flow covering approximately 66% of the airfoil surface. By contrast, a closed separation bubble is observed on the plunging airfoil at both $V_r = 0.05$ and 0.01. The boundary layer separation locations are similar for the two plunging airfoil cases, while the reattachment location of the higher V_r case is further downstream than the lower one.

The RMS velocity results in 4.21 show that there is a region of high RMS formed over the trailing edge for for the stationary airfoil. By contrast, for the plunging airfoil cases the high RMS region has moved over the airfoil surface as a result of the reattachment. The associated boundary layer thickness δ/c toward the trailing edge is observed to be smaller for the plunging airfoil than for the stationary airfoil. This difference in δ/c is highlighted in Fig. 4.22, which shows the mean

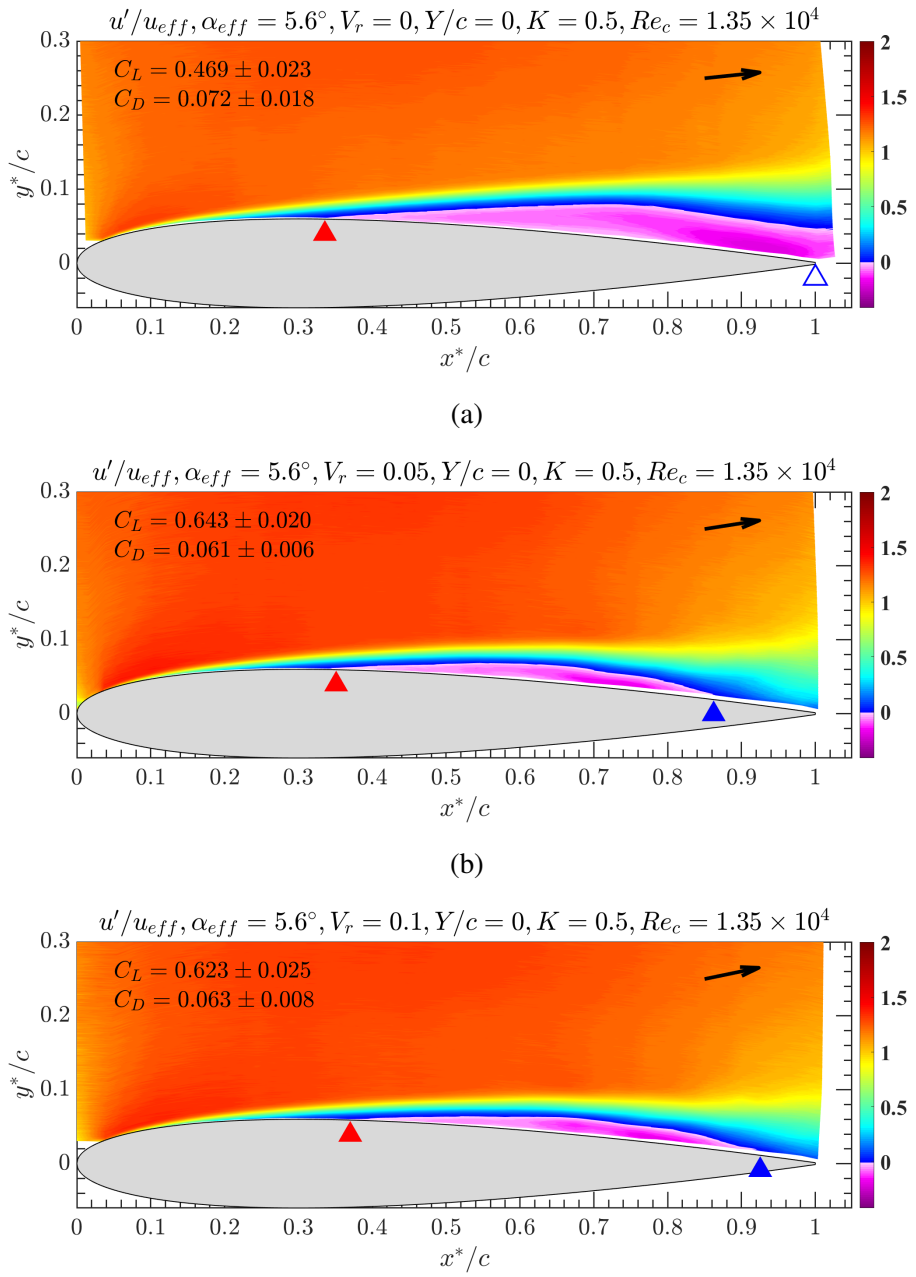

Figure 4.20: Mean streamwise velocity measurements by 1c-MTV for **(a)** the stationary airfoil ($V_r = 0$), and the plunging airfoil with **(b)** $V_r = 0.05$ and **(c)** $V_r = 0.1$ at $\alpha_{eff} = 5.6°$ in shear flow at $Y/c = 0$, $K = 0.50$ and $Re_c = 1.35 \times 10^4$. The black arrow in the upper right corner of each subfigure indicates the direction of the approach stream in the laboratory reference frame. The boundary layer separation location is denoted by the red triangle and the open separation at the trailing edge is denoted by the open blue triangle. Reversed flow is indicated by the shades of pink/purple.

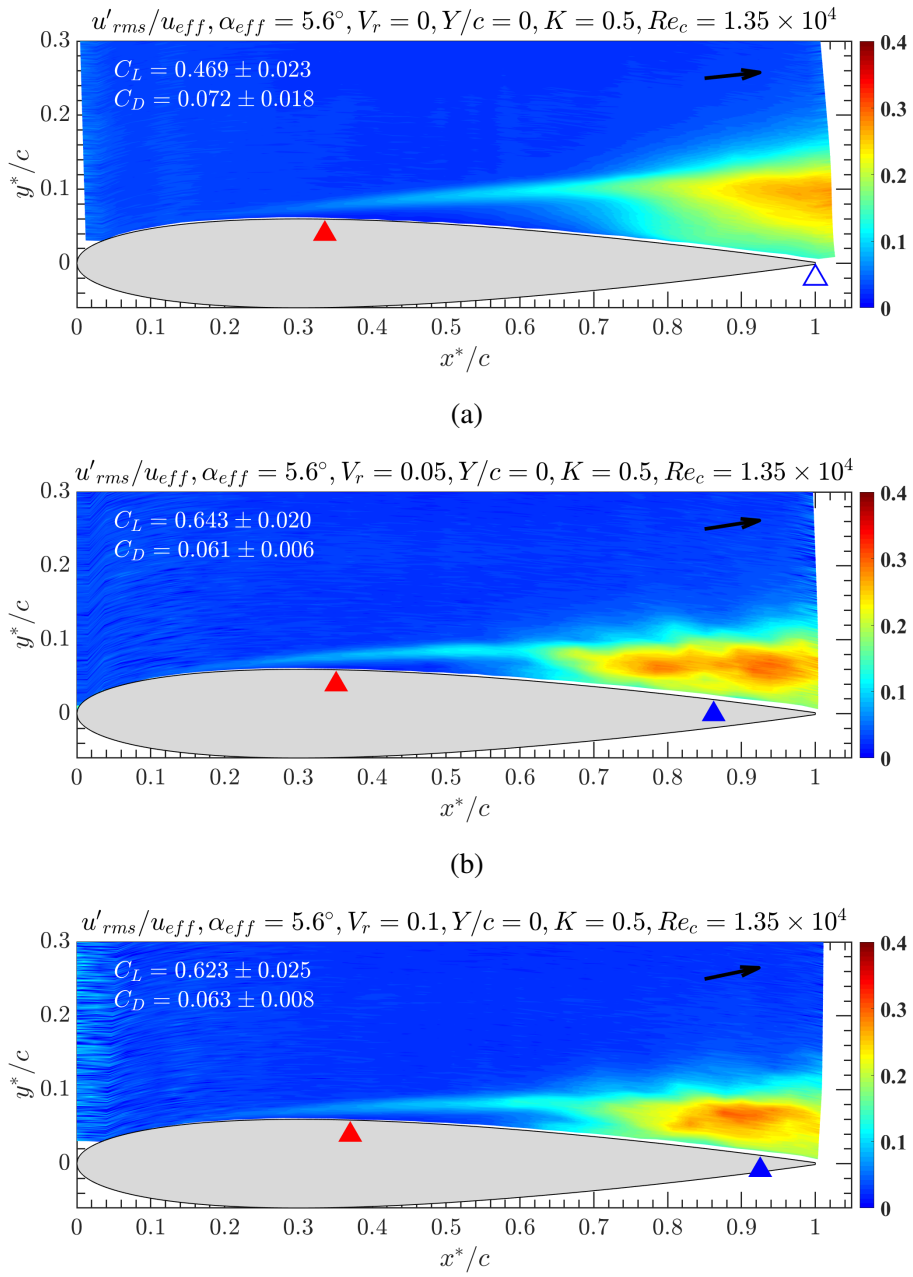

Figure 4.21: RMS streamwise velocity measurements by 1c-MTV for **(a)** the stationary airfoil ($V_r = 0$), and the plunging airfoil with **(b)** $V_r = 0.05$ and **(c)** $V_r = 0.1$ at $\alpha_{eff} = 5.6°$ in shear flow at $Y/c = 0$, $K = 0.50$ and $Re_c = 1.35 \times 10^4$. The black arrow in the upper right corner of each subfigure indicates the direction of the approach stream in the laboratory reference frame. The boundary layer separation location is denoted by the red triangle and the open separation at the trailing edge is denoted by the open blue triangle. Reversed flow is indicated by the shades of pink/purple.

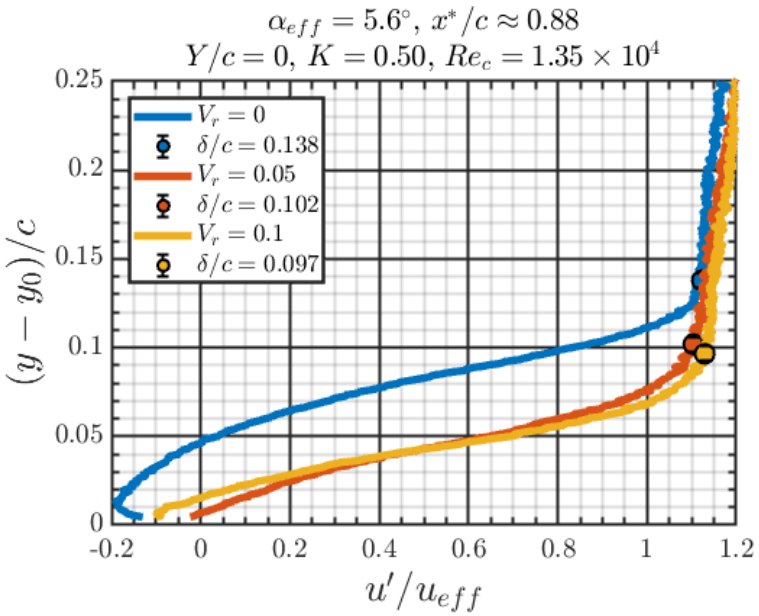

Figure 4.22: Mean velocity profiles (lines) and calculated boundary layer thickness δ/c (circles) for the stationary airfoil ($V_r = 0$), and the plunging airfoil with $V_r = 0.05$ and $V_r = 0.1$, at chordwise location $x^*/c \approx 0.88$ for $\alpha_{eff} = 5.6°$, in shear flow at $Y/c = 0$, $K = 0.50$ and $Re_c = 1.35 \times 10^4$.

velocity profiles and δ/c under these flow conditions at chordwise location $x^*/c \approx 0.88$ for α_{eff} = 5.6°. In Fig. 4.22, the δ/c is observed to be about 26% and 30% smaller for the V_r = 0.05 and 0.1 plunging airfoils, respectively, compared to the stationary airfoil.

Investigating the separation and reattachment locations over the range of α_{eff} for the flow measurements reinforces the physical description between the C_L- and C_D-α_{eff} curves of the stationary and plunging airfoils. Figure 4.23a shows the separation and reattachment locations, x_s and x_r, respectively, for V_r = 0, 0.05 and 0.1 at positive α_{eff} for the centerline shear flow conditions. Figure 4.23b shows the C_L measurements from Fig. 4.15a for a reduced range of α_{eff} which correlates to the separation and reattachment results in Fig. 4.23a. For $\alpha_{eff} \leq 3.6°$ in Fig. 4.23a, open separation is observed for the stationary airfoil and both plunging airfoil cases. Meanwhile, x_s for the plunging airfoils is consistently further downstream of that for the stationary airfoil, where x_s moves further downstream as V_r increases. As observed in Fig. 4.23b, the corresponding region of the C_L-α_{eff} curve is characterized by slightly higher C_L on the plunging airfoils compared to the stationary airfoil, which may be connected to the behavior of x_s. For $3.6° \leq \alpha_{eff} \leq 6.1°$, open separation is maintained on the stationary airfoil, whereas reattachment

occurs on the plunging airfoils. Note that this reattachment is associated with the rapid rise in the slope of the C_L-α_{eff} curve. Reattachment occurs on the stationary airfoil between $6.1^\circ \leq \alpha_{eff} \leq 7.6^\circ$, with the x_r approximately $0.22c$ further downstream compared to the plunging airfoil cases while x_s is similar among all cases. This is consistent with the 33-37% greater C_L on the plunging airfoils at $\alpha_{eff} = 7.6^\circ$ compared to the stationary airfoil.

4.3 Plunging Airfoil Load Approaching the Quasi-Steady Limit

It is apparent from the previous section that significant disagreement arises between the stationary and plunging airfoil load and flow results for the plunge speeds of V_a = 0.5 and 1.0 cm/s, especially at α_{eff} approaching and around stall. However, in the quasi-steady (QS) limit, the load on the plunging airfoil in shear is theoretically identical to the load on the stationary airfoil for all angles. To study how slowly the airfoil needs to plunge before the load it experiences may be well-approximated by that of the stationary airfoil over all α_{eff}, the airfoil is plunged at slower speeds approaching the quasi-steady (QS) limit, i.e., $V_r \rightarrow 0$, in the range $-15^\circ < \alpha_{eff} < 15^\circ$. Investigating the load on the plunging airfoil for $V_r \rightarrow 0$ over this α_{eff} range shows whether the airfoil motion across the shear is sufficiently slow for the flow dynamics to adapt to the changing position of the airfoil within the shear zone, and establishes that the expected QS result can be produced in the current experimental setup. The plunging airfoil cases in shear are studied here at as much as an order of magnitude slower than in the previous section. The resulting C_L- and C_D-α_{eff} curves are shown in Figs. 4.24-4.26 at each of the three primary cross-stream locations in comparison with the respective stationary airfoil results.

In Fig. 4.24 for Y/c = 0.5, where K = 0.40 and $Re_c = 1.65 \times 10^4$, excellent agreement is observed between the C_L-α_{eff} results for stationary and plunging airfoils. Compared to the results at higher V_r in the previous section, there is no longer disagreement in the peak C_L and stall behavior at either positive or negative angles. The corresponding C_D-α_{eff} results continue to show a slightly lower C_D on the plunging airfoil for V_r = 0.02, such as near zero α_{eff} or $\alpha_{eff} \approxeq -8^\circ$, whereas the C_D on the plunging airfoil for V_r = 0.01 generally agrees over the entire α_{eff}

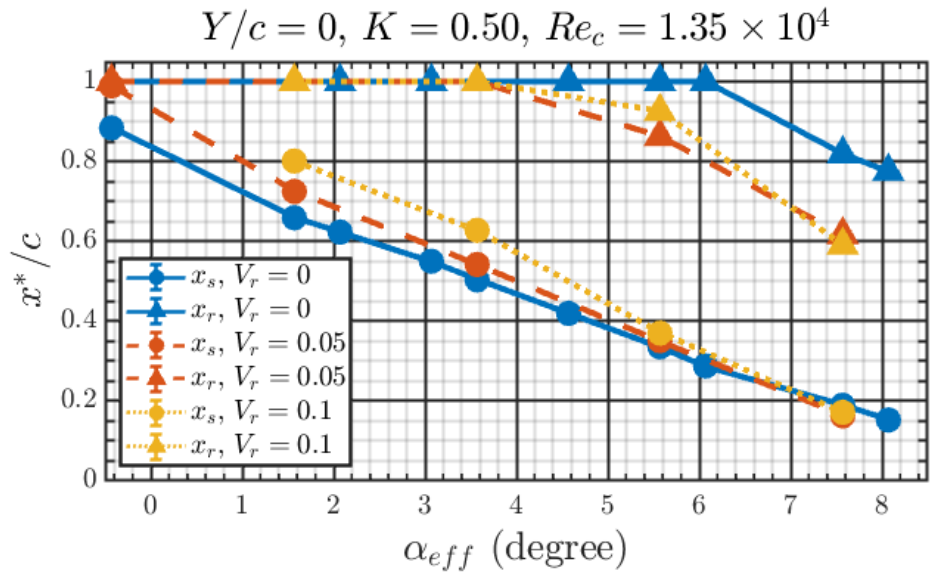

(a)

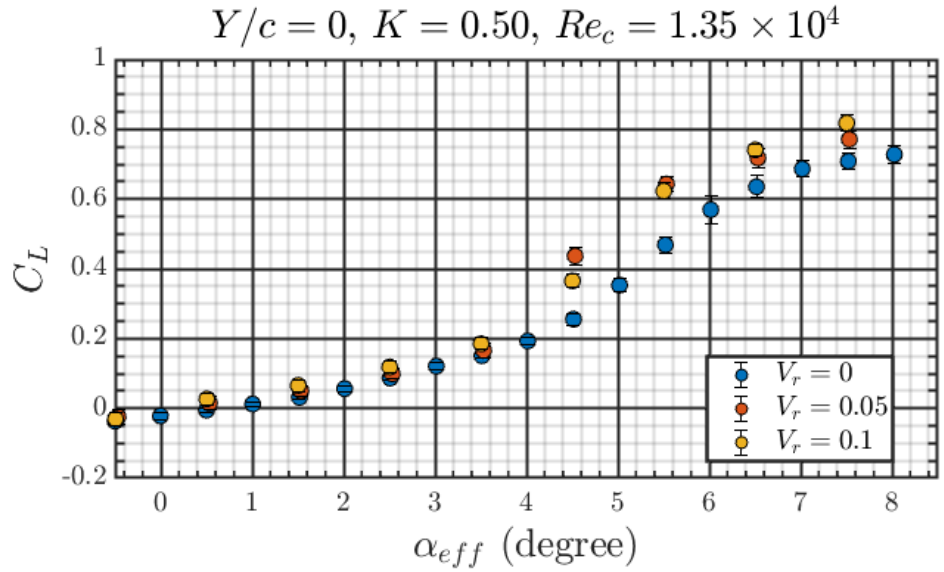

(b)

Figure 4.23: **(a)** The separation and reattachment locations, x_s and x_r, respectively, given by chordwise position x^*/c, and **(b)** lift coefficient C_L results for the stationary ($V_r = 0$) and plunging ($V_r \neq 0$) airfoils in shear flow at the centerline ($Y/c = 0$) where $K = 0.50$ and $Re_c = 1.35 \times 10^4$. In (a), circle symbols indicate x_s, triangle symbols indicate x_r, and open separation is indicated by $x^*/c = 1$ in the results for x_r.

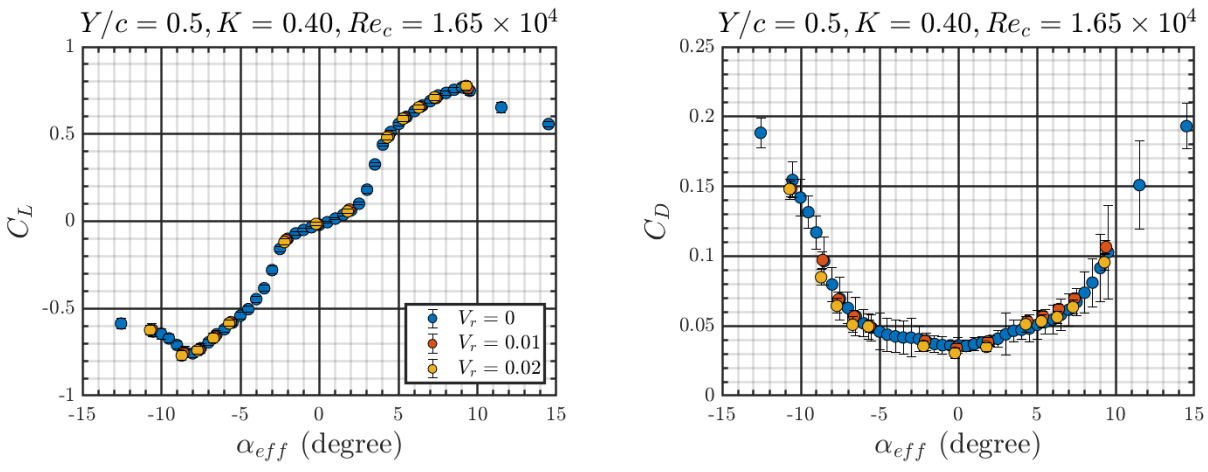

(a) (b)

Figure 4.24: **(a)** C_L- and **(b)** C_D-α_{eff} curves comparing the stationary ($V_r = 0$) and plunging ($V_r \neq 0$) airfoils in shear flow at $Y/c = 0$ where $K = 0.40$ and $Re_c = 1.65 \times 10^4$.

range studied to within the measurement uncertainty.

In Fig. 4.25 for $Y/c = 0$, where $K = 0.50$ and $Re_c = 1.35 \times 10^4$, disagreement is still observed between the C_L-α_{eff} results for stationary and $V_r = 0.02$ plunging airfoil, such as between $4° \lesssim \alpha_{eff} \lesssim 6.5°$ and near stall at both positive and negative angles. However, compared to the results at higher V_r in the previous section, the disagreement in the peak C_L and stall behavior at either positive or negative angles is significantly reduced. More importantly, the C_L on the plunging airfoil for $V_r = 0.01$ agrees with the stationary airfoil results over nearly the entire α_{eff} range investigated, noting the C_L is observed to be higher on the latter than the former only at $\alpha_{eff} \cong 5.5°$. This agreement includes the absence of variation in the α_{eff} at which the previously observed rapid rise in slope of the C_L-α_{eff} occurs for higher V_r. The corresponding C_D-α_{eff} results in Fig. 4.25b generally show close agreement in C_D on the plunging airfoil for $V_r = 0.01$ to within experimental error and similar variation to that observed for the results at $K = 0.40$ and $Re_c = 1.65 \times 10^4$.

In Fig. 4.26 for $Y/c = -0.5$, where $K = 0.69$ and $Re_c = 0.98 \times 10^4$, the $|C_L|$ on both the $V_r = 0.01$ and 0.03 plunging airfoils at negative α_{eff} stall are 11% and 16% greater, respectively, than for the stationary airfoil. At $7° \lesssim \alpha_{eff} \lesssim 10°$, noting no traditional leading edge stall behavior is observed, the C_L on the plunging airfoil for $V_r = 0.03$ is also slightly greater than for the stationary

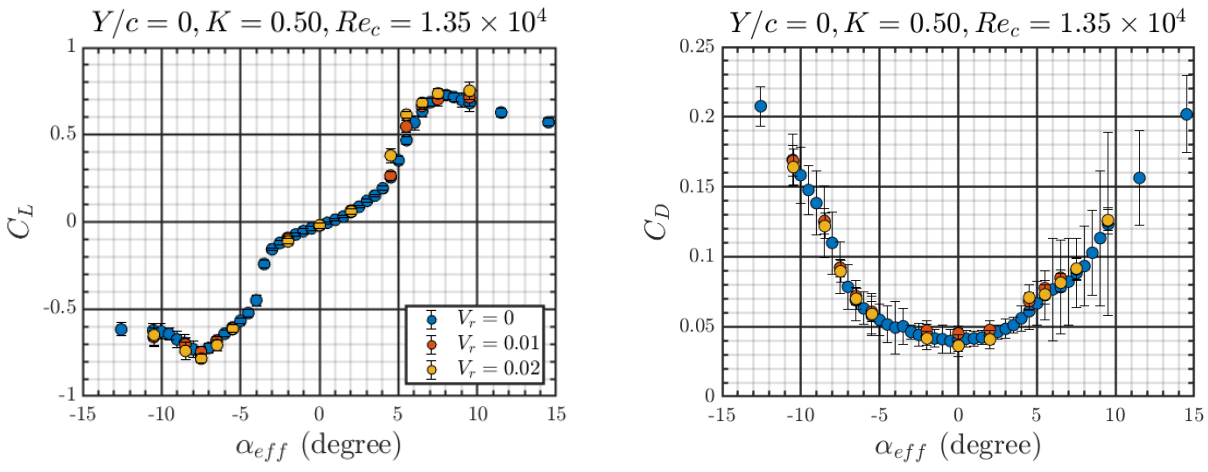

(a) (b)

Figure 4.25: **(a)** C_L- and **(b)** C_D-α_{eff} curves comparing the stationary ($V_r = 0$) and plunging ($V_r \neq 0$) airfoils in shear flow at $Y/c = 0$ where $K = 0.50$ and $Re_c = 1.35 \times 10^4$.

airfoil, while the C_L on the plunging airfoil $V_r = 0.01$ is nearly identical to that on stationary airfoil. Like for the low V_r cases at $K = 0.50$ and $Re_c = 1.35 \times 10^4$, the agreement at $K = 0.69$ and $Re_c = 0.98 \times 10^4$ between the C_L on the stationary and $V_r = 0.01$ plunging airfoils includes the absence of variation in the α_{eff} at which the previously observed rapid rise in slope of the C_L-α_{eff} occurs for higher V_r. While the C_D results for the plunging airfoil cases in Fig. 4.26b tend to follow the general shape of the stationary airfoil C_D-α_{eff} curve, it is difficult to identify any single trend due to amount of variation observed. However, the variation observed is of similar order to that observed at both of the lower K, higher Re_c conditions. Compared to the variation observed in the results at higher V_r, the current results for low V_r show much closer C_D agreement with the stationary airfoil results. Overall, at $K = 0.69$ and $Re_c = 0.98 \times 10^4$ it is concluded that the airfoil plunging with $V_r = 0.01$ is effectively quasi-steady and results in a close approximation by the stationary airfoil result except at negative angle of attack stall.

Finally, to emphasize the approach to QS behavior of the plunging airfoil C_L results, the difference in C_L is calculated between plunging airfoil at each V_r investigated and their stationary airfoil counterpart. The α_{eff} for the stationary airfoil results are found via interpolation since they have a higher α_{eff} resolution compared to that of the plunging airfoil results. Given the lift coefficient on the plunging airfoil $C_{L,p}$ and that on the stationary airfoil $C_{L,s}$, a metric for the

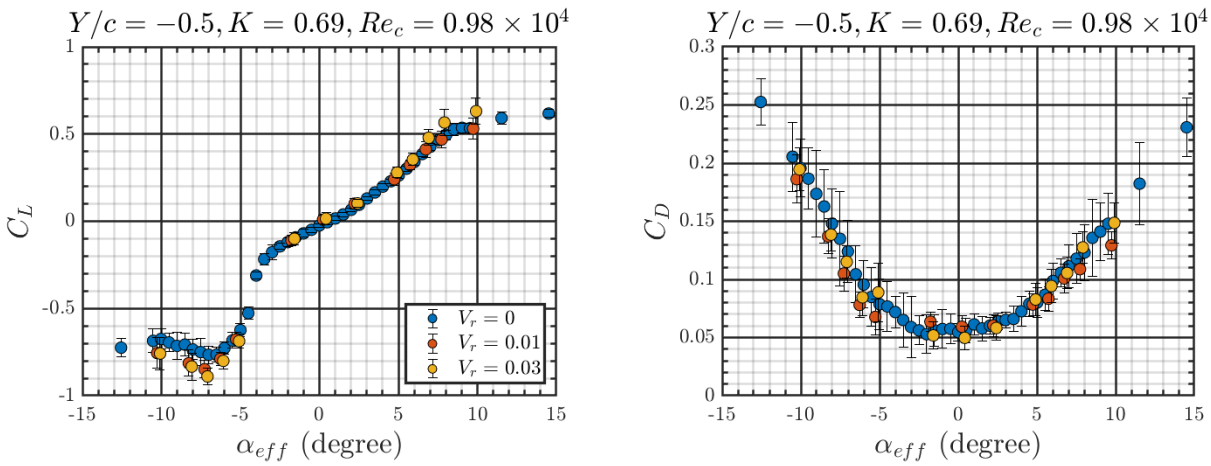

(a) (b)

Figure 4.26: **(a)** C_L- and **(b)** C_D-α_{eff} curves comparing the stationary ($V_r = 0$) and plunging ($V_r \neq 0$) airfoils in shear flow at Y/c = -0.5 where K = 0.69 and $Re_c = 0.98 \times 10^4$.

residual is estimated by $\sigma = \sqrt{\Sigma(C_{L,p} - C_{L,s})^2/N}$, where N is the number of angles used. This metric σ is an estimate of how well the overall C_L-α_{eff} curves agree between the stationary and plunging airfoil results at each V_r. The computed σ results are shown in Fig. 4.27 as a function of V_r for the freestream conditions at each of the three cross-stream positions. Here, the estimated V_r has been extended out to three decimal places to more accurately show the trends at low V_r. From Fig. 4.27, an overwhelming trend becomes clear that σ tends toward zero as V_r approaches zero. It is typically observed at common V_r between the three freestream conditions that the residual is greater on the plunging airfoil as K increases and Re_c decreases. For each of the three freestream conditions studied, the load on the plunging airfoil in shear is overall closely approximated by that on the stationary airfoil under the same freestream conditions only when $V_r \lesssim 1\%$.

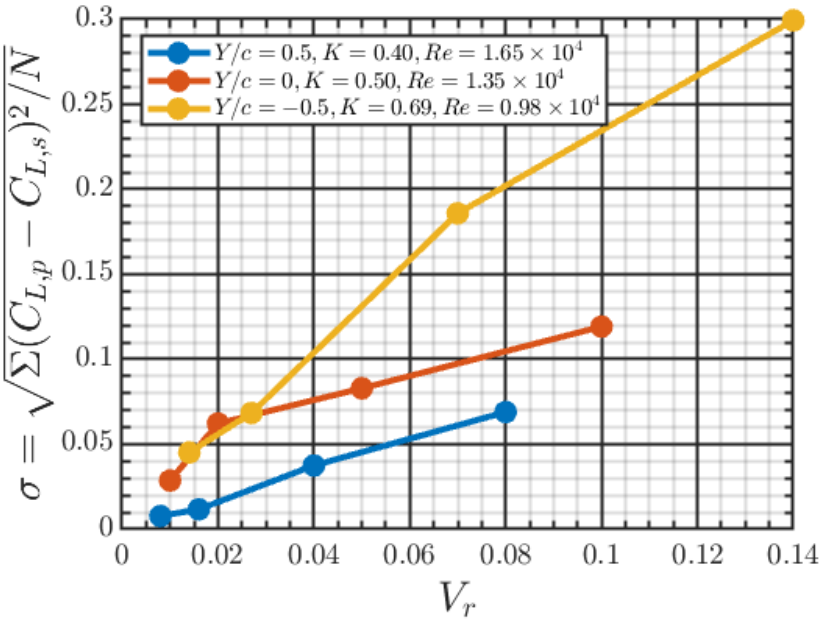

Figure 4.27: Estimated residual metric $\sigma = \sqrt{\Sigma(C_{L,p} - C_{L,s})^2/N}$ as a function of V_r for the flow conditions at each of the three cross-stream positions, where $C_{L,p}$ is the lift coefficient on the plunging airfoil, $C_{L,s}$ is the lift coefficient on the stationary airfoil, and N is the number of angles used. The V_r values are estimated to three decimal places to more accurately show the trends at low V_r.

CHAPTER 5

CONCLUSIONS

The current study experimentally investigated the steadily plunging NACA 0012 airfoil from the high- to low-speed side of a canonical uniform-shear approach flow with a positive velocity gradient in a water tunnel. Unlike the uniform approach stream commonly considered in unsteady aerodynamics studies, the shear approach stream considered in this work is often a more realistic scenario, such as during takeoff and landing. In uniform flow, the load on the steadily plunging airfoil in the moving airfoil reference frame is the same as on the stationary airfoil in the laboratory reference frame. The aim of this work was to determine if the same relationship can be applied to the steadily plunging airfoil in shear. The current study investigated this question by using a load cell to directly measure the aerodynamic load on the steadily plunging airfoil in shear by varying the ratio of the plunge speed to the local freestream speed (V_r). Single-component molecular tagging velocimetry (1c-MTV) was used to measure the streamwise velocity component of the flow over the plunging airfoil. A shaped honeycomb technique was used to generate the canonical freestream shear in the test section characterized by a linearly varying velocity shear zone bounded by regions of high- and low-speed uniform flow. The airfoil traversed from the high- to low-speed side of the flow utilizing a unique motion profile designed to maintain a constant effective angle of attack during the linear acceleration phase, which allowed the airfoil to plunge at higher speeds without introducing significant flow transients.

The plunging airfoil was first investigated in uniform flow to ensure that the unique experimental setup could reproduce the well-known relationship between the stationary and steadily plunging airfoils. In doing so, it is also determined there are no significant blockage, confinement or other artifacts resulting from the airfoil traversing over a large fraction of the test section's width. It was observed that the load and flow on the steadily plunging airfoil in uniform flow agreed well with the load on the stationary airfoil for the same effective angles of attack and flow conditions at specific cross-stream locations. While the unique motion profile enabled higher plunge speeds to

be investigated, the maximum plunge speed was ultimately limited to $V_r \leq 0.1$ due the presence of flow transients in the initial acceleration phase that persisted too far into the airfoil trajectory. The basic load and flow features for the airfoil in uniform flow were characterized at the same chords Reynolds numbers (Re_c) defined in the shear flow at the three primary cross-stream locations of interest; in the range Re_c = 0.98-1.65$\times 10^4$. It was observed that the lift coefficient versus effective angle of attack (C_L-α_{eff}) curve exhibited a multi-region behavior, with each region characterized by a different slope that gave the curve a highly nonlinear shape overall, as observed in literature. It was further observed from connecting the load and flow measurements that the slope of the C_L-α_{eff} curve sharply increased in relation to the flow over the airfoil switching from an open separation to a closed separation bubble on the airfoil suction surface. For $Re_c = 1.35 \times 10^4$ and $Re_c = 1.65 \times 10^4$, the angle of attack at which the slope change occurred was found to increase with decreasing Reynolds number. However, at $Re_c = 0.98 \times 10^4$, only open separation was observed which correlated with a steady increase in C_L.

The basic effect of shear on the stationary airfoil at the three cross-stream locations was studied to provide baseline measurements for the plunging airfoil in shear. For the range of dimensionless shear rates K = 0.40-0.69 and chord Reynolds numbers Re_c = 0.98-1.65 $\times 10^4$ in this study, it was observed that the airfoil in shear flow shows negative lift at zero angle of attack compared to zero lift in uniform flow, which is an effect opposite of inviscid theory but consistent with recent computational and experimental literature from our group. Shear was shown to generate asymmetry in the lift and drag coefficient curves, especially at angles of attack around stall, with greater asymmetry observed as K increased and Re_c simultaneously decreased, noting that these two parameters are inextricably linked by nature of the varying velocity of the shear zone. The C_L-α_{eff} curves for the two higher Re_c, lower K cases exhibit a similar multi-region behavior that is observed in uniform flow, which is correlated from the 1c-MTV measurements to the airfoil switching from open separation to a closed separation bubble. However, at positive angles, the flow transition from open separation to a closed separation bubble occurs at higher angle of attack in shear compared to in uniform flow. For the highest K, lowest Re_c case, only open separation

is observed at positive angles, like the corresponding results in uniform flow, but the separation location on the airfoil in shear was consistently further downstream than for the airfoil in uniform flow.

For the ranges of K = 0.40-0.69 and Re_c = 0.98-1.65$\times 10^4$ here, it is observed that the plunging airfoil in shear exhibits fundamental differences in the load it experiences compared to its stationary airfoil counterpart when accounting for the effective angle of attack in the reference frame of the airfoil. The slope of the C_L-α_{eff} curve on the former begins to rapidly increase at lower α_{eff} than for the latter, which is found to be a result of the flow reattaching at a lower α_{eff} on the plunging airfoil than for the stationary airfoil. It is also observed that the boundary layer separation point tends to be further downstream on the plunging airfoil at low α_{eff}, with the location moving farther downstream with increasing V_r. Specifically near stall, it is generally observed that the magnitude of the C_L on the plunging airfoil is greater than that for the stationary airfoil. Corresponding flow measurements indicate that even though the separation locations on the plunging and stationary airfoils are similar at angles near stall, the reattachment point is further upstream for the plunging airfoil, which gives rise to the higher C_L observed at the same α_{eff}. To approximate the C_L on the plunging airfoil in shear over a large range of α_{eff} (-15° < α_{eff} < 15° in this study) using the stationary airfoil result under the same flow conditions, it is found that the airfoil typically needs to plunge as slowly as 1% of the local freestream speed. For the airfoil plunging with $V_r \cong 0.01$, the differences in the C_L curves observed at higher V_r, such as the change in the slope of the curve or the higher C_L on the plunging airfoil, typically disappear and allow for a large range of α_{eff} over which the approximation from the C_L on the stationary airfoil can be made.

APPENDICES

APPENDIX A

FREESTREAM FLOW CHARACTERIZATION

In this Appendix, the single component molecular tagging velocimetry (1c-MTV) implementation used to characterize the freestream shear velocity profile generated by the variable-length honeycomb is described. Refer to Chapter 2 for the details about the overall 1c-MTV technique. Two pco.pixelfly cameras are mounted side by side beneath the water tunnel. The pco.pixelfly is a 14 bit charge-coupled device (CCD) with a 1392 $\times$ 1024 pixel resolution (cross-stream direction $\times$ streamwise direction). Two cameras are used to minimize acquisition time. Each camera is fitted with a Nikon Nikkor 35 mm f/1.2 lens and pointed upwards into the test section. The resulting fields of view (FOV) at full frame are 11.87 $\times$ 15.90 cm with a resolution of 114.15 μm/pixel. In the cross-stream direction, the pixels are "binned" to a resolution of 696 pixels (228.30 μm/pixel) to increase the signal. The cameras can be positioned independently in the streamwise, cross-stream and vertical directions by way of the traverse system to which they are affixed. The two cameras are positioned on the traverse system so that there is approximately 7% overlap of their FOVs. The location of the flow measurements is far enough upstream of the airfoil such that the presence of the airfoil does not influence the flow and far enough downstream of the shear generation device that the flow is sufficiently developed. The total region investigated is -2.2 $\leq Y/c \leq$ 2.2 relative to the centerline Y/c = 0 to encompass not only the moving airfoil range, but to also measure the uniform flow regions of the three-segment profile. Characterizing the freestream shear velocity profile into both the high- and low-speed uniform streams is achieved using a total of four FOVs, as shown in by the schematic of the overall 1c-MTV implementation in Fig. A.1. The two cameras, respectively denoted by C1 and C2 in Fig. A.1 each acquire one frame at each position of the traverse system. The two positions of the traverse are prescribed so that there is approximately 51% overlap around the centerline.

For sufficiently steady flows, it is possible to record independent time series of reference "undelayed" images and subsequent "delayed" images, provided the initial line tagging pattern

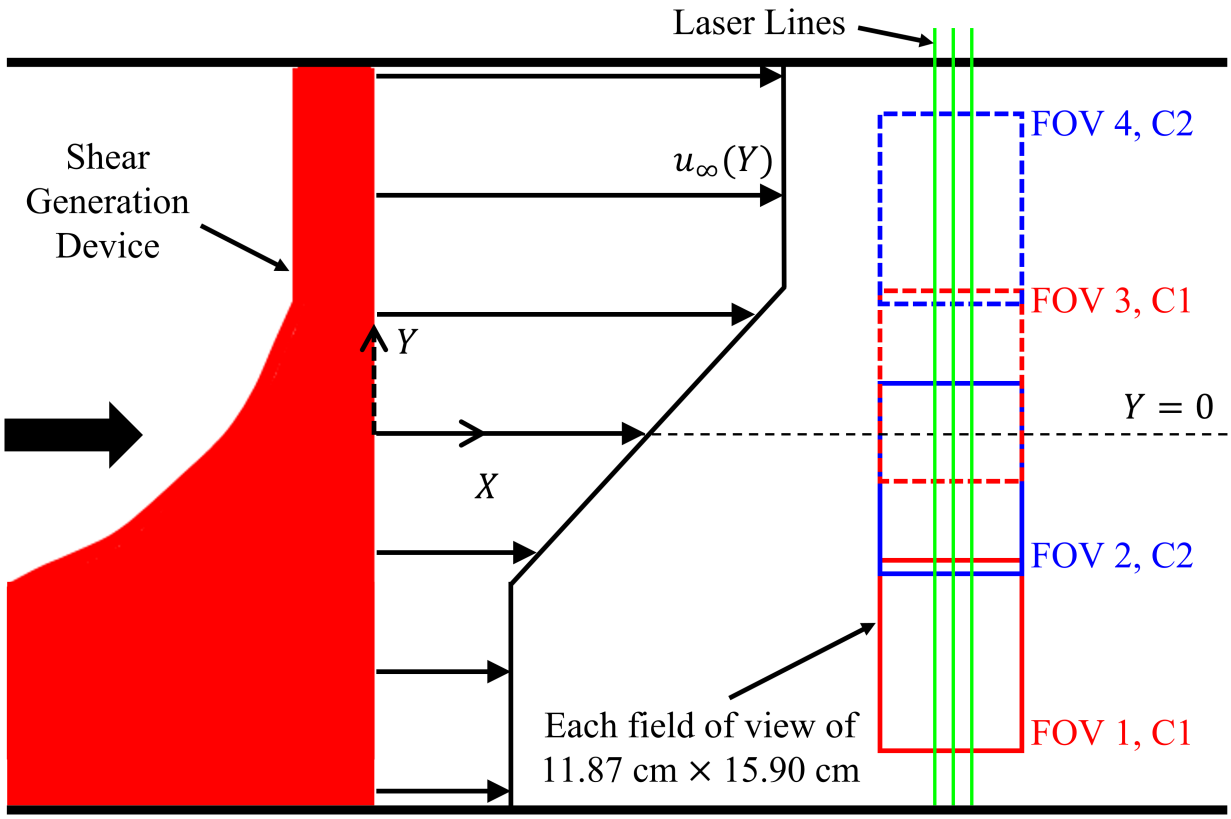

Figure A.1: Schematic of the 1c-MTV setup for characterizing the freestream shear flow. Two adjacent pco.pixelfly cameras capture four fields of view across the test section width.

remains spatially invariant throughout the experiment Koochesfahani & Nocera (2007). The time series of instantaneous undelayed images is averaged to a single image, against which the time series of instantaneous delayed images are correlated. This implementation of 1c-MTV is used for characterizing the freestream, based on previous TMUAL experience. The image sequences are captured by triggering the cameras with transistor-transistor-logic (TTL) pulses generated by a digital delay generator (Stanford Research Systems model DG535 Digital Delay/Pulse Generator), as shown in Fig. A.2. To trigger both cameras at the same time, the signal from the digital delay generator (DDG) from output AB is simply split to both cameras. The first sequence, which is made up of 1600 instantaneous images, is acquired at 11 fps 1 μs after the laser pulse which is triggered from output CD of the DDG. The second sequence, which is made up of 2400 images, is acquired separately at 11 fps with the prescribed delay time Δt in the range 7-8 ms relative to the timing of the first sequence. In all cases, the exposure time is held constant at 1 ms.

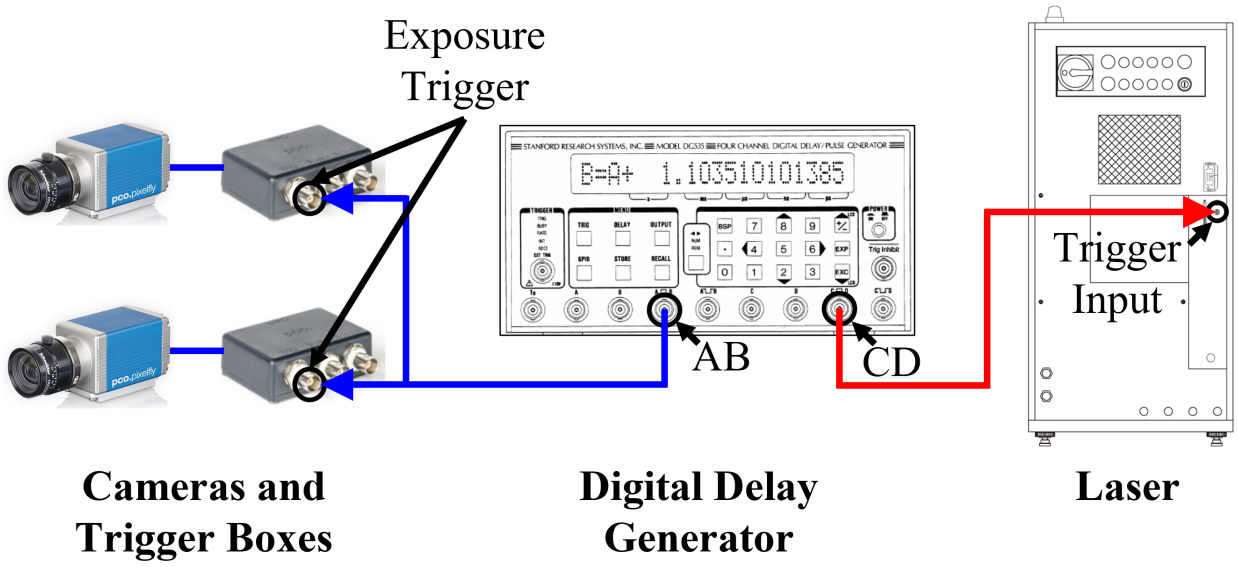

Figure A.2: Laser (red lines) and camera (blue lines) triggering diagram for the pco.pixelfly camera. This diagram is shown for the case of the digital delay generator (DDG) being triggered internally to acquire sequences of images of the freestream flow.

APPENDIX B

LOAD CELL CALIBRATION FOR CROSS-STREAM POSITION AND ANGLE OF ATTACK

The ATI Mini40 load cell used in this work is sensitive to the weight distribution of the airfoil, which varies with the cross-stream position (Y/c) and geometric angle of attack (α). Though great care is taken in the alignment or the airfoil, small changes in the elevation of the tunnel floor, weight of the servo motion system, stiffness of the load cell and other factors can contribute to artifacts in the load cell output. In the stationary airfoil measurements, this is easily accounted for by performing the flow-off measurements at the start of the procedure to zero the load cell, as described in Chapter 2. However, for plunging airfoil experiments, the load measurement procedure does not permit a measurement to zero the load cell for all positions throughout the plunge, which vary between -1.5 $\leq Y/c \leq$ 1.5. To address this concern, the load cell is calibrated based on cross-stream position and angle of attack on the stationary airfoil using the following procedure.

With the flow off, the airfoil begins with a prescribed α at Y/c = 1.5 where the load is recorded for 30 s. The airfoil then moves to the next position, waits 30 s to allow the airfoil to reach steady state, and records the load for 30 s. This procedure is repeated every $0.25c$ between -1.5 $\leq Y/c \leq$ 1.5 for a single α. There are 13 positions recorded in total for a single angle of attack such that the total measurement time is short enough to neglect the drift in the sensor's bias. This procedure is repeated for angles between -20° $\leq \alpha \leq$ 20° with 1° resolution, which encompasses the α range used in this study. The load measurements at each position are ensemble averaged and referenced to the calibration at the centerline since that is where the flow-off measurement to zero the load cell in the plunging airfoil load measurement procedure is referenced. As a result, a 2D calibration matrix is produced which allows for the static, no-flow load to be interpolated for each Y/c and α combination within the experimental range. Consequently, the calibration is applied to the plunging airfoil phase averaged load measurements at every position along the trajectory, prior to making them dimensionless and transforming the reference frames.

The 2D calibration matrices for the force measured in the streamwise and cross-stream directions, F_x and F_y, respectively, are shown for example in Fig. B.1. Along the $Y/c = 0$ location, $F_x = 0$ and $F_y = 0$ since it is the reference location for each α. The calibration data for F_x in Fig. B.1a shows that F_x is typically more sensitive to cross-stream position than angle of attack, except for at large negative angles. The load offset from the centerline condition peaks at about 0.03 N in either direction, which equates to a substantial force coefficient of about 0.08 (over twice the minimum C_D at zero α at the centerline flow conditions for the NACA 0012 airfoil in this work). The calibration data for F_y in Fig. B.1b shows that F_y is typically sensitive with the combination of high angle of attack and cross-stream position far from the centerline, peaking at about 0.03 N, but less sensitive overall at low α. Based on the above discussion, the large contribution to the load offsets based on cross-stream position and geometric angle of attack clearly shows that it must be accounted for in the current work to obtain the load history on the plunging airfoil as it moves across the test section.

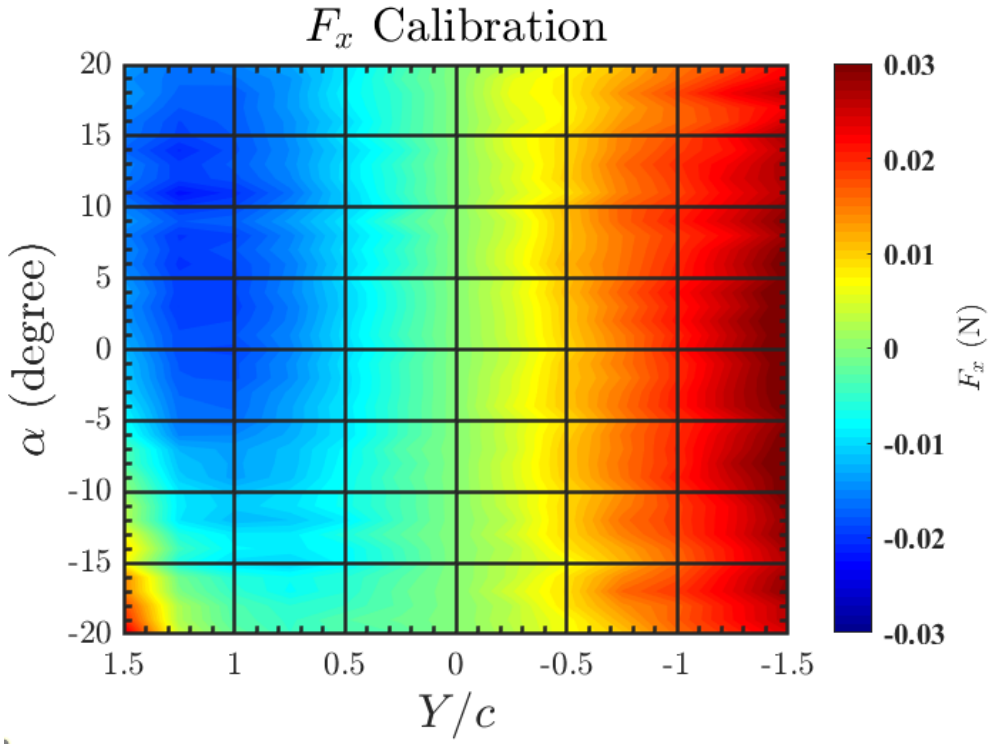

(a)

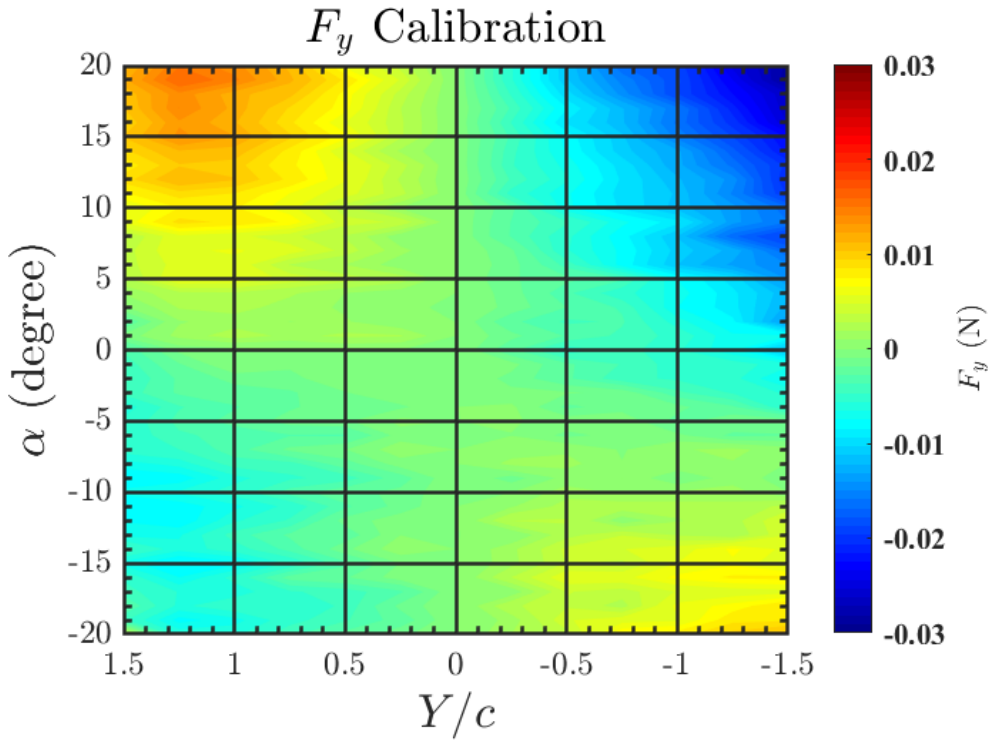

(b)

Figure B.1: Contour plots of the calibrated force in the (a) x-direction (F_x) and (b) y-direction (F_y) of the load cell as functions of Y/c and α. The data in these plots are used to perform a 2D interpolation which is subtracted from the plunging airfoil load measurements at a given instant in time based on Y/c and α.

APPENDIX C

AERODYNAMIC EFFECTS BASED ON CROSS-STREAM POSITION

Performing aerodynamic experiments in a bounded flow, such as in the water tunnel test section in the current work, results in various effects that must be considered, compared to in an unbounded flow or flow bounded by one plane boundary typical for flight vehicles. Furthermore, the current work considers the plunging airfoil which traverses across the central 59% of the test section width, i.e., with varying proximity to the boundaries. To address the aerodynamic effects due to the presence of the test section boundaries, the variation of the local zero-lift angle of attack ($\alpha_{L=0}$) and the C_L and C_D at zero α with cross-stream position Y/c are characterized. Characterizing the local $\alpha_{L=0}$ as a function of Y/c is intended to account for the effect of streamline curvature caused by the streamlines being forced to be tangent to the test section walls, while characterizing the variation in C_L and C_D with Y/c is intended to account for the blockage effects based on the presence of the model blocking the flow.

To evaluate the variation in $\alpha_{L=0}$ with Y/c, load measurements are performed on the stationary airfoil at several Y/c positions in the range -1.5 $\leq Y/c \leq$ 1.5. The measurements are performed for several angles of attack around zero degrees, where the $\alpha_{L=0}$ at the centerline in uniform flow is used as the reference. The $\alpha_{L=0}$ at each Y/c is determined by the α where the measured C_L-α curve crosses zero and is found to within an uncertainty $\pm 0.1^\circ$. The results of these measurements are highlighted in Fig. C.1 which shows the variation in $\alpha_{L=0}$ for the stationary airfoil in both uniform flow and shear. The uniform flow results in Fig. C.1 show a clear trend in which the $\alpha_{L=0}$ increases as the airfoil moves in the positive-Y/c direction and decreases in the negative-Y/c direction, relative to the centerline. It is observed that the variation in $|\alpha_{L=0}|$ is less than 0.25° up to the extremes of $|Y/c|$ = 1.5. However, between -0.5 $\leq Y/c \leq$ 0.5, where the current work focuses, the variation in $|\alpha_{L=0}|$ is less than 0.06°; less than the uncertainty of $\pm 0.1^\circ$. Consequently, the shift in the local $\alpha_{L=0}$ is deemed negligible for the purpose of comparing the time- or phase-averaged load measurements in uniform or shear flow at each of the three cross-stream positions investigated.

The shear flow results in Fig. C.1 show a unique variation in $\alpha_{L=0}$ with Y/c but are provided only for information since the effects of both Re_c and K are present and inseparable. The flow parameters at each Y/c position in shear are provided in Table C.1 for reference.

To evaluate the variation in C_L and C_D with Y/c, the C_L and C_D values at $\alpha = 0^\circ$ are extracted from the above measurements. Here zero α is identical at each position based on the zero α at the centerline. The C_L and C_D at $\alpha = 0^\circ$ are shown in Fig. C.2, relative to the values at $Y/c = 0$. It is observed from Fig. C.2 that C_L decreases as Y/c increases and vice versa. These results are consistent with the shift in $\alpha_{L=0}$ in C.1; e.g., the shift in $\alpha_{L=0}$ toward positive angles at positive Y/c relative to the centerline means the geometric zero α is at negative angle of attack relative to the flow, which produces negative lift. The C_D results in Fig. C.2 show no clear trend across the width of the test section. The magnitude of the variations in C_L and C_D at zero α over the range -1.5 $\leq Y/c \leq$ 1.5 are less than 0.0062 and 0.0033, respectively, compared to the plunging airfoil measurement uncertainty in C_L of ±0.06 and C_D of ±0.02. As such, the variation in C_L and C_D over the primary measurement range of -0.5 $\leq Y/c \leq$ 0.5 is neglected for the purpose of this study.

Y/c	Re_c	K	u_0 (cm/s)
1.50	17300	-	14.1
1.00	17900	-	14.5
0.67	16400	0.38	13.3
0.33	14500	0.43	11.7
0.00	12600	0.50	10.1
-0.33	10400	0.59	8.4
-0.67	7900	0.78	6.4
-1.00	4700	-	3.8
-1.50	5900	-	4.8

Table C.1: Freestream flow parameters in shear flow for the cross-stream positions discussed in this appendix. Dimensionless shear rate (K) data at the edge or outside of the shear layer are given by "-" since K is not clearly defined.

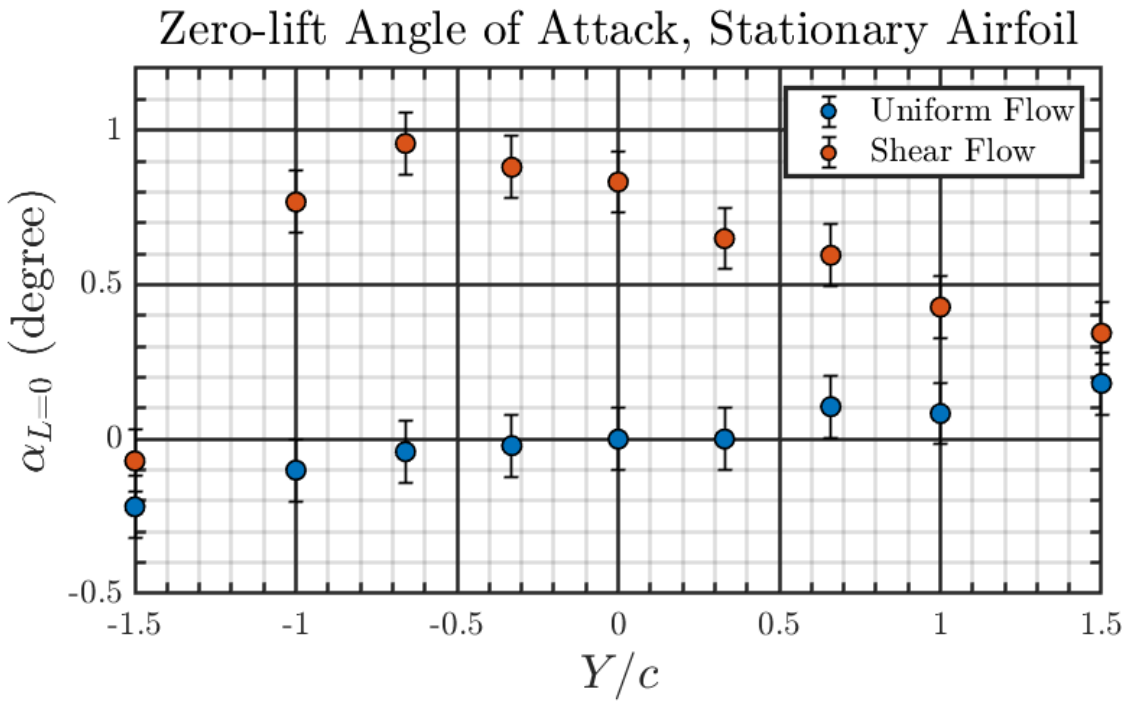

Figure C.1: Variation of the zero-lift angle of attack ($\alpha_{L=0}$) with cross-stream position Y/c in uniform flow ($Re_c = 1.24 \times 10^4$) and shear. Zero α is referenced at $Y/c = 0$ in uniform flow. Shear flow parameters are given in Table C.1.

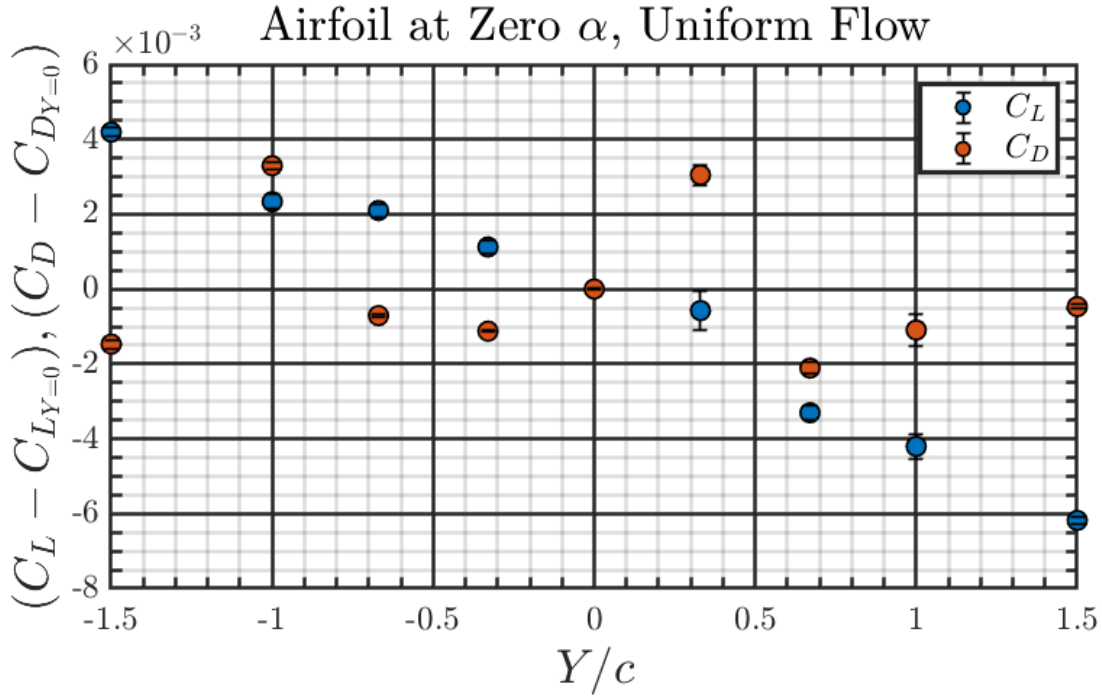

Figure C.2: Variation of C_L and C_D at geometric angle of attack $\alpha = 0$ in uniform flow with cross-stream position Y/c, where the C_L and C_D values at $Y/c = 0$ are respectively subtracted. Geometric $\alpha = 0$ is referenced at $Y/c = 0$ and held fixed at each position.

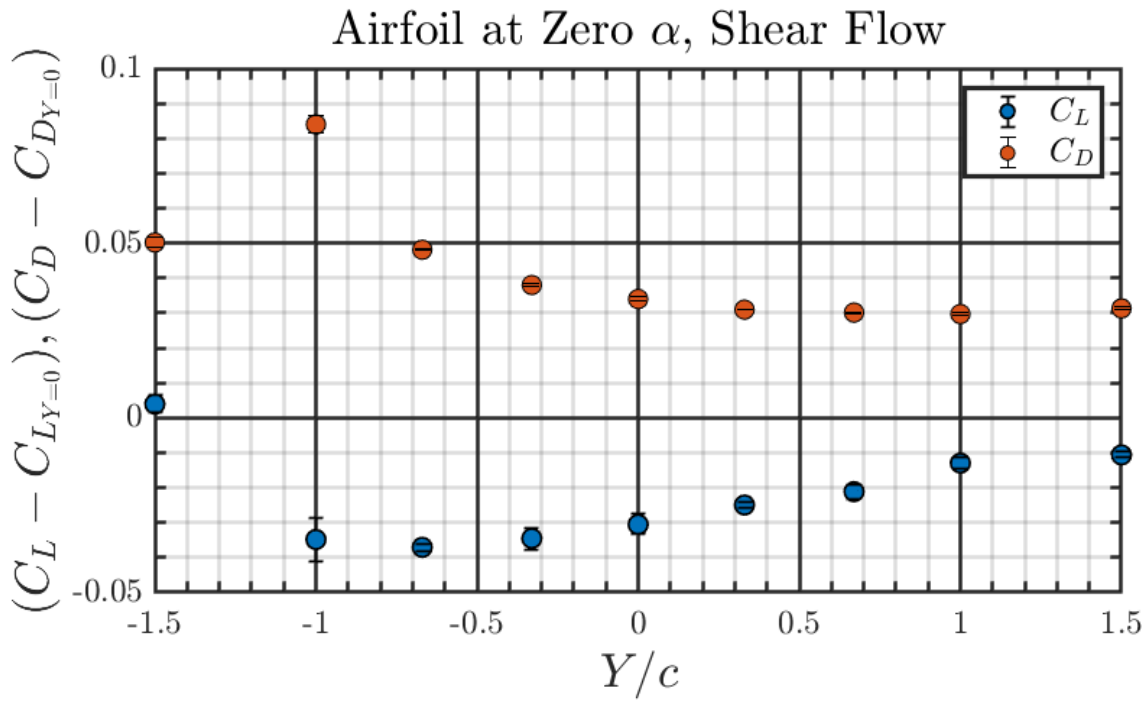

Figure C.3: Variation of C_L and C_D at geometric angle of attack $\alpha = 0$ in shear flow with cross-stream position Y/c, where the C_L and C_D values at $Y/c = 0$ in uniform flow are respectively subtracted. Geometric $\alpha = 0$ is referenced at $Y/c = 0$ in uniform flow and held fixed at each position.

APPENDIX D

LASER AND CAMERA TRIGGERING SYNCHRONIZATION

The system used to synchronously trigger the laser and pco.dimax S4 camera works as follows, with a corresponding diagram in Fig. D.1. For stationary airfoil 1c-MTV measurements, a digital delay generator (Stanford Research Systems model DG535 Digital Delay/Pulse Generator) is triggered internally. For the moving airfoil 1c-MTV measurements, the digital delay generator (DDG) is triggered externally using the output-on-position (OOP) feature of the ACR9000. The OOP feature creates a 5 V transistor-transistor logic (TTL) pulse when the encoder on the linear positioner reaches prescribed positions, such as when the airfoil passes through the centerline position. In both the stationary and the moving airfoil cases, the pulse paths from the DDG are the same.

Once the DDG is triggered it sends two pulses to the ACR9000 via two opto-isolated inputs. One pulse from output CD controls the laser trigger, while the other pulse 1 μs later from output AB controls the camera exposure trigger, represented by the red and blue lines, respectively, in Fig. D.1. The ACR9000 acts as a gate for the pulses, controlled by setting or clearing the bits for the two opto-isolated outputs. The two pulses continue through the opto-isolated outputs, one to the

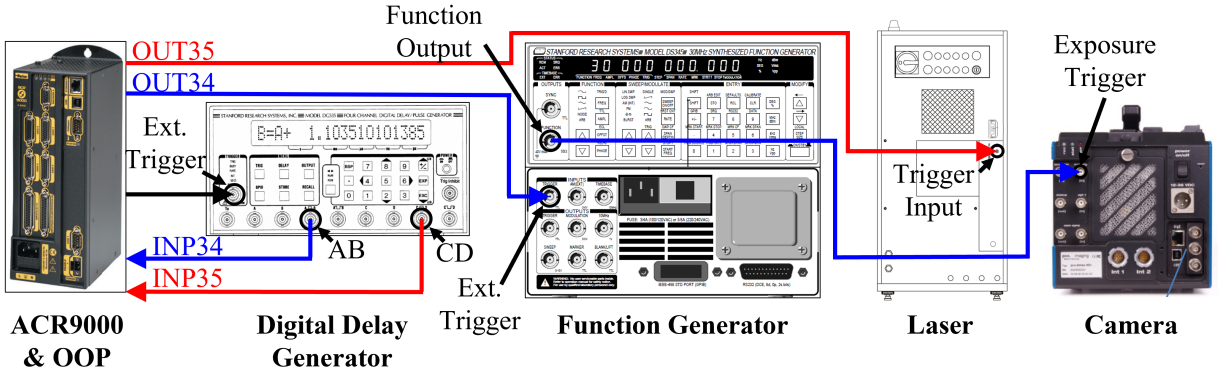

Figure D.1: Laser (red lines) and camera (blue lines) triggering diagram for the pco.dimax S4 camera. This diagram is shown for the case of the digital delay generator (DDG) being triggered externally by the output-on-position (OOP) feature for the plunging airfoil cases. For stationary airfoil cases, the diagram is the same except the DDG is triggered internally. The function generator is setup to create a burst of two pulses which control the exposure of the respective images of an 1c-MTV image pair.

laser trigger input, and the other to the external trigger of the function generator (Stanford Research Systems model DS345 Function and Arbitrary Waveform Generator). The function generator is set to burst mode such that two pulses are output. The frequency (f) setting on the function generator controls the delay time (Δt) between the two pulses ($\Delta t = 1/f$). The two pulses are sent to the pco.dimax S4 camera exposure trigger input, separated by Δt, which creates the trigger signals for the pair of images for 1c-MTV measurements.

In the present work, the pco.dimax S4 camera operates in correlated double-image (CDI) mode. In CDI mode, a reference image is acquired immediately prior to exposure which is subtracted from the subsequent exposed image. The result, as stated by the manufacturer[1], is an image with increased dynamic range and 30% better performance on the weak signal side of the images. The cost of operating in CDI mode is a halving of the frame rate and corresponding doubling of the minimum exposure time, since two images are read off the sensor before the next image acquisition. This is highlighted in Eq. (D.1) where the minimum exposure time $t_{exp_{min}}$ is given in terms of the frame rate in CDI mode, f_{CDI}. The value of f_{CDI} is dependent on the region of interest (ROI) and exposure time t_{exp}, provided $t_{exp} > t_{exp_{min}}$.

$$t_{exp_{min}} = \frac{1}{2 \times f_{CDI}} \tag{D.1}$$

[1]Information regarding CDI mode is gathered from the pco.dimax S4 user manual and personal correspondence with technical service representatives from PCO AG, the camera's manufacturer.

APPENDIX E

COMPLETE UNIFORM FLOW 1C-MTV RESULTS

This appendix contains the complete mean (u'/u_{eff}) and RMS (u'_{rms}/u_{eff}) streamwise flow results by 1c-MTV for both the stationary ($V_r = 0$) and plunging ($V_r \neq 0$) airfoils in uniform flow ($K = 0$), and at each of the three cross-stream positions ($Y/c = 0$ and ± 0.5) where the Re_c is specified. See the figure titles for the respective airfoil geometry, motion and flow conditions.

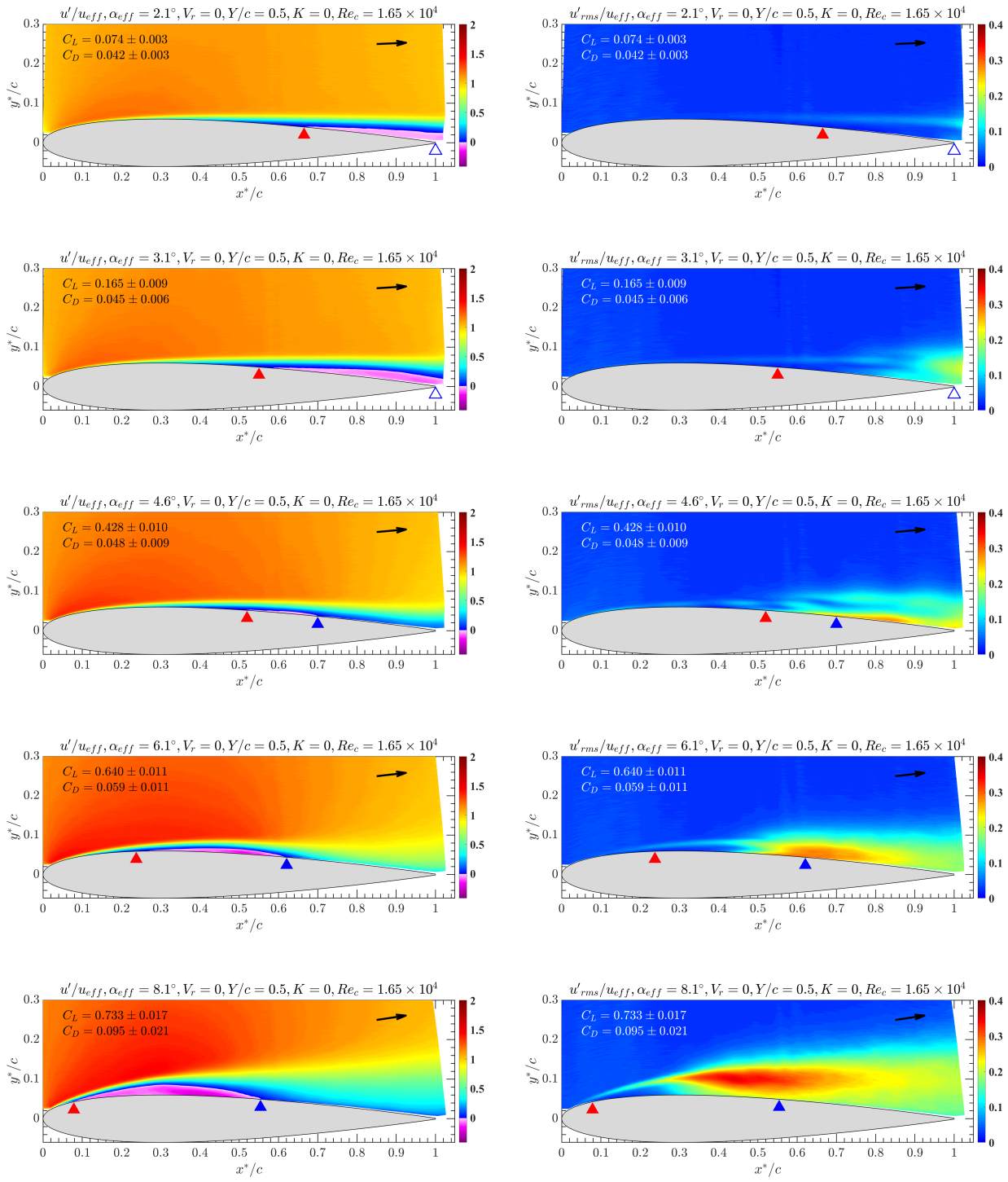

Figure E.1: Mean (left) and RMS (right) streamwise velocity measurements by 1c-MTV for the stationary airfoil. Black arrow: direction of the approach stream in the laboratory reference frame. Red triangle: boundary layer separation location. Open blue triangle: open separation at the trailing edge. Closed blue triangle: reattachment with a closed separation bubble.

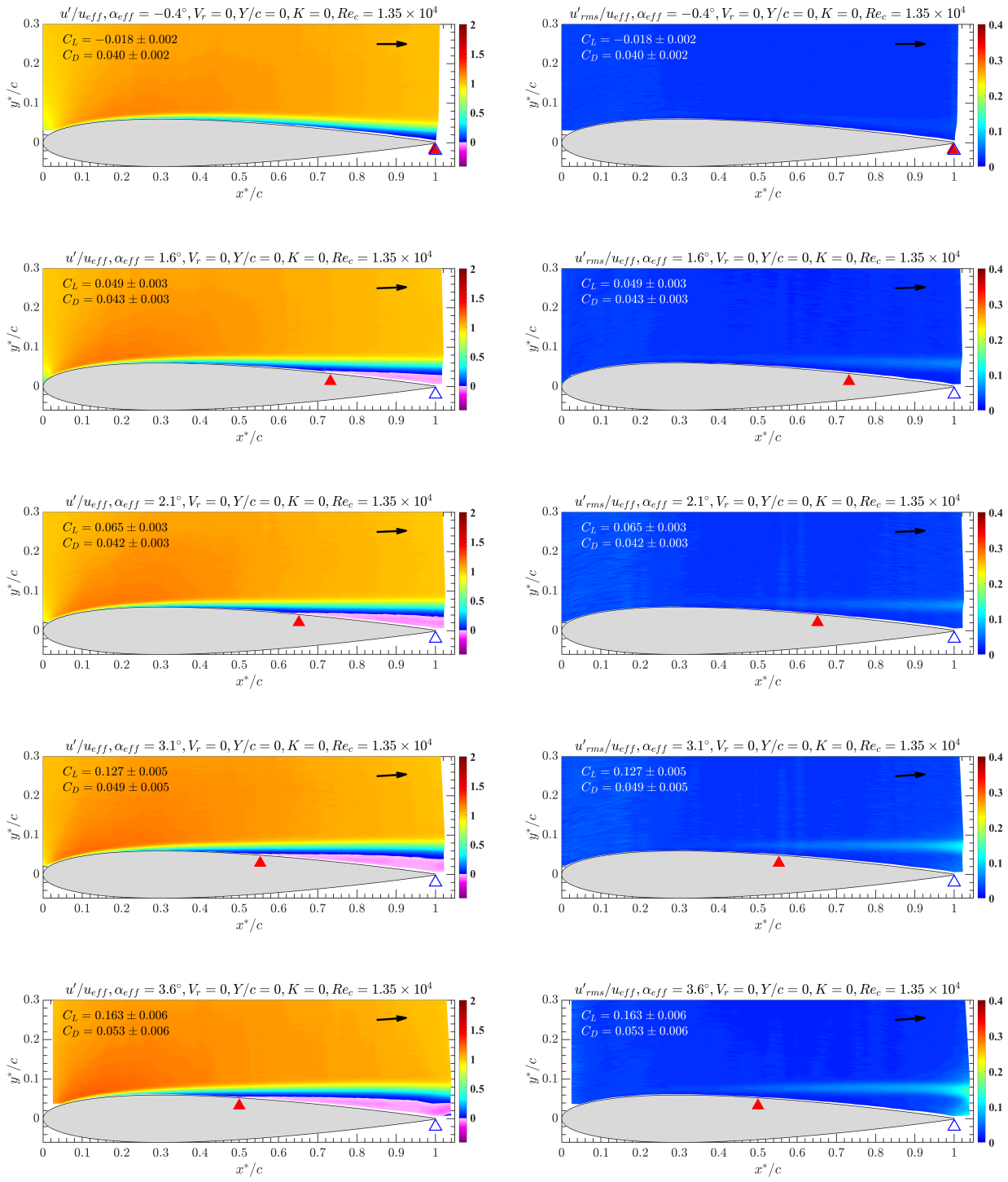

Figure E.2: Mean (left) and RMS (right) streamwise velocity measurements by 1c-MTV for the stationary airfoil. Black arrow: direction of the approach stream in the laboratory reference frame. Red triangle: boundary layer separation location. Open blue triangle: open separation at the trailing edge. Closed blue triangle: reattachment with a closed separation bubble.

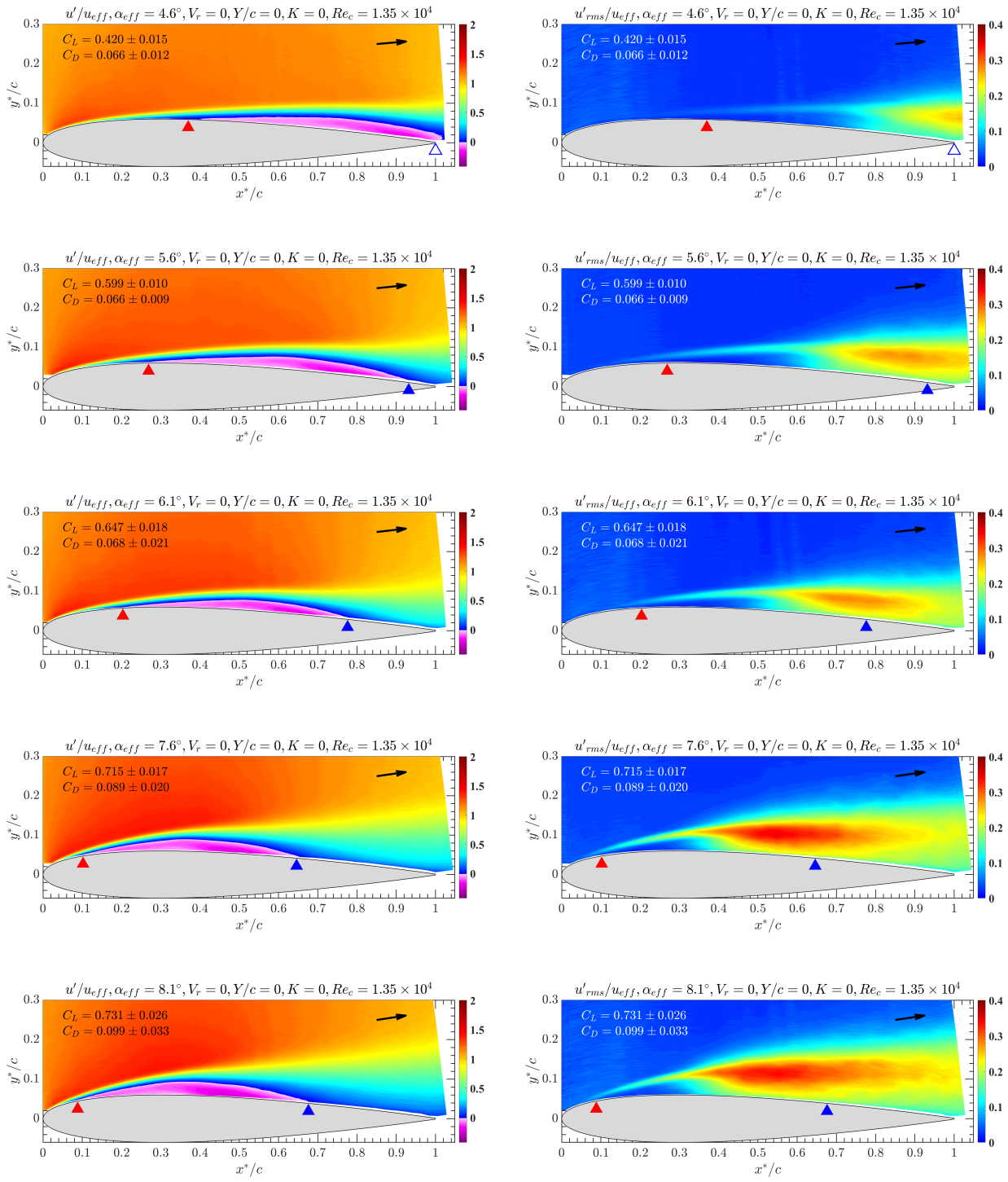

Figure E.3: Mean (left) and RMS (right) streamwise velocity measurements by 1c-MTV for the stationary airfoil. Black arrow: direction of the approach stream in the laboratory reference frame. Red triangle: boundary layer separation location. Open blue triangle: open separation at the trailing edge. Closed blue triangle: reattachment with a closed separation bubble.

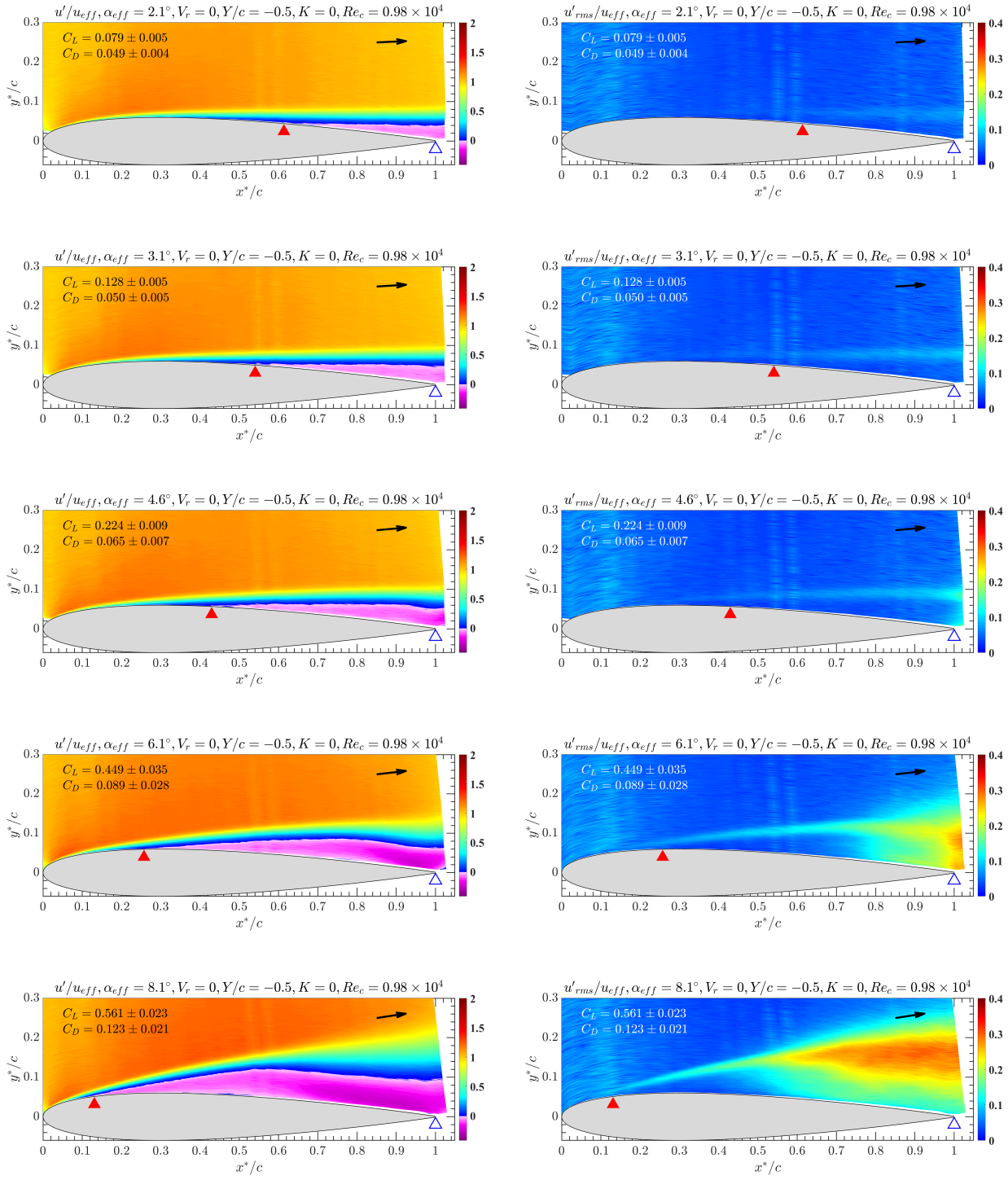

Figure E.4: Mean (left) and RMS (right) streamwise velocity measurements by 1c-MTV for the stationary airfoil. Black arrow: direction of the approach stream in the laboratory reference frame. Red triangle: boundary layer separation location. Open blue triangle: open separation at the trailing edge. Closed blue triangle: reattachment with a closed separation bubble.

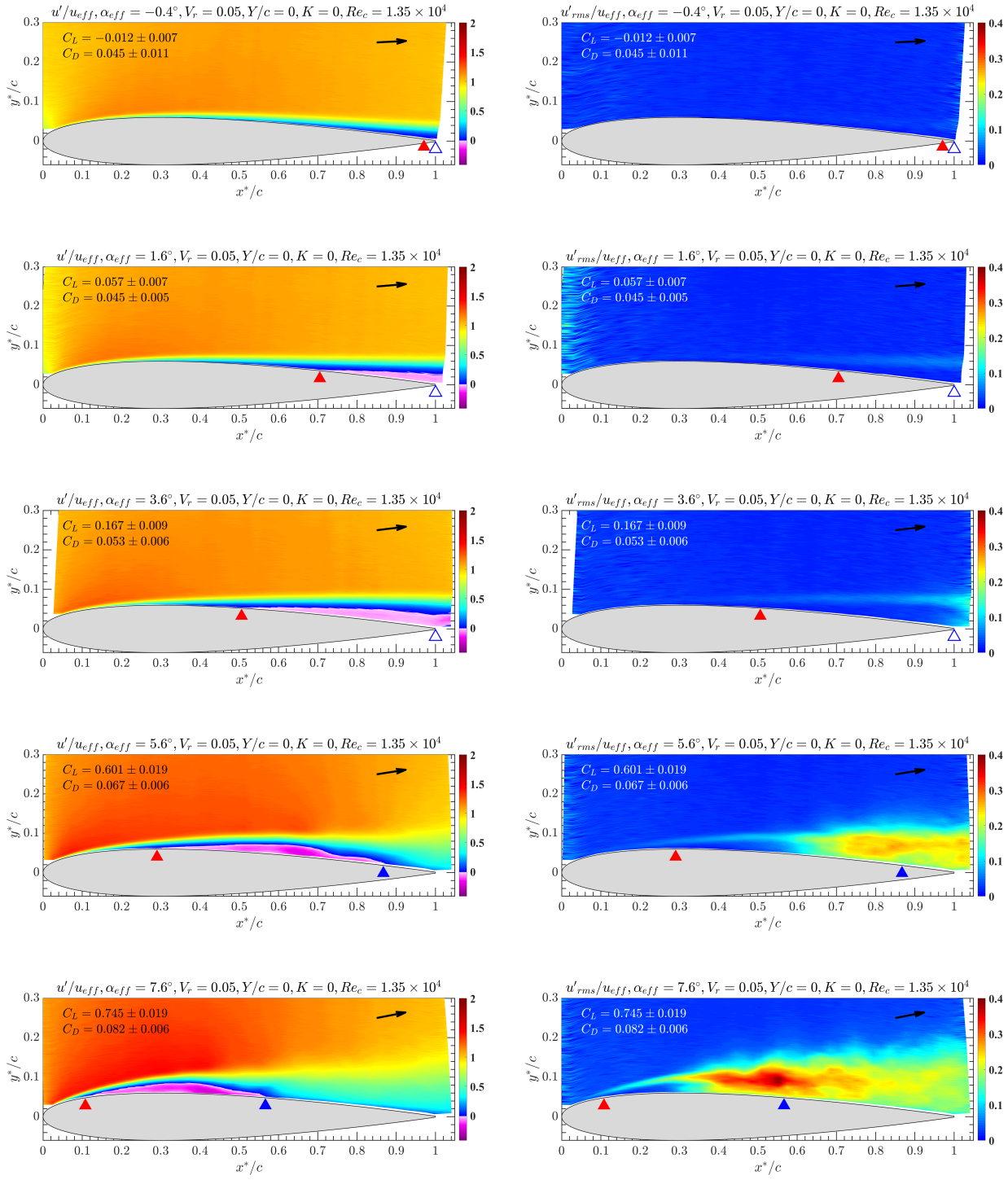

Figure E.5: Mean (left) and RMS (right) streamwise velocity measurements by 1c-MTV for the plunging airfoil. Black arrow: direction of the approach stream in the laboratory reference frame. Red triangle: boundary layer separation location. Open blue triangle: open separation at the trailing edge. Closed blue triangle: reattachment with a closed separation bubble.

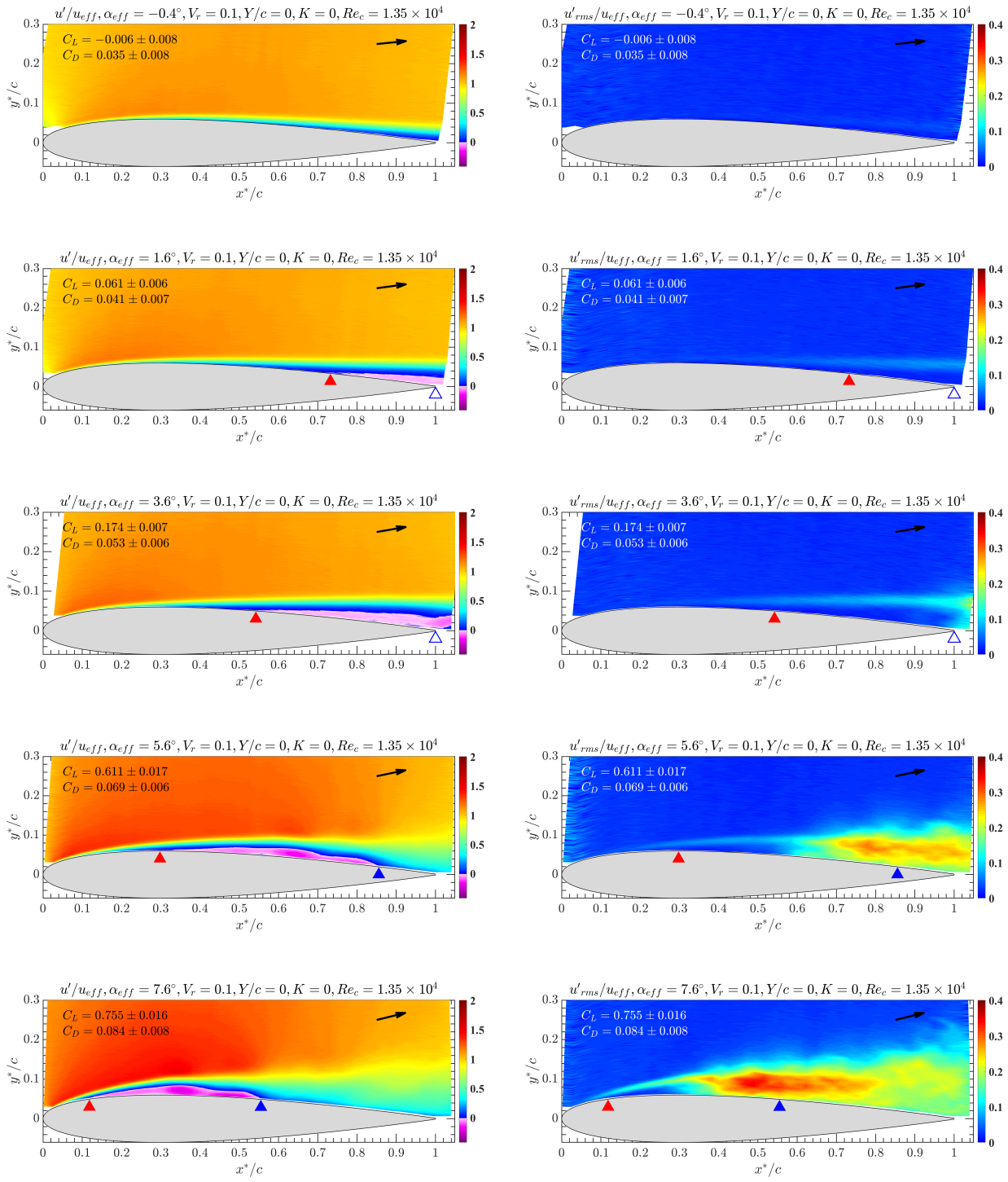

Figure E.6: Mean (left) and RMS (right) streamwise velocity measurements by 1c-MTV for the plunging airfoil. Black arrow: direction of the approach stream in the laboratory reference frame. Red triangle: boundary layer separation location. Open blue triangle: open separation at the trailing edge. Closed blue triangle: reattachment with a closed separation bubble.

APPENDIX F

COMPLETE SHEAR FLOW 1C-MTV RESULTS

This appendix contains the complete mean (u'/u_{eff}) and RMS (u'_{rms}/u_{eff}) streamwise flow results by 1c-MTV for both the stationary ($V_r = 0$) and plunging ($V_r \neq 0$) airfoils in shear flow ($K \neq 0$), and at each of the three cross-stream positions ($Y/c = 0$ and ± 0.5) where the K and Re_c are specified. See the figure titles for the respective airfoil geometry, motion and flow conditions.

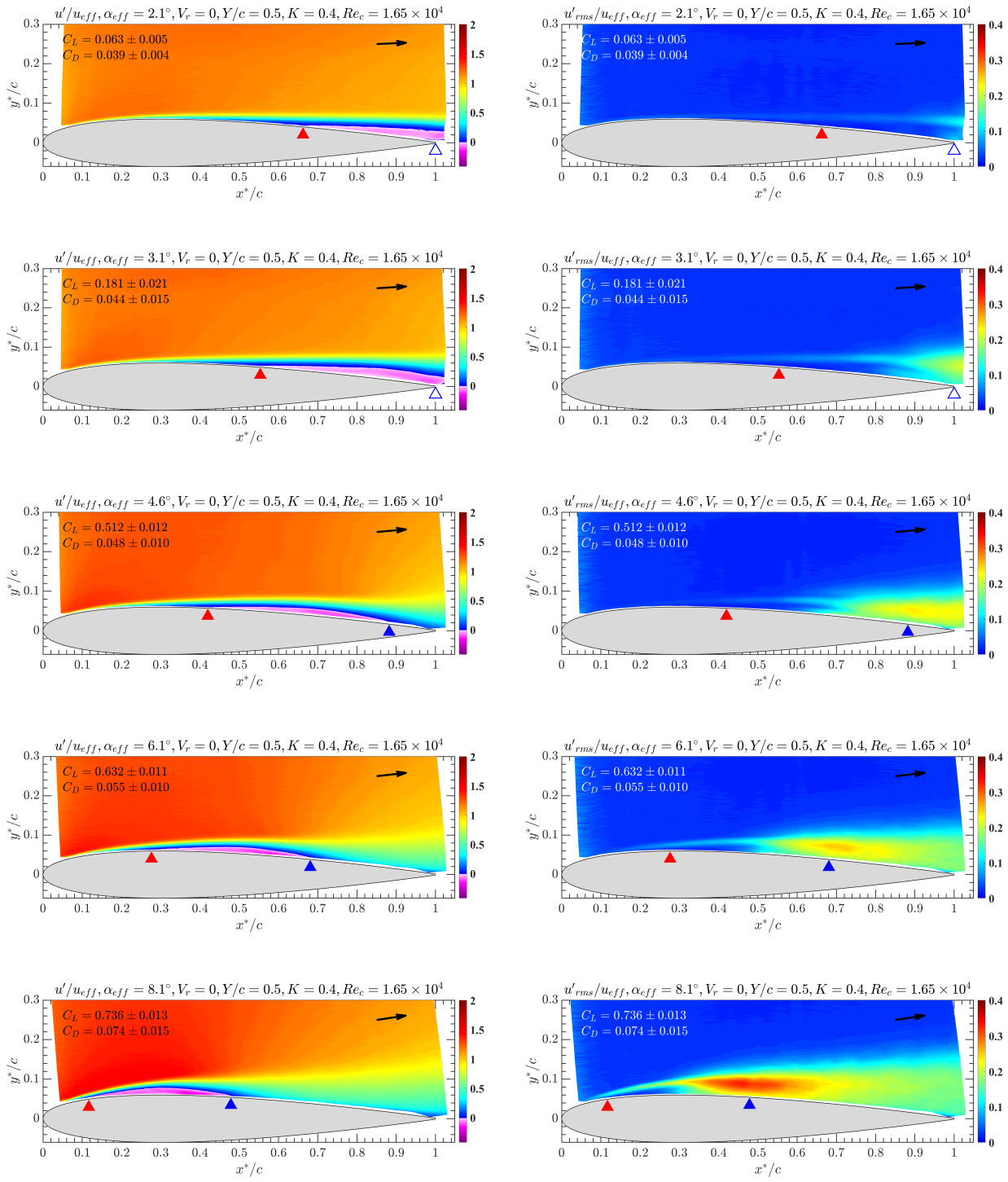

Figure F.1: Mean (left) and RMS (right) streamwise velocity measurements by 1c-MTV for the stationary airfoil. Black arrow: direction of the approach stream in the laboratory reference frame. Red triangle: boundary layer separation location. Open blue triangle: open separation at the trailing edge. Closed blue triangle: reattachment with a closed separation bubble.

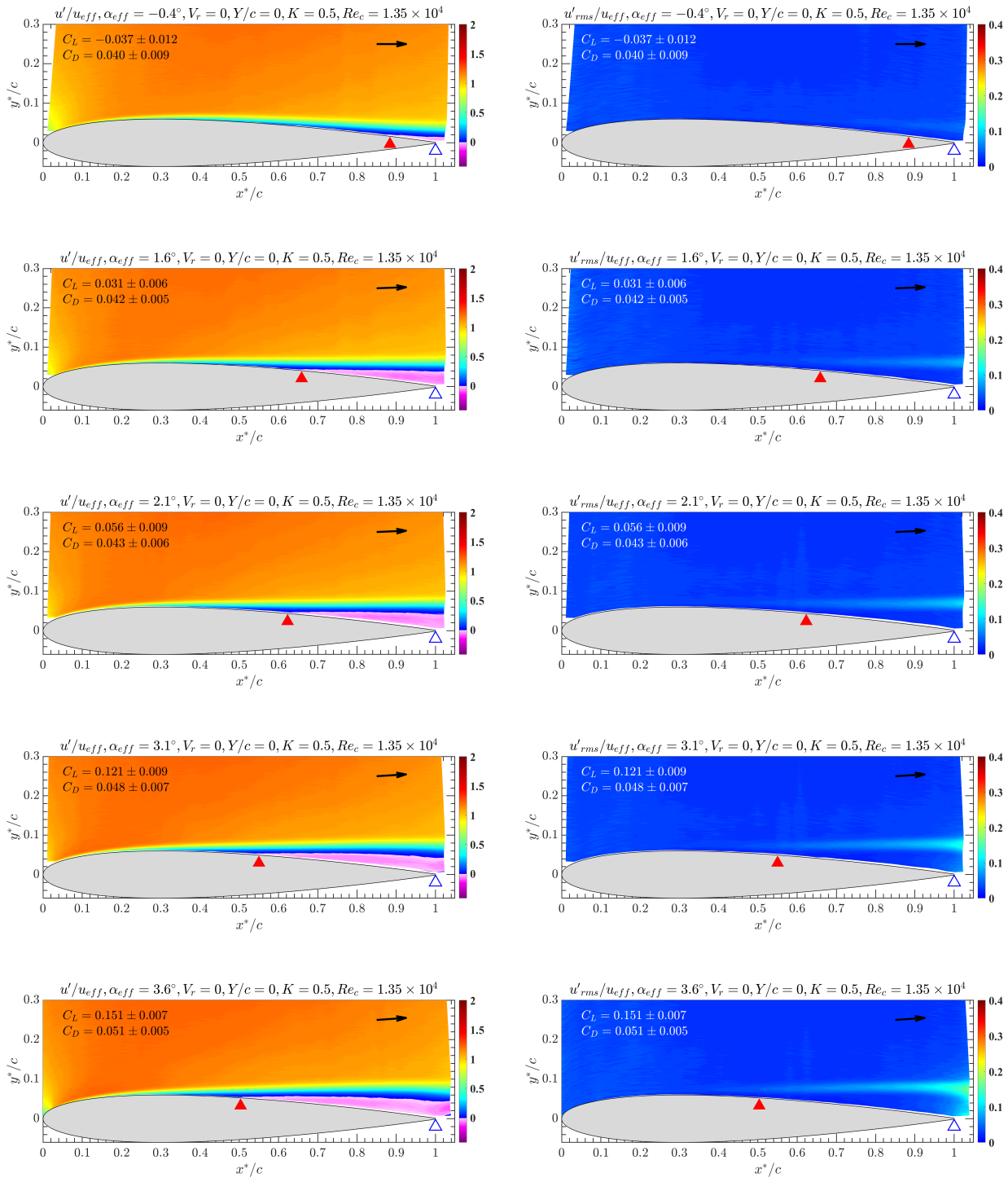

Figure F.2: Mean (left) and RMS (right) streamwise velocity measurements by 1c-MTV for the stationary airfoil. Black arrow: direction of the approach stream in the laboratory reference frame. Red triangle: boundary layer separation location. Open blue triangle: open separation at the trailing edge. Closed blue triangle: reattachment with a closed separation bubble.

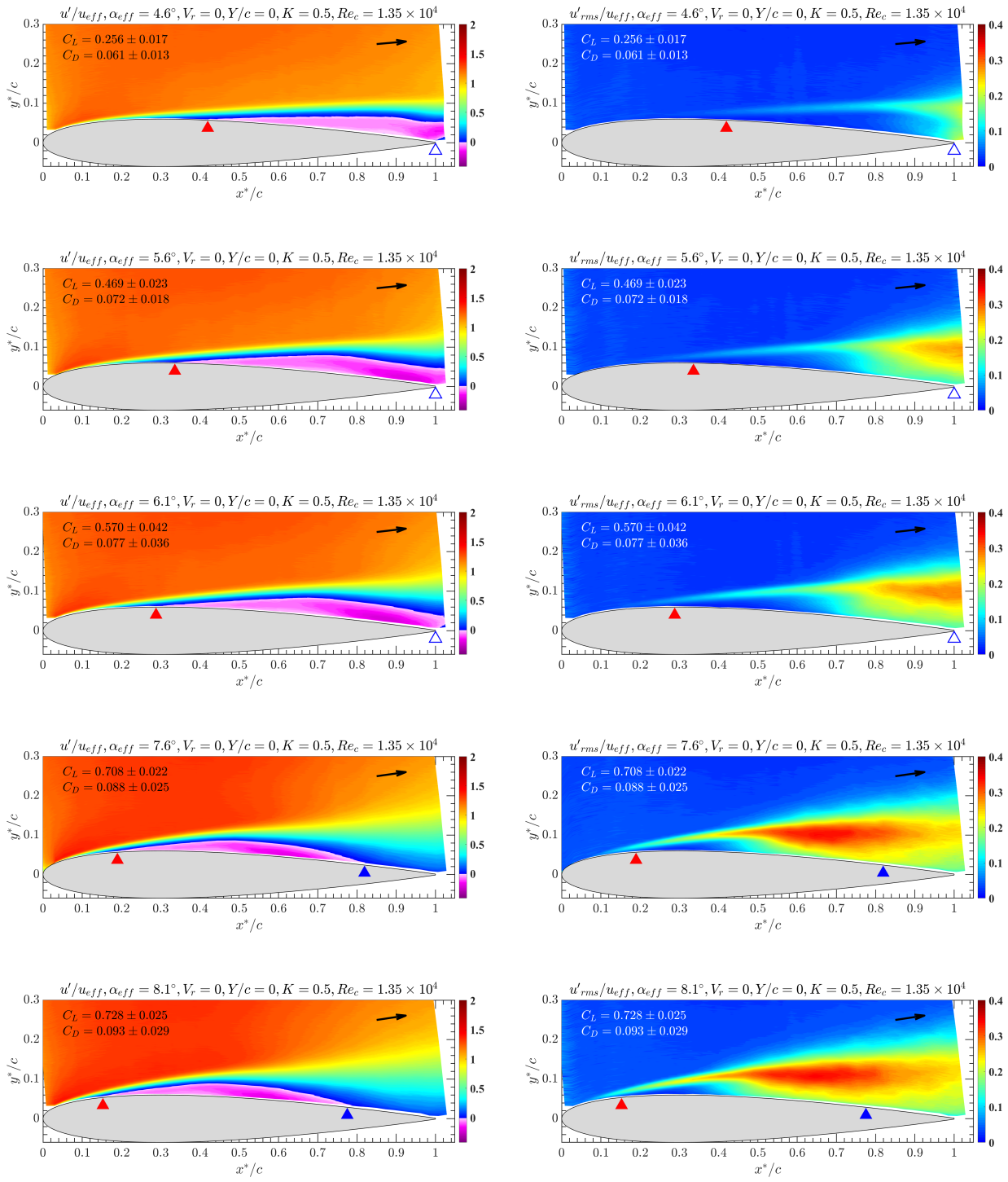

Figure F.3: Mean (left) and RMS (right) streamwise velocity measurements by 1c-MTV for the stationary airfoil. Black arrow: direction of the approach stream in the laboratory reference frame. Red triangle: boundary layer separation location. Open blue triangle: open separation at the trailing edge. Closed blue triangle: reattachment with a closed separation bubble.

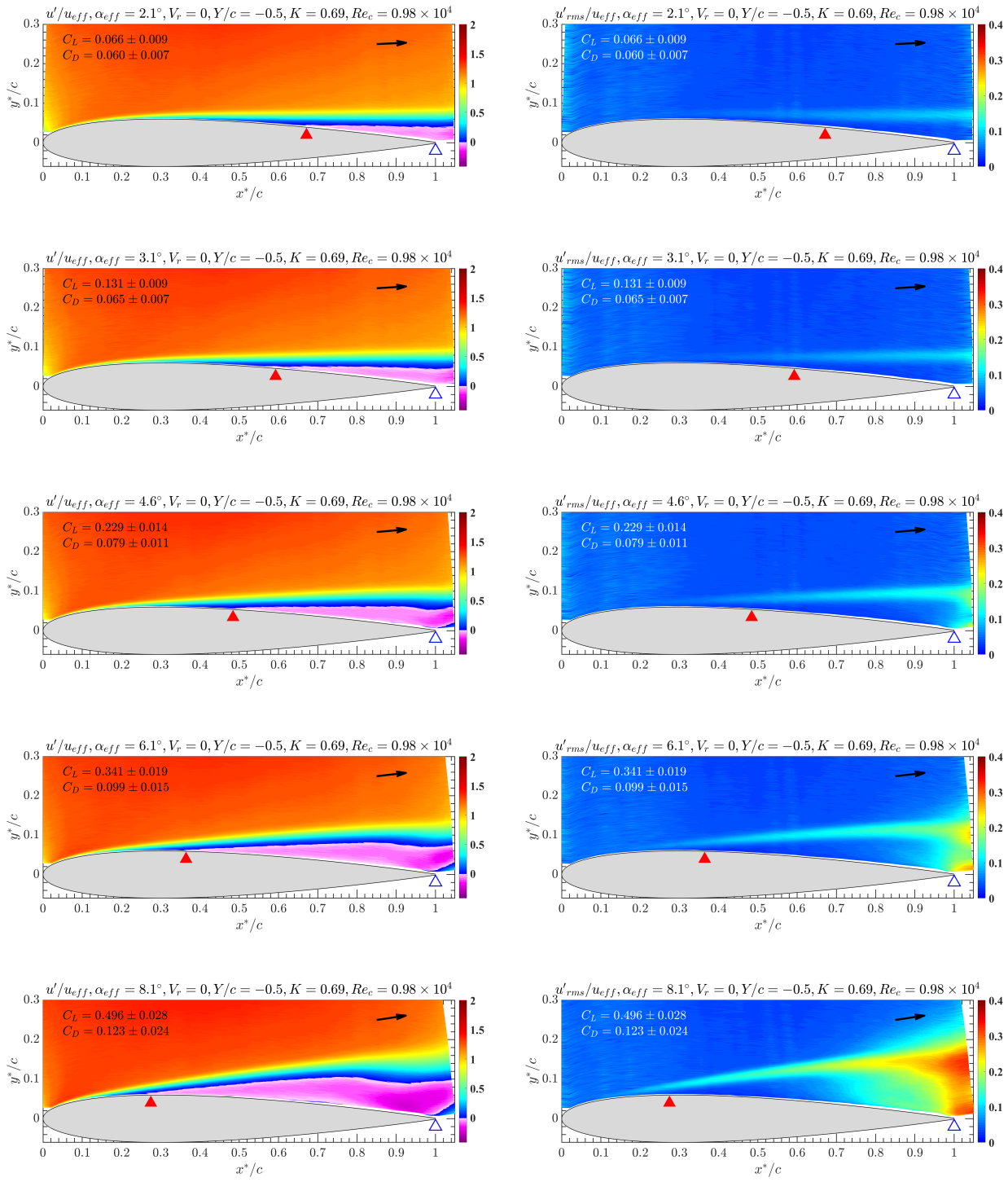

Figure F.4: Mean (left) and RMS (right) streamwise velocity measurements by 1c-MTV for the stationary airfoil. Black arrow: direction of the approach stream in the laboratory reference frame. Red triangle: boundary layer separation location. Open blue triangle: open separation at the trailing edge. Closed blue triangle: reattachment with a closed separation bubble.

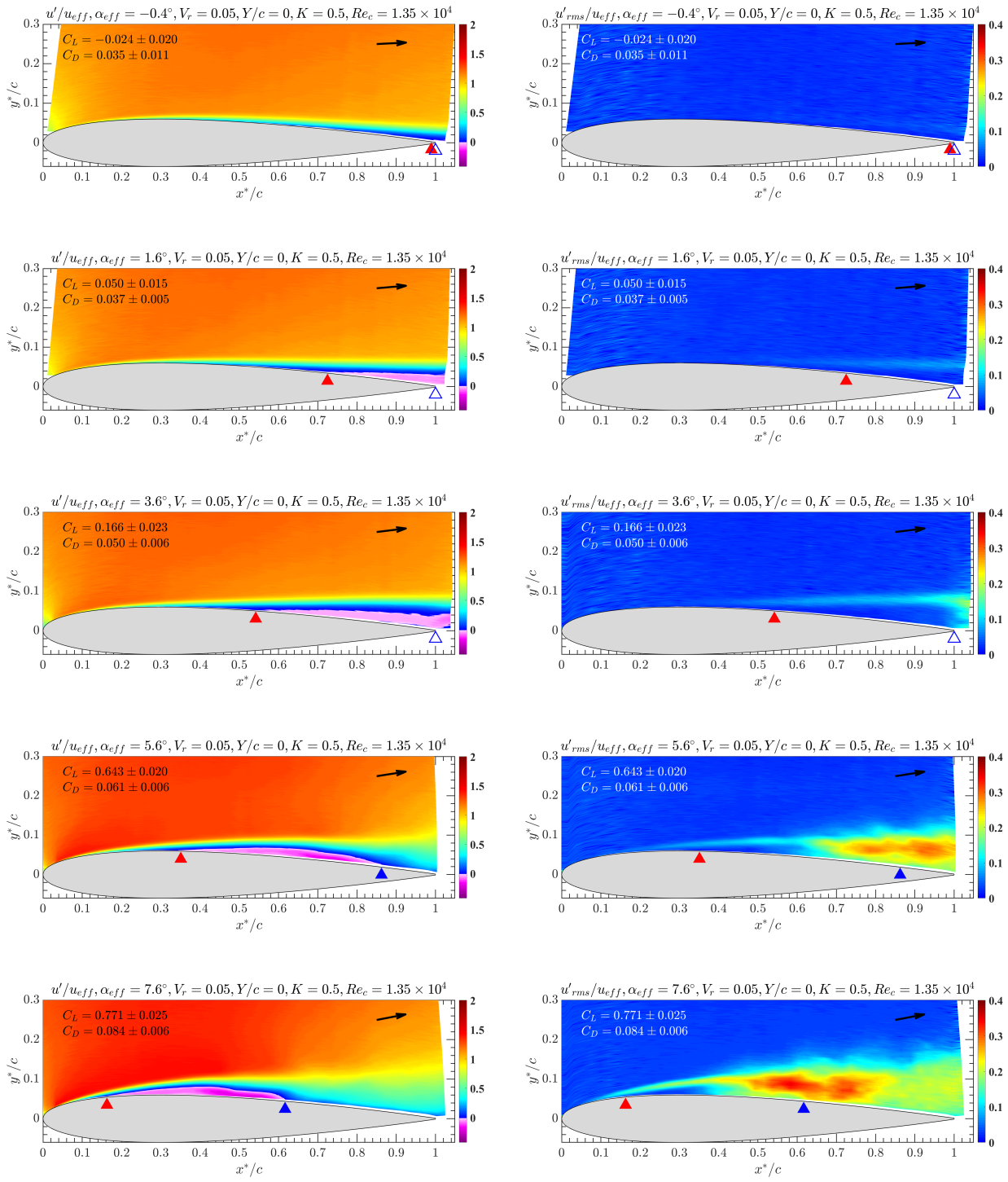

Figure F.5: Mean (left) and RMS (right) streamwise velocity measurements by 1c-MTV for the plunging airfoil. Black arrow: direction of the approach stream in the laboratory reference frame. Red triangle: boundary layer separation location. Open blue triangle: open separation at the trailing edge. Closed blue triangle: reattachment with a closed separation bubble.

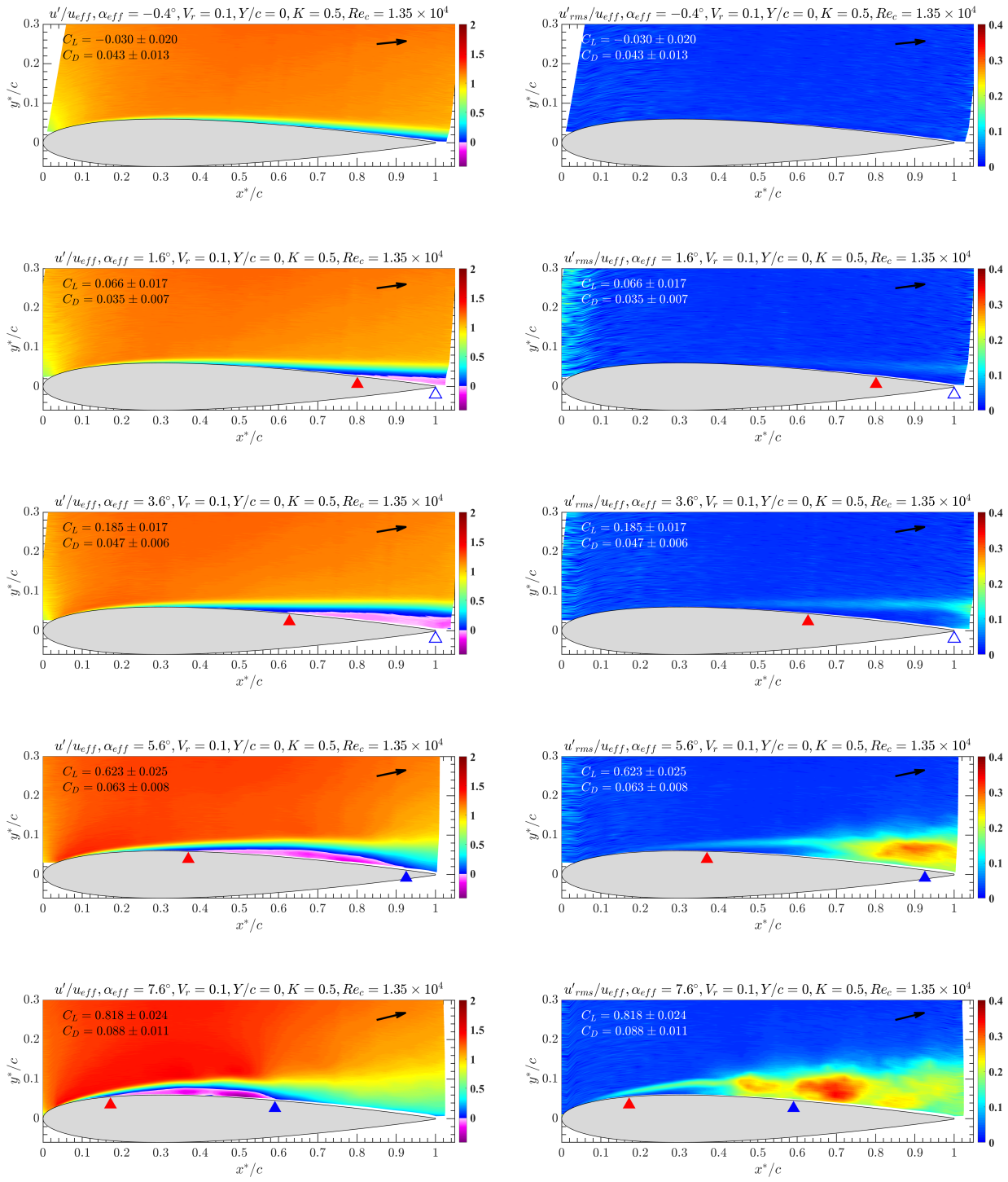

Figure F.6: Mean (left) and RMS (right) streamwise velocity measurements by 1c-MTV for the plunging airfoil. Black arrow: direction of the approach stream in the laboratory reference frame. Red triangle: boundary layer separation location. Open blue triangle: open separation at the trailing edge. Closed blue triangle: reattachment with a closed separation bubble.

BIBLIOGRAPHY

BIBLIOGRAPHY

Albrecht, M. B., D. A. Olson, A. N. Naguib & M. M. Koochesfahani. 2022. Reynolds Number and Freestream Shear Effects on a NACA 0012 Airfoil in the Reynolds Number Range 10,000-30,000. In *2022 AIAA Aerospace Sciences Meeting, AIAA SciTech Forum* AIAA 2022-1055, AIAA.

Benedict, L. H. & R. D. Gould. 1996. Towards better uncertainty estimates for turbulence statistics. *Experiments in Fluids* 22. 129–136.

Bohl, D. G. 2002. *Experimental Study of the 2-D and 3-D Structure of a Concentrated Line Vortex Array*: Michigan State University Ph.D. Dissertation.

Brown, T. A. 1992. *Effects of Motion History on Leading Edge Separation for an Airfoil Pitching to Large Angles of Attack*. Michigan State University M.S. Thesis.

Carr, L. W. 1988. Progress in analysis and prediction of dynamic stall. *Journal of Aircraft* 25(1). 6–17.

Chee, C. L. 2005. *An Experimental Study of Pressure- and Electroosmotically-Driven Flows in Microchannels with Surface Modifications*: Michigan State University Ph.D. Dissertation.

Cherry, B. E. & M. M. Constantino. 2010. The Burble Effect: Superstructure and Flight Deck Effects on Carrier Air Wake. Tech. rep. United States Naval Academy, Annapolis, MD.

Cleaver, D., Z. Wang & I. Gursul. 2010. Vortex Mode Bifurcation and Lift Force of a Plunging Airfoil at Low Reynolds Numbers. In *48th AIAA Aerospace Sciences Meeting Including the New Horizons Forum and Aerospace Exposition* AIAA 2010-390, AIAA.

Cleaver, D. J., Z. Wang & I. Gursul. 2013. Investigation of High-Lift Mechanisms for a Flat Plate Airfoil Undergoing Small-Amplitude Plunging Oscillations. *AIAA Journal* 51(4). 968–980.

Cook, R., D. Atkinson, R. Milla, N. Revill & P. Wilson. 2010. Development of the Shipborne rolling vertical landing (SRVL) manoeuvre for the F-35B aircraft. In *Proceeding of the International Powered Lift Conference*, 5–7.

Francis, M. S. & J. E. Keesee. 1985. Airfoil Dynamic Stall Performance with Large-Amplitude Motions. *AIAA Journal* 23(11). 1653–1659.

Gendrich, C. P. 1999. *Dynamic Stall of Rapidly Pitching Airfoils: MTV Experiments and Navier-Stokes Simulations*: Michigan State University Ph.D. dissertation.

Gendrich, C. P., M. M. Koochesfahani & D. G. Nocera. 1997. Molecular tagging velocimetry and other novel applications of a new phosphorescent supramolecule. *Experiments in Fluids* 23(5). 361–372.

Gendrich, C. P., M. M. Koochesfahani & M. R. Visbal. 1995. Effects of Initial Acceleration on the Flow Field Development Around Rapidly Pitching Airfoils. *Journal of Fluids Engineering* 117(1). 45–49.

Hamedani, B. A., A. M. Naguib & M. M. Koochesfahani. 2017. An Experimental Investigation of an Airfoil Traversing Across a Shear Flow. In *APS Meeting Abstracts*, A18.00003.

Hamedani, B. A., A. N. Naguib & M. M. Koochesfahani. 2019. Reynolds Number Effect on Lift Characteristics of an Airfoil Translating Across a Non-uniform Approach Flow. In *2019 AIAA Aerospace Sciences Meeting, AIAA SciTech Forum* AIAA 2019-0639, AIAA.

Hammer, P. R., D. A. Olson, M. R. Visbal, A. M. Naguib & M. M. Koochesfahani. 2018. An Investigation of the Aerodynamics of a Harmonically-Pitching Airfoil in Uniform-Shear Approach Flow. In *2018 AIAA Aerospace Sciences Meeting, AIAA SciTech Forum* AIAA 2018-0575, AIAA.

Hammer, P. R., D. A. Olson, M. R. Visbal, A. M. Naguib & M. M. Koochesfahani. 2019. Joint Computational-Experimental Investigation of Harmonically Pitching Airfoil Aerodynamics in Uniform-Shear Approach Flow. *AIAA Journal* 57(8). 3290–3298.

Hammer, P. R., M. R. Visbal, A. M. Naguib & M. M. Koochesfahani. 2018. Lift on a steady 2-D symmetric airfoil in viscous uniform shear flow. *Journal of Fluid Mechanics* 837. R2.

Hill, R. B. & J. C. Klewicki. 1996. Data reduction methods for flow tagging velocity measurements. *Experiments in Fluids* 20(3). 142–152.

Honda, M. 1960. Theory of a thin wing in a shear flow. *Proceedings of the Royal Society of London. Series A. Mathematical and Physical Sciences* 254(1278). 372–394.

James, D. G. 1951. Two-Dimensional Airfoils in Shear Flow. I. *The Quarterly Journal of Mechanics and Applied Mathematics* 4(4). 407–418.

Jumper, E. J., S. J. Schreck & R. L. DImmick. 1987. Lift-curve characteristics for an airfoil pitching at constant rate. *Journal of Aircraft* 24(10). 680–687.

Katz, A. W. 2010. *Molecular Tagging Velocimetry Measurements of the Low-Reynolds-Number Flow Around an SD7003 Airfoil*. Michigan State University M.S. Thesis.

Kaul, C. E., S. C. Collyer & G. Lintern. 1980. Glideslope Descent-Rate Cuing to Aid Carrier Landings. Tech. rep. Naval Training Equipment Center, Naval Air Systems Command, Technical Report NAVTRAEQUIPCEN IH-322.

Kelly, M. F., M. White, I. Owen & S. J. Hodge. 2016. Using airwake simulation to inform flight trials for the Queen Elizabeth Class Carrier. In *IMarEST 13th International Naval Engineering Conference and Exhibition, (INEC 2016)*, Bristol, UK.

Kim, D.-H., J.-W. Chang & J. Chung. 2011. Low-Reynolds-Number Effect on Aerodynamic Characteristics of a NACA 0012 Airfoil. *Journal of Aircraft* 48(4). 1212–1215.

Koochesfahani, M. M & D. G. Nocera. 2007. Molecular Tagging Velocimetry (MTV). In Tropea, C. and Yarin, A. L. and Foss, J. F. (ed.), *Springer Handbook of Experimental Fluid Mechanics*, chap. B.5.4, 362–382. Springer-Verlag Berlin Heidelberg.

Kotansky, D. R. 1966. The use of honeycomb for shear flow generation. *AIAA Journal* 4(8). 1490–1491.

Laitone, E. V. 1997. Wind tunnel tests of wings at Reynolds number below 70000. *Experiments in Fluids* 23. 405–409.

McCroskey, W. J. 1982. Unsteady Airfoils. *Annual Review of Fluid Mechanics* 14. 285–311.

McCroskey, W. J. 1987. A Critical Assessment of Wind Tunnel Results for the NACA 0012 Airfoil. Tech. rep. NASA Technical Momorandum 100019 USAAVSCOM Technical Report 87-A-5.

Naguib, A. N. & M. M. Koochesfahani. 2020. Inviscid flow analysis of a circular cylinder traversing across an unbounded uniform-shear stream. *Journal of Fluid Mechanics* 882(A21).

Nishiyama, T. & K. Hirano. 1970. Aerofoil Section Characteristics in Shear Flows. *Ingenieur-Archiv* 39(3). 137–148.

Ohtake, T., Y. Nakae & T. Motohashi. 2007. Nonlinearity of the Aerodynamic Characteristics of NACA0012 Aerofoil at Low Reynolds Numbers. *The Japan Society for Aeronautical and Space Sciences* 55(644). 439–445.

Olson, D., A. Naguib & M. Koochesfahani. 2016. Experiments on a steady low Reynolds number airfoil in a shear flow. In *APS Meeting Abstracts*, E6.00006.

Olson, D. A. 2011. *Facility and Flow Dependence Issues Influencing the Experimental Characterization of a Laminar Separation Bubble at Low Reynolds Number*. Michigan State University M.S. Thesis.

Olson, D. A. 2017. *The Influence of Chordwise Flexibility on the Flow Structure and Streamwise Force of a Sinusoidally Pitching Airfoil*: Michigan State University Ph.D. Dissertation.

Olson, D. A., A. W. Katz, A. M. Naguib, M. M. Koochesfahani, D. P. Rizzetta & M. R. Visbal. 2013. On the challenges in experimental characterization of flow separation over airfoils at low reynolds number. *Experiments in Fluids* 54:1470.

Olson, D. A., A. M. Naguib & M. M. Koochesfahani. 2018. The effect of steady shear on the aerodynamic performance of an airfoil at low Reynolds number. In *APS Meeting Abstracts*, F16.00002.

Payne, F. M. & R. C. Nelson. 1985. Aerodynamic Characteristics of an Airfoil in a Nonuniform Wind Profile. *Journal of Aircraft* 22(1). 5–10.

Safaripour, A., D. A Olson, A. M Naguib & M. M Koochesfahani. 2016. On Using Shaped Honeycombs for Experimental Generation of Arbitrary Velocity Profiles in Test Facilities. In *APS Meeting Abstracts*, G31.006.

Safaripour-Tabalvandani, A. 2020. *Effects of Shear Layer Unsteadiness on the Aerodynamics of a Pitching Airfoil*: Michigan State University Ph.D. Dissertation.

Smiljanovski, V. 1990. *Flow Visualization of the Flow Field of an Airfoil Pitching to Large Angles of Attack*. Michigan State University Diplomarbeit.

Sunada, S., A. Sakaguchi & K. Kawachi. 1997. Airfoil Section Characteristics at a Low Reynolds Number. *Journal of Fluids Engineering* 119(1). 129–135.

Tank, J., L. Smith & G. R. Spedding. 2017. On the possibility (Or lack thereof) of agreement between experiment and computation of flows over wings at moderate Reynolds number. *Interface Focus* 7(1).

Theodorsen, T. 1935. General Theory of Aerodynamic Instability and the Mechanism of Flutter. Tech. Rep. 496 National Advisory Committee for Aeronautics.

Tsien, H. S. 1943. Symmetrical Joukowsky Airfoils in Shear Flow. *Quarterly of Applied Mathematics* 1(2). 130–148.

Wagner, H. 1925. Über die Entstehung des dynamischen Auftriebes von Tragflügeln. *Zeitschrift für Angewandte Mathematik und Mechanik* 5(1). 17–35.

Watson, N. A., M. F. Kelly, I. Owen, S. J. Hodge & M. D. White. 2019. Computational and experimental modelling study of the unsteady airflow over the aircraft carrier HMS Queen Elizabeth. *Ocean Engineering* 172. 562–574.

Yu, M., B. Wang, Z. J. Wang & S. Farokhi. 2018. Evolution of vortex structures over flapping foils in shear flows and its impact on aerodynamic performance. *Journal of Fluids and Structures* 76. 116–134.